HOKKAIDO UNIVERSITY

Title	EFFICIENT AND ACCURATE PHASE UNWRAPPING ALGORITHMS FOR NOISY IMAGES WITHIN FRINGE PATTERNS
Author(s)	Abdelwahab, Samia Heshmat Hassan
Degree Grantor	北海道大学
Degree Name	博士(工学)
Dissertation Number	甲第11450号
Issue Date	2014-03-25
DOI	https://doi.org/10.14943/doctoral.k11450
Doc URL	https://hdl.handle.net/2115/57189
Type	doctoral thesis
File Information	Samia_Heshmat_Hassan_Abdel_Wahab.pdf

Hokkaido University Collection of Scholarly and Academic Papers : HUSCAP

EFFICIENT AND ACCURATE PHASE UNWRAPPING ALGORITHMS FOR NOISY IMAGES WITHIN FRINGE PATTERNS

高雑音干渉縞に対する高効率高精度位相連結アルゴリズム

SAMIA HESHMAT H. ABDELWAHAB

Graduate School of Engineering
Hokkaido University
Sapporo, JAPAN

EFFICIENT AND ACCURATE PHASE UNWRAPPING ALGORITHMS FOR NOISY IMAGES WITHIN FRINGE PATTERNS

高雑音干渉縞に対する高効率高精度位相連結アルゴリズム

A DISSERTATION

Submitted in partial fulfillment of the
requirements for the Degree of

DOCTOR OF PHILOSOPHY

by

SAMIA HESHMAT H. ABDELWAHAB

Graduate School of Engineering
Hokkaido University
Sapporo, JAPAN

March 2014

Dedication

This piece of work is dedicated to:

My respectful parents	*My father and mother*
My loving family	*My brothers and sisters*
My dearest husband	*Mohamed Zakaria*
My beloved sons	*Reyad and Eyad*

Declaration

This work has not previously been submitted for a degree or diploma in any university. To the best of my knowledge and belief, the dissertation contains no material previously published or written by another person except where due reference is made in the dissertation itself.

Samia Heshmat
Sapporo, JAPAN
March 2014

Acknowledgments

Thanks to **Almighty Allah** who guided me and aided me to bring-forth for the achievement of this research.

I am greatly indebted to my supervisor **Assoc. Prof. Satoshi Tomioka**, for his precious advice and supportive guidance throughout this research work. Under whose kind supervision and sympathetic attitude, the present research was completed.

Sincere gratitude is also expressed to **Prof. Koichi Sasaki**, **Prof. Masafumi Itagaki** and **Prof. Yuichi Murai**, who are the members of the dissertation examination committee, for their valuable remarks and constructive criticism, especially in the annual evaluations. Our numerous fruitful discussions contribute in various ways to the realization and finalization of this study. Grateful acknowledgments are also extended to all the professors that accepted to be members of the examination committee of the public defense.

Sincere gratitude is also expressed to **Assist. Prof. Shusuke Nishiyama**, for the advice and helpful comments during the seminar and discussion. I fully appreciate the kindness and patience shown upon me.

I should give my appreciation to all past and current students of Laboratory of Lightwave Instrumentation during my study here, for the friendly and supportive atmosphere that certainly helped me to carry out this research in a pleasant working environment. As well, my deep thanks to **Ms. Tomoko Sasaki** for giving me her support, friendship as well as language support in both English and Japanese.

Grateful acknowledgments are also extended to the Ministry of Education, Culture, Sports, Science and Technology of Japan (MEXT) for giving the opportunity and financial support to carry out the current study. In addition, I should convey my appreciation to the Egyptian Government for giving me the chance to pursue my graduate study at Hokkaido University; its support is greatly appreciated.

I am indebted especially to my husband **Mohamed Zakaria** who has borne a lot with me. I would like to gratitude him so much for his supporting, care, patience and understanding during my study. Also I give my thanks to my lovely sons, **Reyad** and **Eyad**, who could draw the smile on my face all the time through their growing. Finally, I am extremely grateful to **my beloved parents**, **uncles**, **brothers** and **sisters**, for their encouragement and sacrifices throughout the period of my educational career.

Samia Heshmat
Sapporo, JAPAN
March 2014

Abstract

Phase unwrapping is a crucial and challenging step to most data-processing chains based on phase information in many fields of research, such as magnetic resonance imaging, synthetic aperture radar interferometry and optical metrology. In all these research fields, the measured parameters are modulated in the form of two-dimensional fringe pattern. To retrieve the phase information from the fringe pattern, Fourier domain filtering or phase shift technique can be used. The retrieved phase values, which are wrapped phase, are the distribution of principal values ranging from $-\pi$ to π. Thus, phase unwrapping procedure is needed to get back the unknown multiple of 2π to each pixel. This is why many algorithms have been proposed for phase unwrapping. However, there is no agreement between the current phase unwrapping algorithms for different applications, due to the existence of disturbance in the measured phase data. In the case that there is no disturbance in the phase data, the unwrapped phase can be obtained by integrating the phase gradients over the whole data samples, which is independent from the integration path. However, there are several sources of errors in the phase images. Firstly, phase aliasing occurs when the true phase changes by more than one cycle (2π rad) between samples, which was caused by long baselines, objects discontinuities or high deformation. The second source is noise, which may be caused by speckle noise, electronic noise and/or fringe breaks. Those defected points in the measured phase images are called singular points (SPs). To exclude these invalid areas from unwrapping process and get precise unwrapped phase results can be a time-consuming process.

For this purpose, we proposed two novel phase unwrapping algorithms for noisy phase images. The first algorithm is called rotational and direct compensators for phase unwrapping (RC+DC). The RC+DC algorithm is a new phase unwrapping approach for noisy wrapped phase maps of continuous objects to improve the accuracy and computational time requirements of phase unwrapping using a rotational compensator (RC) method. The RC method uses local phase information to compensate the singularity parts of phase map caused by existence of SPs. It computes the compensators through superposing the effect of each SP by adding an integral of isotropic singular function along any loops. However, the RC method

has a drawback of undesired phase error because the RC should be applied to the regular region with no SPs as well as to the singular region. In addition, the RC method required high computational time cost when the measured phase data contains many SPs. Therefore, the proposed algorithm (RC+DC) aims to overcome the disadvantages of the RC method. It uses direct compensator (DC) for adjoining SP pairs, and uses RC for other pairs. The adjoining pair is a dipole which consists of two SPs with opposite signs, separated by one pixel horizontally or vertically. The RC+DC method is fast, however, its accuracy is not guaranteed. Its accuracy is depending on reducing the times for using the RC technique that increases the phase distortion in the unwrapped results.

The second proposed algorithm is based on singularity compensation for cluster regions of SPs; it aims to improve the performance of phase unwrapping using a localized compensator (LC) method regards the memory shortage and computational time requirements. The LC method regularizes the inconsistencies in local areas, which are clusters, around the SPs by integrating the solution of Poisson's equation for segments in each cluster to evaluate the compensators according to a certain mechanism. The original LC method uses boundary element method (BEM) to get the compensator values. However, BEM produce large error in the results when the singularity sources are position near to the segments which compensators are computed for them. Hence, the LC method also use singular value decomposition (SVD) to fix the errors produce from BEM step. We refer to the original LC method, which uses BEM and SVD method to obtain the compensator values, as LC.bem+svd. In terms of accuracy, the method using LC is superior to the other methods. Despite this, LC method has a major disadvantage of computational cost since this method requires long time cost to compute the compensator values and to reduce errors. Therefore, to overcome these drawbacks, we use a new way to produce the compensator values. The proposed algorithm solves the Poisson's equation by using rotational and divergence operators to get the compensators without any effect of the singularity source positions. Hence, the new proposed method does not need any further steps to fix errors. We called this new proposed method as LC phase unwrapping algorithm based on rotational and divergence operators (LC.rot+div). The proposed LC.rot+div algorithm is tested on both computer-simulated and experimental noisy phase data. The results show that the proposed LC.rot+div algorithm is faster compared to the original LC.bem+svd algorithm, meanwhile it keeps the same level of accuracy of the unwrapped results.

As a summary, the proposed phase unwrapping algorithms (RC+DC, and LC.rot+div) have been evaluated extensively using a set of simulated and experimental phase data obtained from various optical applications, such as interferometric data and Fourier transform profilometry data. In addition, these proposed algorithms are also compared to existing phase unwrapping methods, such as the method by Goldstein et al. and least-squares method with discrete cosine transforms .... etc. The results show that the proposed algorithms give better performances regards the accuracy and computational time cost. Therefore, the two new proposed phase unwrapping algorithms (RC+DC, LC.rot+div) are applicable for dynamic three-dimensional shape measurements and applications that are required large phase data size, such as computed tomography (CT) measurements.

Keywords: Interferometric measurements, Three-dimensional shape measurements, Holographic data, Fringe analysis, Phase extraction, Phase unwrapping, Image processing.

Abbreviations

CCD	Charge-coupled device
S/N	Signal-to-Noise ratio
SP	Singular Point
FTP	Fourier Transform Profilometry
VSP	Virtual Singular Point
PDE	Partial Differential Equation
FT	Fourier Transform
DCT	Discrete Cosine Transform
FFT	Fast Fourier Transform
LS-DCT	Least-Square method by using Discrete Cosine Transform
SSPU	Spreading Singularity Phase Unwrapping
RC	Rotational Compensator
USP	Unconstrained Singular Point
DC	Direct Compensator
LC	Localized Compensator
BEM	Boundary Element Method
SVD	Singular Value Decomposition
CT	Computed Tomography

Symbols

$I(x, y)$	The intensity recorded on the CCD at (x, y) point,
$\Psi(x, y)$	The value of the wrapped phase,
f_0	The spatial-carrier frequency,
$\phi_0(x, y)$	The phase of the background zebra pattern,
$\phi(x, y)$	The phase of the distorted fringe pattern,
$\Delta\phi(x, y)$	The phase caused by the object's height distribution,
Ψ_i	The value of the wrapped phase at pixel i in phase map,
$\Delta\Psi^i$	Wrapped phase difference at pixel i in phase map,
W[.]	Wrapping operator, where $-\pi \leq W[.] \leq +\pi$,

Int[.]	A function that returns the nearest integer
$\nabla\Psi^i$	Wrapped phase gradient at pixel i in phase map,
Φ_M	The estimated unwrapped phase at point M,
S	The SP residue,
$\Phi_{i,j}$	The estimated unwrapped phase,
$\nabla\Psi^x_{i,j}$	Horizontal wrapped phase gradient in x direction,
$\nabla\Psi^y_{i,j}$	Vertical wrapped phase gradient in y direction,
ε^2	Minimum discontinuity error in L^2-norm sense,
Q	Matrix that perform the discrete Laplacian operation,
Φ	Column vector containing the unwrapped phase values which is the solution,
ρ	A column vector containing the discrete Laplacian operation on the wrapped phase differences,
$w^x_{i,j}$	Horizontal weightings,
$w^y_{i,j}$	Vertical weightings,
W	Matrix of weight values of every pixel in the phase map,
$\boldsymbol{g}(\boldsymbol{r},\boldsymbol{r}')$	The wrapped phase difference vector between two adjoining pixels,
$\boldsymbol{r}$, $\boldsymbol{r}'$, and $\hat{\boldsymbol{s}}$	The position of the pixel of interest, position of the adjoining pixel, and unit vector of direction $\boldsymbol{r}'-\boldsymbol{r}$, respectively,
m_k	Residue point value $m_k \in \{-1,0,1\}$,
K	A sum of the number of that not satisfying the sampling theorem,
$\boldsymbol{A}$	A rotational vector that is a rotation of a vector potential,
(R,θ,z)	The cylindrical coordinate,
$\boldsymbol{e}_R$ and $\hat{\boldsymbol{z}}$	Unit vectors for R-axis and z-axis, respectively,
$\hat{\boldsymbol{n}}$	The outward normal unit vector to the path ($\hat{\boldsymbol{n}}=\hat{\boldsymbol{s}}\times\hat{\boldsymbol{z}}$)
$\boldsymbol{E}_{\text{monopole}}$	The effect of a single SP,
$\boldsymbol{E}_{\text{dipole}}$	The effect of the dipole SPs in two dimensional space,
$\boldsymbol{d}$	The difference vector from the negative SP to the positive SP,
$\bar{\phi}$ and $\delta\phi(\boldsymbol{r})$	A phase average and a non-singular phase fluctuation, respectively,
C^i	A compensator regularizes the singularity of Ψ^i,
${}^RC^i_j$	The RC for the i-th segment to cancel the singularity of the j-th SP,

S_j	The residue of the j-th SP,
$\theta_{i+1,j}$ and $\theta_{i,j}$	Azimuthal angles of both ends of the i-th segment,
${}^{D}C_j^i$	The DC of a segment that is related to the adjoining pair,
T_j^i	The sign direction of ${}^{D}C_j^i$,
$adj^+(i)$	The positive SP number which belongs to the adjoining pair,
$adj^-(i)$	The negative SP number which belongs to the adjoining pair,
i	the segment number,
m_j^i	is defined, $m_j^i = 1$, when $adj^+(i)$ or $adj^-(i)$ has a value of j; otherwise $m_j^i = 0$,
$\hat{\boldsymbol{z}}$	The perpendicular unit vector to the domain surface,
A_z	The flux density that describes the spreading of singularities,
$\boldsymbol{e}_{k,j}$	The error vector on the j-th segment in the k-th elementary loop,

Contents

Dedication **iii**

Declaration **v**

Acknowledgements **vii**

Abstract **ix**

Abbreviations **xiii**

Table of Contents **xvii**

List of Figures **xix**

List of Tables **xxv**

1 Introduction **1**
1.1 Phase extraction 4
1.2 Phase unwrapping 5
1.3 Objective of study 11
1.4 Synopsis of the thesis 12

2 Background of phase extraction and unwrapping processes **13**
2.1 Introduction 15
2.2 Phase extraction and calculation 16
2.2.1 Phase extraction for interferometric measurements 16
2.2.2 Phase extraction for Fourier transform profilometry measurements . . 18
2.3 Phase unwrapping 21
2.3.1 Phase unwrapping definition 21
2.3.2 Singular points and branch cuts 23
2.4 Existing phase unwrapping algorithms 26
2.4.1 Path following methods 27
2.4.2 Least squares based methods 30
2.5 Conclusions 34

3 Phase unwrapping algorithm by using rotational compensator **37**
3.1 Introduction 39
3.2 Rotational compensator phase unwrapping method 39
3.2.1 Rotational compensator technique 40
3.2.2 Unconstrained singular point positioning 43

3.2.3 Virtual singular points 46
3.3 Results and discussion 49
3.3.1 Simulated phase data 49
3.3.2 Unwrapping for interferogram data 54
3.4 Conclusions 56

4 Rotational and direct compensators phase unwrapping algorithm 57
4.1 Introduction 59
4.2 Basic concepts 59
4.3 Direct compensator technique 61
4.4 Phase unwrapping by rotational and direct compensators algorithm 64
4.5 Results and discussion 66
4.5.1 Computer simulation results 66
4.5.2 Experimental results 70
4.6 Conclusions 80

5 Localized compensator based on rotational and divergence operators for unwrapping 81
5.1 Introduction 83
5.2 Phase unwrapping compensation methods 83
5.3 Proposed localized compensator method based on rotational and divergence operators (LC.rot+div) 86
5.3.1 The principles of the Localized compensator technique 87
5.3.2 Clustering 92
5.3.3 BEM to solve Poisson's equation 92
5.3.4 The description of the proposed algorithm (LC.rot+div) 100
5.4 Results and discussion 103
5.4.1 Simulated wrapped phase for known phase map 104
5.4.2 Experimental data obtained by interferometer 107
5.5 Conclusions 109

6 Conclusions 111

Bibliography 117

List of Figures

1.1 Fringe analysis for an object 4
1.2 Concept of phase unwrapping technique 6
1.3 One-dimensional phase unwrapping examples: (a) successful example with sufficient sample points number is 35; (b) unsuccessful example with insufficient sample points number is 33, which is slightly under Nyquist rate; (c) unsuccessful example with insufficient sample points number is 18. 8
1.4 One-dimensional phase unwrapping noisy examples: (a) successful example has noise with magnitude 0.1 and sample points number is 35; (b) unsuccessful example has noise with magnitude 0.2 and sample points number is 35. . 9

2.1 A schematic diagram of an experimental setup system of the interferometer technique measurement. 16
2.2 Procedure for calculating the phase from an interferogram: FT Fourier transformation, FT^{-1} inverse Fourier transformation, the $I(x, y)$ is a fringe pattern for interferometric data, the $\widehat{I}(k_x, k_y)$ shows Fourier spectrum of the fringe pattern, the $F(k_x, k_y)$ shows the filtering function, the $\widehat{I}_F(k_x, k_y)$ shows the filtered spectrum, the $W\{\Phi(x, y)\}$ is the wrapped phase modulation. 18
2.3 Experimental setup of three-dimensional shape measurement system. (a) geometry for the projecting and imaging grating pattern on the object, (b) sketch map for projected light pattern. 20
2.4 Elementary path in two-dimensional coordinate for visualizing SP identification: the white circles denote points at which the phase values are defined, the thick arrows denote the direction of the path around the tested SP, the black circle illustrates the position of the tested SP. 23
2.5 Unwrapping path with the existence of the branch cuts in the phase map: the thick dashed line denotes the branch cut that connects two of opposite sign SPs, the thick arrow shows the direction of unwrapping path; (a) incorrect unwrapping path, (b) correct unwrapping path. 24
2.6 Schematic figure shows SPs types: (a) one pixel apart dipole SPs generated by phase noise, (b) dipole SPs generated by phase noise several pixels apart, (c) dipole SPs generated by discontinuous objects and under-sampling have the tendency of lying far apart from each other and (d) & (e) are monopole SPs. 26
2.7 Spreading of errors in regular regions due to the Goldstein method handling way for the singularity regions in the phase map: (a) SPs distribution map, (b) correct placement of branch cuts, (c) incorrect placement of branch cut lines and phase errors appear in regular regions. 28

2.8 Spreading of errors in regular regions due to the LS-DCT method handling way for the singularity regions in the phase map: (a) SPs distribution map, (b) phase errors appear in regular regions. 32
2.9 Schematic of the singularity spreading phase unwrapping: (a) singular point, (b) compensator, (c) spread singularity. 33
2.10 Spreading of errors in regular regions due to the SSPU method handling way for the singularity regions in the phase map: (a) SPs distribution map, (b) phase errors appear in regular regions. 34

3.1 Configuration to compute the rotational compensator 43
3.2 Elementary path including an unconstrained singular point: The $\Delta\theta_l$ means the facing angle of the side with the ends $\boldsymbol{r}_l$ and $\boldsymbol{r}_{l+1}$. The $\Delta\Phi_l$ means the difference of the wrapped phases. 45
3.3 Spreading of errors in regular regions due to the RC method handling way for the singularity regions in the phase map: (a) SPs distribution map, (b) phase errors appear in regular regions. 46
3.4 Determination of dipole pairs: (a) definition of the virtual SP candidates, each dashed arrow shows the correspondence between original and virtual SP; (b) search nearest SP and pairing in the first iteration: each arrow shows the nearest opposite-signed SP, the SPs encircled are paired as dipoles, the checked virtual candidate is removed from the list of candidates in subsequent steps; (c) the second iteration: SPs enclosed with dashed ellipse have been already paired; (d) elimination of removable virtual SP pairs. 47
3.5 Unwrapped and rewrapped phase map of simulated phase data has noise with $\sigma = 0.15$ cycle: In each figure, the left-hand side figure shows original or unwrapped phase map where phase increases with increasing of brightness, and the right-hand side figure shows wrapped or rewrapped phase map. (a) original phase map, (b) Goldstein's path-following method, (c) least squares method with DCT, (d) RC method. 50
3.6 Frequency histogram for distance from a positive SP to the nearest negative SP. 51
3.7 Unwrapped phase results with contour lines for simulated noisy data with 0.15 cycle standard deviation, obtained when uses: (a) RC technique only, (b) RC technique with using USP approach only, (c) RC technique with using VSP approach only, (d) RC technique with using both USP and VSP approaches. . 53
3.8 Computational time: The horizontal axis N denotes one-dimensional area size in pixels. The computational time is measured with a PC including CPU of Intel Core 2 DUO (TM) with 2.13GHz clock in a single CPU operation mode. 54
3.9 Unwrapped phase of fringe by Mach-Zehnder interferometer for candle flame: (a) fringe pattern obtained with existence of flame, (b) wrapped phase map obtained by Fourier domain method, (c) SPs distributions, (positive and negative SPs are represented by white and black dots, respectively), (d) & (e) unwrapped and rewrapped phases map obtained by LS-DCT method, (f) & (g) unwrapped and rewrapped phases map obtained by the developed RC method. 55

4.1 Example of dipole distance distribution: the dipole distance is defined as the distance between one SP and the closest SP with opposite polarity. 62

4.2 The existence of the branch cuts between the adjoining SPs and the concept of direct compensation: the thick dashed line denotes the branch cut that connects two SPs of opposite sign, compensator position is denoted by thick arrow, the thin arrows show the direction and distribution of compensators for the segments of each SP where S and S' denote the residues of the SPs. . . . 63

4.3 Complex cases for the position patterns of SP pairs and the direct compensators for the adjoining SPs pairs: (a) SPs are distributed in discrete values, (b) SPs are distributed by using USP technique; in (b) the thick dashed line denotes the branch cut that connects two SPs of opposite sign and also shows the direct compensator positions are denoted by thick arrows. 64

4.4 Spreading of errors in regular regions due to the proposed method (RC+DC) handling way for the singularity regions in the phase map: (a) SPs distribution map, (b) phase errors appear in regular regions. 66

4.5 A comparison of the unwrapped phase results for simulated phase data has noise with $\sigma = 0.15$ cycle: (a) the original phase data, (b) the wrapped data, (c) the positions of all SP pairs, (d) the positions of the pairs of non-adjoining SPs, (e) the positions of the pairs of adjoining SPs, (f) unwrapped result by LS-DCT, (g) unwrapped result by RC, and (h) unwrapped result by RC+DC. In (a), (b), and (f)-(h), the phase increases with the increases of brightness. In (f)-(h), contour lines of the phase with the interval of one cycle are also shown. 67

4.6 Required computational time of each algorithm for various image sizes: The horizontal axis N denotes one-dimensional area size in pixels. "RC" shows the required time cost for RC method, "RC+DC" shows the required execution time for the proposed method, and "LS-DCT" shows the required time cost for LS-DCT method. The computational time is measured with a PC including an Intel Core 2 DUO CPU with 2.13 GHz clock in the single CPU operation mode. 69

4.7 Unwrapped phase result of experimental data for candle flame: (a) the wrapped data, (b) SPs distribution map, (positive and negative SPs are represented by white and black dots, respectively); (c) the unwrapped result of RC algorithm, (d) the unwrapped result of RC+DC, ... 71

4.8 The way of an object extraction from experimental data: (a) pre-rejection of background. (b) Post-rejection of background. 73

4.9 A comparison of the accuracy of the examined phase unwrapping algorithms' results of candle flame for **pre-rejection** of background way to extract the object. The left column shows the unwrapped phase results. The right column shows the rewrapped phase results. (a) results obtained by Goldstein et al. method, (b) results obtained by Flynn method, (c) results obtained by LS-DCT method, (d) results obtained by RC+DC method. 74

4.10 A comparison of the accuracy of the examined phase unwrapping algorithms' results of candle flame for **post-rejection** of background way to extract the object. The left column shows the unwrapped phase results. The right column shows the rewrapped phase results. (a) results obtained by Goldstein et al. method, (b) results obtained by Flynn method, (c) results obtained by LS-DCT method, (d) results obtained by RC+DC method, ... 75

4.11 Experimental measured data: (a) deformed grating image, (b) wrapped phase image, and (c) map of distribution of SPs. 78

4.12 Comparison of the accuracy of the examined phase unwrapping algorithms' results for the measured data: the first row shows the unwrapped phase shift of the object, the second row shows the rewrapped phase shift of the object, the third row shows the cross-sectional profile of the object's height. (a), (c), and (e) show the results of Flynn's method. (b), (d), and (f) show the results of RC+DC algorithm. 79

5.1 Schematic of rotational compensator phase unwrapping method: the singularity of $j-th$ SP is canceled by computing the RC of $i-th$ segment using eq. (5.1). 84

5.2 Schematic of rotational and direct compensator phase unwrapping method: (a) defined SPs, (b) create SPs pairs and defined adjoining and nonadjoining pairs, (c) add DC for adjoining pairs and compute RC for nonadjoining pairs. 85

5.3 Spreading of errors in regular regions due to the handling way of the LC method for the singularity regions in the phase map: (a) SPs distribution map, (b) phase errors appear in regular regions. 86

5.4 A flowchart of the original LC method (LC.bem+svd) shows the two main steps for this method. 87

5.5 Example of two adjacent loops have two SPs with opposite polarity, presenting the compensator value for the internal segment. 88

5.6 Definition of local domain and flux density around SPs: (a) local domain including SPs, (b) flux distribution in the local domain. Outmost closed thick line is a boundary of the local domain, and the grids are segments of elementary loops. The dashed line in (a) represents concave polygon that contains all SPs. The arrows in (b) are the flux density of which line width expresses the magnitude. 91

5.7 Schematic of BEM to solve flux density A_z: shows the steps of BEM to compute the flux, the condition in boundary Γ is $\hat{\boldsymbol{n}} \cdot \nabla A_z = 0$, and for internal point inside the specific domain is, $A_z(\boldsymbol{r}_i) = \int_{\Gamma_i} (\nabla A_z^* \cdot \hat{\boldsymbol{n}}) A_z \, d\Gamma + \sum_k S_k A_z^*$. 95

5.8 An example of unwrapped phase results for simulated phase data has noise with standard deviation 0.15 cycle, to show the errors produce when use BEM only for the old LC method: (a) original phase data, (b) wrapped data, (c) SPs distribution map (positive and negative SPs are represented by white and black dots, respectively), (d) unwrapped result of the old LC method by using BEM only, (e) unwrapped result obtained by the old LC method using both BEM and SVD, (f) errors generated due to using of BEM only for unwrapped result the range of values is $[-0.3\pi : 0.4\pi]$, and (g) errors generated due to using both BEM and SVD to produce unwrapped result the range of values is $[-0.3\pi : 0.3\pi]$. In (a), (b), and (d), (e), the phase increases with the increases of brightness. In (d), (e), contour lines of the phase with the interval of one cycle are also shown. 96

5.9 An example of unwrapped phase results for simulated phase data has noise with 0.2 cycle standard deviation to show the errors produce when use BEM only for the old LC method: (a) original phase data, (b) wrapped data, (c) SPs distribution map (positive and negative SPs are represented by white and black dots, respectively), (d) unwrapped result of the old LC method by using BEM only, (e) unwrapped result obtained by the old LC method using both BEM and SVD, (f) rewrapped result of the old LC method by using BEM only, (g) rewrapped result obtained by the old LC method using both BEM and SVD, (h) errors generated due to using of BEM only for unwrapped result the range of values is $[-0.06\pi : 1.8\pi]$, and (i) errors generated due to using both BEM and SVD to produce unwrapped result the range of values is $[-0.05\pi : 1.3\pi]$. 99

5.10 Accuracy comparison for unwrapped phase results of experimental data for candle flame: (a) wrapped data, (b) SPs distribution map (positive and negative SPs are represented by white and black dots, respectively), (c) unwrapped result of the RC+DC method, (d) unwrapped result of the old LC method by using BEM only, and (e) unwrapped result obtained by the old LC method using both BEM and SVD. In (c), (d) and (e), contour lines of the phase with the interval of one cycle are also shown. 100

5.11 A schematic for the proposed algorithm to illustrate the way for solving Poisson's equation to compute the flux values. This way uses rotational, ($\nabla\times$), and divergence, ($\nabla\cdot$) operators to produce the flux density values directly without any integration to evaluate the compensators. 102

5.12 A flowchart of the proposed algorithm (LC.rot+div). 103

5.13 A comparison of the unwrapped phase results for simulated phase data has noise with $\sigma = 0.2$ [cycle]: (a) the original and wrapped phase data, (b) the unwrapped and rewrapped results obtained by the old LC method (LC.bem+svd), (c) the unwrapped and rewrapped results obtained by the proposed modified LC method (LC.rot+div), (d) the phase difference between the unwrapped results the range of values is $[-0.1\pi : 0.2\pi]$. The left side in (a) to (c), the phase increases with the increases of brightness. 105

5.14 Required computational time of each algorithm for various image sizes: The horizontal axis N denotes one-dimensional area size in pixels. "LC.bem+svd" shows the required time cost for the old LC method, and "LC.rot+div" shows the required execution time for the proposed method. 106
5.15 The maximum cluster size for various image sizes: The horizontal axis N denotes one-dimensional area size in pixels. 107
5.16 Unwrapped phase results of experimental data for candle flame: (a) wrapped data, (b) SPs distribution map (positive and negative SPs are represented by white and black dots, respectively), (c) unwrapped result of the old LC method (LC.bem+svd), and (d) unwrapped result obtained by the proposed method (LC.rot+div). In (c) and (d), contour lines of the phase with the interval of one cycle are also shown. 108

List of Tables

3.1 Accuracy comparison among algorithms by planar function fitting for the simulated phase data with 0.1 [cycle/pixel] constant gradient and has noise with 0.15 [cycle] standard deviation. 'RC(only)' represents the case when the unwrapped result is obtained by using RC technique only; 'RC(USP)' in the case of using RC and USP techniques; 'RC(VSP)' when uses RC and VSP techniques; while 'RC(USP+VSP)' represents the case when using all technique (RC, USP, VSP) to obtain the unwrapped result. 52

4.1 A comparison of the accuracy for the simulation data, shown in Fig. 4.5. . . . 68
4.2 A comparison of the execution time cost between RC algorithm and the proposed RC+DC algorithm: The T_{ovrh} presents the required execution time for overhead procedure to search and analyse SPs' distribution. The T_{comp} presents the required execution time to compute the Compensators. The T_{total} is the summation, $T_{total} = T_{ovrh} + T_{comp}$. N_s and N_a, denote the total number of SPs and the number of SPs that form adjoining pairs, respectively. "Saving time ratio" $= 1 - T_{(RC+DC)}/T_{RC}$; where T_{RC} and $T_{(RC+DC)}$, represent the total execution times for RC method and the proposed method, respectively. . 72

5.1 A comparison of the accuracy for the simulated noisy data with 0.15 cycle standard deviation, shown in Fig. 5.8; "LC.bem" is the old LC method by using BEM only, and "LC.bem+svd" is the old LC method by using both BEM and SVD. 97
5.2 A comparison of the accuracy for the simulated noisy data with 0.2 cycle standard deviation, shown in Fig. 5.9; "LC.bem" is the old LC method by using BEM only, and "LC.bem+svd" is the old LC method by using both BEM and SVD. 98
5.3 A comparison of the accuracy for the simulation data, shown in Fig. 5.13; "LC.bem+svd" is the old LC method, and "LC.rot+div" is the proposed method. 104

6.1 Accuracy and computational time cost comparisons among the studied algorithms, for two examples of simulated noisy phase data. 115

CHAPTER 1

INTRODUCTION

- Phase extraction
- Phase unwrapping
- Objective of study
- Synopsis of the thesis

Chapter 1
Introduction

Optical measurement techniques such as interferometry and fringe projection profilometry have become crucial tools in many areas of science and engineering. Since these techniques have the features of non-contact characteristics and highly accurate measurement capability. However, most optical methods require the processing of a fringe pattern. The intensity of the fringe pattern which is produced by these optical methods modulates the physical quantity that is measured. This intensity varies as the cosine of a phase which is most often directly proportional to that physical quantity. Thus, the accuracy of measurements carried out by these optical methods is strongly dependent on the accuracy with which the underlying phase distribution of the recorded fringe patterns is estimated. Different methods are used to demodulate fringe patterns in order to obtained the desired information. These method are referred as fringe pattern analysis techniques [1–5]. Any of these fringe analysis algorithms can be divided into two main processing stages: phase extraction and phase unwrapping. The frist stage is to extract the phase information from the fringe pattern, Fourier domain filtering [5–7] or phase shift techniques [6, 8, 9] can be used for that. The extracted phase values, which are wrapped phase, are the distribution of principal values ranging from $-\pi$ to π. Thus, phase unwrapping procedure is needed to get back the unknown multiple of 2π to each pixel, which is the second main stage in any fringe analysis method. However, the defects in the fringe patterns, such as phase discontinuity, shadow, and/or noise are the main difficulties in the phase unwrapping methods. To exclude these invalid areas from unwrapping process and get precise unwrapped phase results can be a time-consuming process. Despite no small numbers of methods to estimate unwrapped phase map have been proposed, the problem of phase unwrapping remains unresolved.

Fringe analysis techniques are considered to be an effective and reliable optical noncontact methods for surface shape measurements. In these techniques, a structured lighting pattern is projected onto the surface of an object. According to the surface shape of the object, the

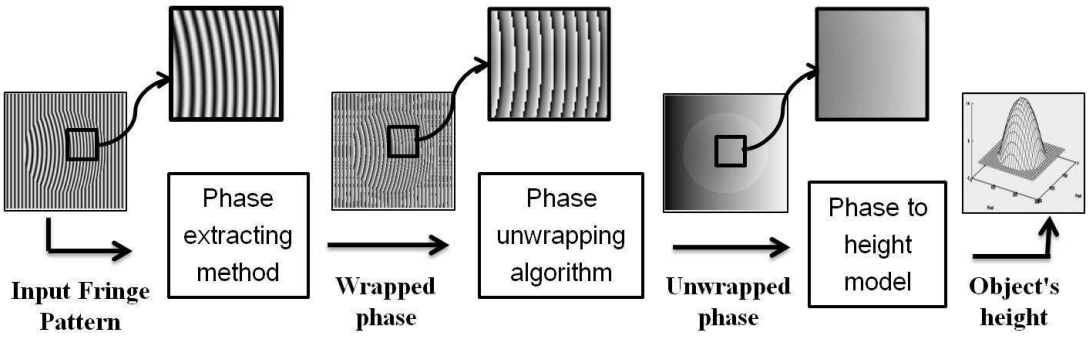

Figure 1.1: *Fringe analysis for an object*

projected pattern will be modified. This pattern is captured by a CCD camera and then stored into computer memory. The image is then analyzed by one of fringe analysis algorithms to extract the phase information and retrieved the continuous form of the phase distribution by applied one of phase unwrapping methods. Finally, by using phase-height relationship, the object height shape can be determined. Figure 1.1 summarized these steps about fringe patterns analysis.

Driven by these motivations, both theoretical aspects of the phase unwrapping problem as well as practical algorithms for its solution is examined in this dissertation. However, we begin with a brief explanation for the main stages of fringe analysis methods to figure out the problems of phase processing and the circumstances in which they arise.

1.1 Phase extraction

Many techniques have been proposed for the analysis of fringe patterns. These techniques vary in accuracy, the number of frames required and processing time. The aim of any fringe pattern analysis algorithm is to obtain the phase information modulated into the fringe pattern. This phase is wrapped between $[-\pi, \pi)$ and needs to be unwrapped, as will be shown in the next section. Fringe pattern analysis algorithms can be classified into two categories, which are spatial and temporal techniques. Spatial methods calculate the phase of a pixel in a fringe pattern depending on its neighboring pixels. Examples of a spatial technique such as Fourier fringe analysis and direct phase demodulation. Spatial techniques require at least one fringe

pattern to calculate the phase components. In contrast, temporal algorithms require at least three images to calculate the phase of a pixel depending on the values of that pixel in different images and independent of its surrounding pixels. An examples of a temporal methods is phase stepping. However, in this study our main concerning is for the unwrapping stage in the analysis of fringe pattern process. This is why we will present only one of famous fringe analysis technique for phase extraction stage in chapter 2, which is Fourier fringe analysis method.

1.2 Phase unwrapping

Phase unwrapping is a technique used on wrapped phase images to remove the 2π discontinuities embedded within the phase map. It detects a 2π phase jump and adds or subtracts an integer offset of 2π to successive pixels following a threshold mechanism, thus, retrieving the contiguous form of the phase map. To clarify the concept of phase unwrapping technique consider an example for one-dimensional data as shown in Fig. 1.2. The actual phase data shown by the solid line is continuous function; it has values greater than 2π. The measured phase (wrapped phase) shown by square symbol is detected at discrete point, its values stored in the range $(-\pi, \pi]$. From the figure, it can be found that the wrapped phase has phase jumps because it represents the fractional part of the unwrapped phase. The filled diamond symbol is the unwrapped phase calculated from wrapped phase by applying a certain process to remove the gaps.

Phase unwrapping is not a straightforward step because of the possible presence of different error sources and problems. Figure 1.3 shows examples of one-dimensional phase unwrapping to illustrate the effect of phase aliasing or insufficient sampling rate on the unwrapping process. In the figure, the true unwrapped phase, which is associated with a physical quantity, is shown by solid line. The measured phase, which is wrapped phase shown by square symbol, is detected at discrete point. The range of these phases is within $[0, 1)$ [cycle]. The filled diamond symbol is the unwrapped phase calculated by adding or subtracting an integer offset of 2π to the previous successive point. According to sampling theory, more than two samples per period of the highest frequency component must be obtained. The Nyquist rate defines

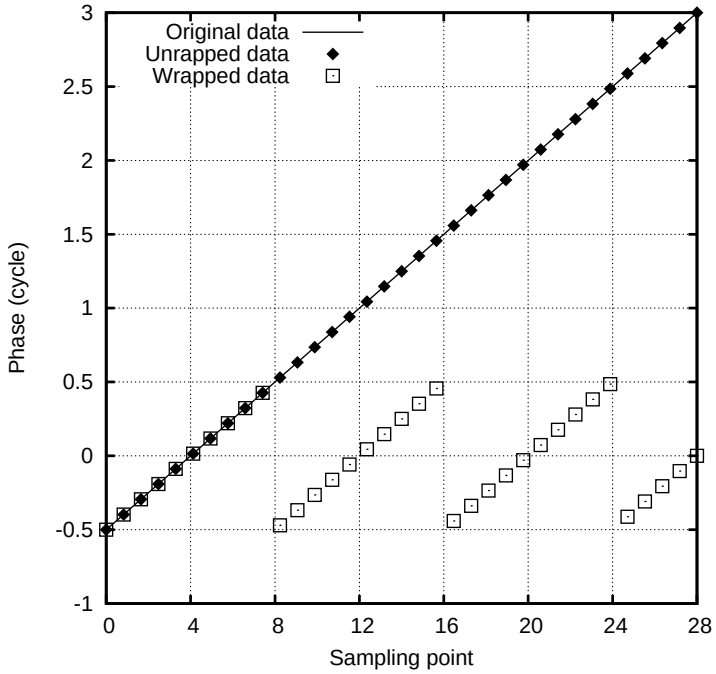

Figure 1.2: *Concept of phase unwrapping technique*

this minimum sampling rate [10]. Alternatively, sampling at the Nyquist rate is equivalent to constraining the phase change to less than 0.5 cycle or π radian per sample everywhere. In order to perform the phase unwrapping process in this example, the difference between a sample and the preceding sample (directly adjacent on its left) is calculated. When this difference is larger than $+\pi$ or smaller than $-\pi$, a wrapped phase is detected. Once the detected wrapped phase is found, the value of 2π is either added or subtracted to or from this sample and also all the further samples to the right-hand side of this sample. Figure 1.3(a) shows a successful case for phase unwrapping process. This is due to that the number of sampling points,which is 35, is greater than Nyquist rate. It is clear that positive cycles are applied at the fifth and seventh point in Fig. 1.3(a), as well as, negative cycles are applied around the position of 4.2 and 5.0. Meanwhile, Fig. 1.3(b) shows the result for unsuccessful unwrapping process case, in which the number of sampling points is slightly under the Nyquist rate. Comparing results in Fig. 1.3(a) and that one shown in Fig 1.3(b), it can be found that the sixth point in Fig. 1.3(b) got a negative cycle at the sixth point, this result has error at this point. Furthermore, since the unwrapping is applied to the rightward direction, the unwrapped phase results in the right-

hand side region of this point show incorrect results. The reason for such incorrect results is due to shortage of sampling points. However, considering a boundary condition such as the unwrapped phase must be zero at both ends, it can be found that at least one unwrapping error is included at any point in the region, which is called inconsistency in subsequent descriptions. This additional condition (boundary condition) plays an important role to fix the unwrapping errors. Figure 1.3(c) shows the number of sampling points is the smallest among the studied cases. It shows that the unwrapped phase is not identical to the true phase. However, any inconsistency cannot be detected from the boundary condition. It means that the number of incorrect adding cycles with $+1$ is equal to that with -1, and the result seems good. It can be concluded that consistency is one of requirements but not a sufficient condition.

Figure 1.4 shows examples for one-dimensional phase unwrapping process in case where the data contains noise with different magnitudes 0.1 and 0.2 cycles, respectively. The noise is applied before phase measurements. In the figure, the true phase with noise is shown by dotted line. The result of Fig. 1.4(a) shows that the phase unwrapping is completed successfully. However, Fig. 1.4(b) shows incorrect unwrapped phase result, this is due to that the noise ratio is too high. Also, it can be detected that there is inconsistency by considering the boundary condition at the ends of region as similar to the case of shortage of sampling points. Also, when the magnitude of noise is grater than 0.5, it is worth to mention that the phase unwrapping cannot be applied.

Therefore, from last examples we can summarize the problems that affect the phase unwrapping process as follow:

- Low S/N ratio of the fringes caused by electronic noise, speckle noise.
- Violation of sampling theorem.
- Object discontinuities.

As a result, many phase unwrapping algorithms have been developed in an attempt to solve these problems. However, the variety of forms and densities for the noise that might be found in real wrapped phase maps makes the problem of phase unwrapping more complex and difficult to solve, even with given the significant amount of research effort expended to date

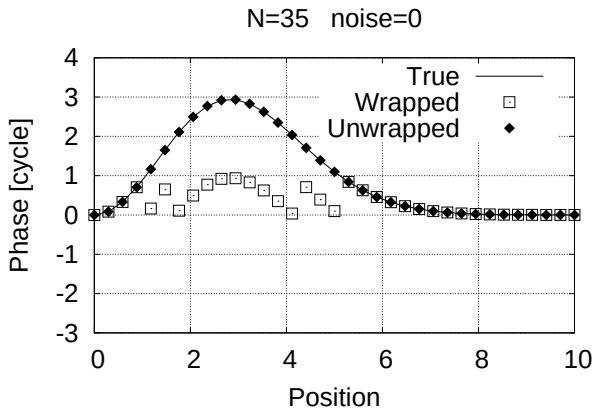

(a)

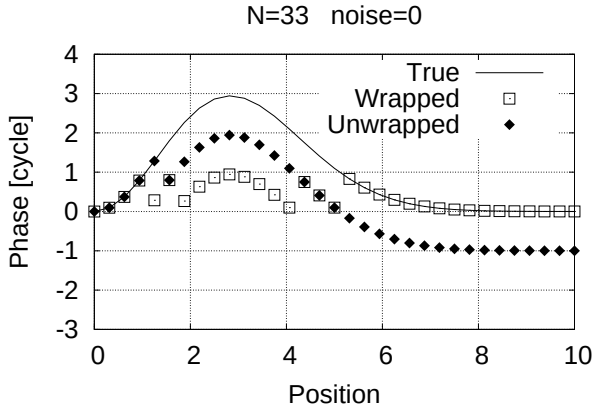

(b)

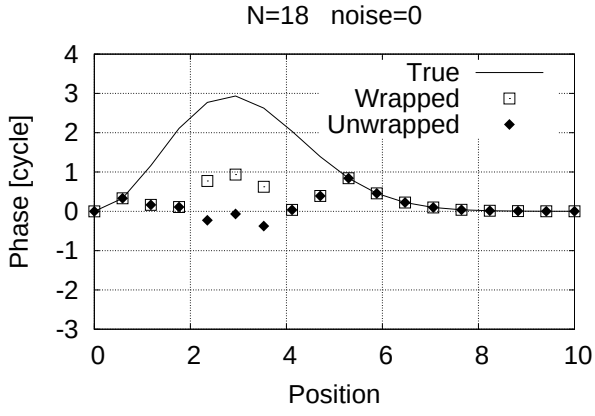

(c)

Figure 1.3: *One-dimensional phase unwrapping examples: (a) successful example with sufficient sample points number is 35; (b) unsuccessful example with insufficient sample points number is 33, which is slightly under Nyquist rate; (c) unsuccessful example with insufficient sample points number is 18.*

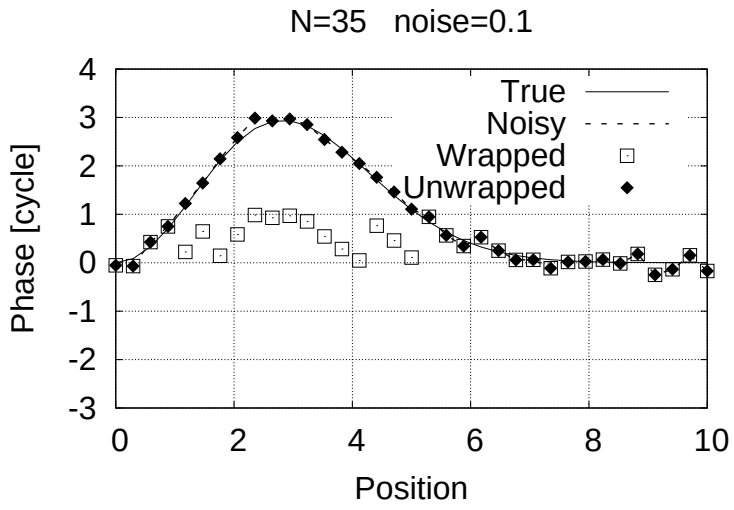

(a)

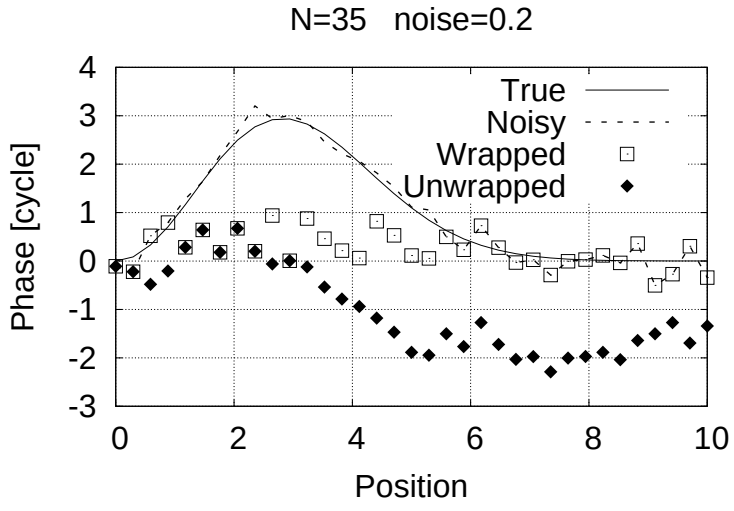

(b)

Figure 1.4: *One-dimensional phase unwrapping noisy examples: (a) successful example has noise with magnitude 0.1 and sample points number is 35; (b) unsuccessful example has noise with magnitude 0.2 and sample points number is 35.*

and the large number of existing phase unwrapping algorithms. Although various methods to estimate a correct unwrapped phase map have been proposed, they can be divided into three categories. The first category contains algorithms based on following the paths [11–18]. These methods involve integrating the phase gradient of pixels in an image over a path starting from a certain point and going over all the pixels, in essence, unwrapping the image. Path independent unwrapping is obtained in the absence of error sources (singular points) that can arise from either noise or object discontinuities. The unwrapped result is independent of the unwrapping path; hence, the complete phase map is consistent. However, in the presence of corrupted pixels (singular points), taking just any path is not possible anymore. Consequently, unwrapping becomes path dependent, where it has to manoeuvre between pixels choosing the best path to follow where the pixels are not corrupted by error. To overcome path dependence, many ways have been suggested and implemented. Hence, it can be said that path following methods fist search for singular points (SPs), then pair these SPs by placing branch cuts. By examining the branch cuts and determining if any appear to be placed poorly or any isolate a region, it can be determined whether or not the paths can be followed to retrieve the phase maps, as well as whether these methods succeed or fail.

The second category includes the methods which use the least-squares approach [19–25]. These algorithms use a different way for unwrapping images while still using the estimated phase gradient. They use the same idea of minimization of discrete gradients difference squares as used in the leased-squares approach. These differences are taken between the wrapped phase gradients and supposed unwrapped phase gradients. In these methods, a smooth solution is achieved by the resultant minimization. That can be done by integrating over all the possible paths within the image not like path following methods, which integrate over one single path, thus, spreading the error over the whole image. Like the previous methods, these methods also encounter a large number of errors once a corrupted region is present in the image. Hence, weighting parameters are introduced to exclude corrupted regions. However, the success of algorithms using such a method relies on choosing the weights, which puts a huge load on the performance of the algorithm. One advantage of these methods over algorithms based on following the paths is unwrapping SPs rich regions.

The last category is denoising-unwrapping methods [26–31]. This type of methods performs

phase map denoising to remove noise from wrapped phase by using a filtering process. The filtering process is sometimes applied before the unwrapping process such as windowed Fourier transform method [28], or it is applied simultaneously with the unwrapping process such as dynamic filter method [29, 30]. These methods can reduce the noise within the original spatial resolution. However, they have a minimum signal-to-noise ratio for the wrapped phase data in which this method start to fail to obtain accurate unwrapped phase result. In addition, the unwrapped results of these methods are highly depending on relaxation parameter, which can control the cut-off frequency of the filter.

1.3 Objective of study

Current interest in two-dimensional phase unwrapping has been motivated largely by coming on techniques based phase measurements. In these measurements, properties of two or more waves are diagnosed by studying the pattern of interference created by their superposition, and depending on how the data are processed. However, the data must usually be unwrapped before they can be made useful. In fact, incorrect phase unwrapping is often the most significant source of error in these measurements. For this reason, the main objective of this research study is the development of accurate, efficient, and robust phase unwrapping algorithms for wrapped noisy images obtained from various optical applications. We propose new methods to compensate the inconsistencies and to confine the effect of each one in a local region, however, they do that in different ways. The unwrapped results of these proposed methods are similar to that of the methods based on the least square methods. However, the unwrapping is carried out along successive pixels as similar to the path following methods. To achieve the main object of this study, the following steps are done:

- Investigate and demonstrate the phase unwrapping process and problems deeply. In addition, a brief overview of the existing phase unwrapping methods and ideas should be provide. Then, programming these existing phase unwrapping algorithms is generated.

- Figure out the ideas and prove them to propose efficient and accurate unwrapping algorithms. Then, implement these new ideas to have applicable phase unwrapping algo-

rithms in reality. After that, examine the proposed algorithms for simulated and actual phase data to check their performance.

- Carry out comparisons between the proposed algorithms and the existing phase unwrapping algorithms to evaluate the quality and validity for the unwrapped images taking in consideration the noise level and time cost for the simulated data. Furthermore, comparison for these algorithms is done for experimental phase data obtained from various applications to examine the applicability and validity of these methods for actual phase data.

1.4 Synopsis of the thesis

Chapter 1 is an introduction to the research by throwing the light on the subject and main objectives of the study. In chapter 2, a background about phase extraction and unwrapping is presented. In addition, a brief study for some of the existing phase unwrapping algorithms is also introduced. Chapter 3 presents a detailed explanation of the phase unwrapping algorithm based on rotational compensator that is the main step for the first proposed phase unwrapping algorithm which is explained in details in chapter 4. In addition, the applicability of the first proposed algorithm is demonstrated by using simulated and real wrapped phase data is also given chapter 4. Furthermore, this chapter shows a comparison between the proposed algorithm and the existing phase unwrapping algorithms to examine the quality of the unwrapped results for actual phase data. Meanwhile, chapter 5 presents the idea and details description of the second proposed algorithm for phase unwrapping. Beside that chapter 5 shows the unwrapped simulated and experimental results for this proposed algorithm to demonstrate the performance of the proposed algorithm for noisy phase images. Finally, the work accomplished is concluded in chapter 6 with comments regarding the significance of the work accomplished.

CHAPTER **2**

BACKGROUND OF PHASE EXTRACTION AND UNWRAPPING PROCESSES

- Introduction
- Phase extraction and calculation
- Phase unwrapping
- Existing phase unwrapping algorithms
- Conclusions

Chapter 2
Background of phase extraction and unwrapping processes

2.1 Introduction

Many techniques allow the measurement of physical properties based on the retrieval of phase information encoded in an interference pattern. Techniques such as profilometric [32, 33] and interferometric [34, 35] methods measure mechanical properties (e.g., strain or deformation) of materials. These techniques encode the information about physical quantities as phase data found in the measured intensity of a two-dimensional fringe pattern. Therefore, the accuracy of measurements carried out by these optical techniques is strongly dependent on the accuracy of fringe analysis techniques that use to retrieve the phase distribution of the recorded fringe patterns. In general, the true phase may range over a larger interval than 2π, which implies that the obtained phase may contain discontinuities. For many years Fourier transform fringe analysis technique [36] has been regarded as being fast and reliable technique for the analysis of fringe patterns. This technique extracts the phase of a fringe pattern by using Fourier transform and carrying out filtering in the frequence domain. The phase produced by the first stage is wrapped contains 2π jumps, which should be removed by using phase unwrapping algorithm.

In this chapter, the processes of phase extraction and unwrapping will be defined and explained in detail. The methods and techniques that use to extract and calculate the phase from a fringe pattern are introduced; since this step, phase extraction, is strongly affected the accuracy of results obtained by the unwrapping process. In essence, this chapter will explain the important terminologies such as singular point (SP) and singularity in phase unwrapping specifying how to locate SPs in the phase map. SPs are local inconsistencies that prevent straight-forward unwrapping. Furthermore, the branch cut technique used to avoid the SP ef-

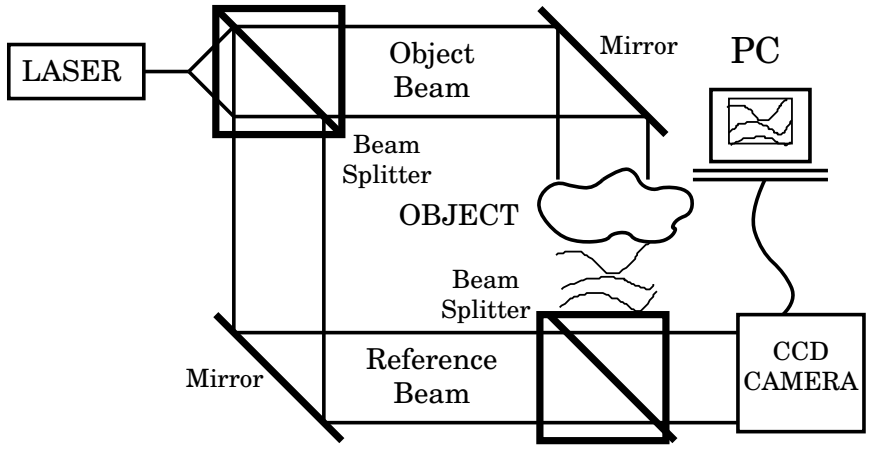

Figure 2.1: *A schematic diagram of an experimental setup system of the interferometer technique measurement.*

fect will be presented. In addition, existing two-dimensional phase unwrapping methods will be presented. This chapter will help in understanding the material presented in later chapters.

2.2 Phase extraction and calculation

Here, we present two famous examples of applications that are based on phase measurements to obtain their desired results. The two examples are interferometric measurements and Fourier transform profilometry measurements. In each example, we start by introducing the principle of system setup for measuring and how the phase is extracted from the measured data.

2.2.1 Phase extraction for interferometric measurements

Interferometer is a technique of measuring the phase modulation from the light reflected or transmitted from a projected object to screen in the form of interference pattern. The optical setup of interferometric system is shown in Fig 2.1. For the measuring, light from a laser is divided by a beam splitter into two beams, one for object illumination and another for a reference. The object beam illuminates the object, the illuminating light is transmitted through

the object toward the detector, where it forms an image of the object on a CCD camera. An interferogram is a fringe pattern formed on the CCD as a result of the interference between the reference beam, R, and the object beam, O. The intensity recorded on the CCD is given by

$$I(x,y) = |R|^2 + |O|^2 + R^*O + RO^*, \tag{2.1}$$

where R^* and O^* denote the complex conjugates of R and O, respectively.

The last two terms of Eq. (2.1) contain information about the amplitude and the phase of the object. To retrieve the phase information, two techniques are partly used. One is the phase shift interferometry [6, 8, 9], in which several fringe patterns are recorded by varying the known phase shift introduced to one of the beams in the interferometer system. The other one is spatial filtering for interferogram using the Fourier transform method [5–7]. The Fourier transform method requires only one fringe pattern; however, high frequency part of spectrum in Fourier domain cannot be used. A schematic diagram describing the use of the Fourier transform method is shown in Fig. 2.2. In the figure, the Fourier spectrum, $\widehat{I}(k_x, k_y)$, shows a symmetrical distribution of the origin. The $\widehat{I}_F(k_x, k_y)$ is the filtered spectrum in which the zero-frequency component and one of the symmetrical distributions are eliminated. The center of gravity of the filtered spectrum can be also obtained. There is a problem in the filtering of the spectrum that we normally cannot determine which non-zero spectrum should be eliminated. However, even when the eliminated term is incorrect, the sign of the phase modulation is only inverted. Therefore, if we know the sign of the phase modulation, we can determine it after the phase unwrapping. After filtering and inverse Fourier transformation the complex amplitude of the wave front is obtained. From the complex digitalized amplitude, the phase of the wave front is calculated by the relation

$$\Psi(x,y) = \arctan \frac{\mathrm{Im}[O(x,y)]}{\mathrm{Re}[O(x,y)]}, \tag{2.2}$$

where Im and Re denote the real and the imaginary parts, respectively. $\Psi(x,y)$ denotes the estimated phase obtained from the evaluation of the interferogram, and it is a wrapped phase ranged in the interval from $-\pi$ to π.

However, a major problem with interferometric techniques that recover phase information

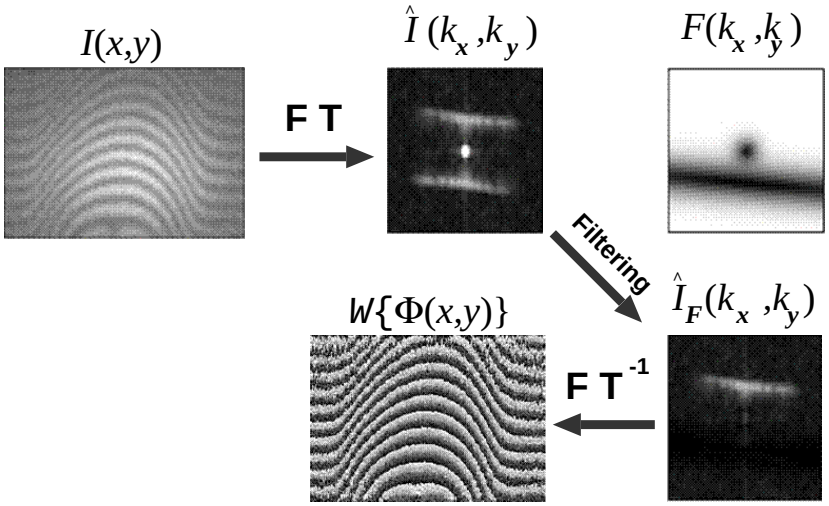

Figure 2.2: *Procedure for calculating the phase from an interferogram: FT Fourier transformation, FT^{-1} inverse Fourier transformation, the $I(x, y)$ is a fringe pattern for interferometric data, the $\widehat{I}(k_x, k_y)$ shows Fourier spectrum of the fringe pattern, the $F(k_x, k_y)$ shows the filtering function, the $\widehat{I}_F(k_x, k_y)$ shows the filtered spectrum, the $W\{\Phi(x, y)\}$ is the wrapped phase modulation.*

is that the reconstructed phase is mathematically limited to the interval $(-\pi, \pi]$. Therefore, unwrapping process is needed to apply for retrieving the continuous phase form.

2.2.2 Phase extraction for Fourier transform profilometry measurements

Noncontact measurement methods are employed to determine the three-dimensional height distribution of an object. Several three-dimensional object profilometry methods are concerned with extracting the geometry information from the image of the measured object, such as Moiré topography [37], phase measurement profilometry [38], Fourier transform profilometry (FTP) [39], and many other methods. These methods all vary in accuracy, the number of frames required, and the processing time. FTP is considered as one of the most popular among them. The FTP method is usually implemented as follows: Initially, a Ronchi grating or a sinusoidal grating is projected onto the object's surface. Then, a sequence of dynamic projected zebra-patterned images can be captured by a CCD camera from the other view point. The projected fringe patterns are deformed or phase modulated by the height distribution of the object. Then, the deformed fringe pattern images are analyzed or demodulated using a

fringe analysis algorithm to extract the phase distribution of the fringe patterns. Finally, the height distribution of the object can be evaluated from the demodulated phase.

The optical geometry of the measurement system for an object by using the traditional FTP is as shown in Fig. 2.3(a), in which the optical axes of a projector and a camera lie on the same plane on $y = 0$. The camera is focused to the reference plane, where the reference plane is a virtual plane that serves as a reference from which the object height is measured. The reference plane is located at $z = 0$. The projector illuminates the sinusoidal pattern to an object, as illustrated in Fig. 2.3(b). The direction of the illuminated light is oblique to the reference plane. The angle between the camera direction and the illuminated light direction is θ (where $tan(\theta) = d_0/l_0$). When a sinusoidal optical field is projected onto a three-dimensional object, the images of a projected fringe pattern and an object with projected fringes can be represented by the following equations:

$$g_0(x, y) = a(x, y) + b(x, y) \cos[2\pi f_0 x + \phi_0(x, y)], \tag{2.3}$$

$$g(x, y) = a(x, y) + b(x, y) \cos[2\pi f_0 x + \phi(x, y)], \tag{2.4}$$

where $g_0(x, y)$ and $g(x, y)$ are the intensity of the images at the (x, y) point, $a(x, y)$ represents the background illumination, $b(x, y)$ denotes amplitude modulation of the fringes, $b(x, y)/a(x, y)$ is the fringe contrast, f_0 is the spatial-carrier frequency, and $\phi_0(x, y)$ and $\phi(x, y)$ are the phases of the background zebra pattern and the distorted fringe pattern observed from the camera, respectively. The phase function $\phi(x, y)$ contains the required information about the shape measurement of the object, which can be represented as

$$\phi(x, y) = \phi_0(x, y) + \Delta\phi(x, y), \tag{2.5}$$

where $\phi_0(x, y)$ is the phase caused by the angle of projection corresponding to the reference plane, and $\Delta\phi(x, y)$ is the phase caused by the object's height distribution, where

$$\Delta\phi(x, y) = 2\pi f_0 \Delta x. \tag{2.6}$$

The task now is to find the relationship between the extracted phase and the height distribution using the geometric system. As shown in Fig. 2.3(b), the fringe projected from the projector reaches the object at point B and will cross the reference plane at point A. The relationship

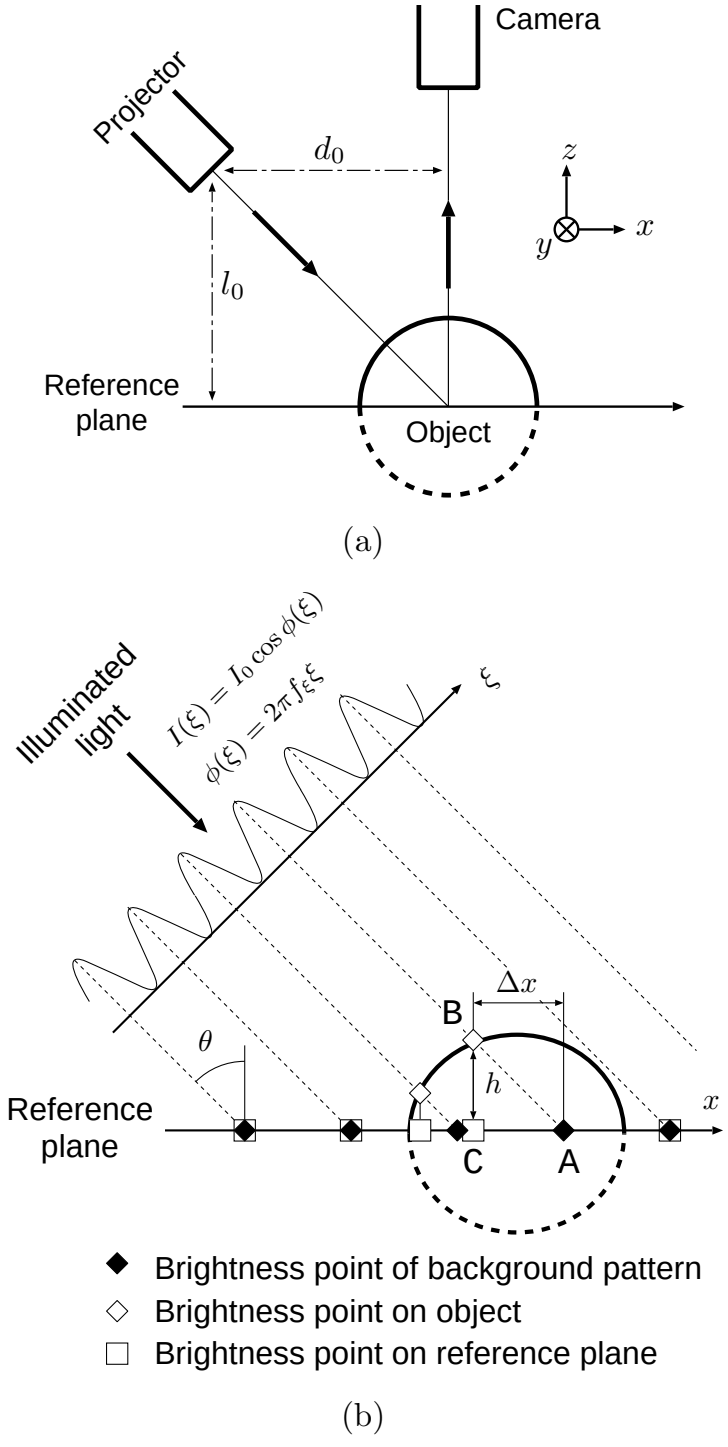

Figure 2.3: *Experimental setup of three-dimensional shape measurement system. (a) geometry for the projecting and imaging grating pattern on the object, (b) sketch map for projected light pattern.*

between the height to be measured, $h(x, y)$, and the shift distance, Δx, by the object on the reference plane is

$$\begin{aligned} h(x, y) &= \frac{\Delta x}{\tan(\theta)} \\ &= \Delta x \frac{l_0}{d_0}, \end{aligned} \tag{2.7}$$

where l_0 and d_0 are distances, as shown in Fig. 2.3(a). From eqs. (2.6) and (2.7), the height distribution of the object can be presented by the phase shift, $\Delta\phi(x, y)$, as follows:

$$h(x, y) = \frac{\Delta\phi(x, y) l_0}{2\pi f_0 d_0}. \tag{2.8}$$

Unfortunately, most fringe analysis techniques produce a so-called "wrapped phase" instead of the required continuous phase. Consequently, phase unwrapping algorithms are required to recover the true phase from the wrapped phase.

2.3 Phase unwrapping

Phase unwrapping has been a research area for more than two decades. Hundreds of papers have been published aimed at solving the phase unwrapping problem. Many phase unwrapping algorithms have been suggested and implemented. The reason for such interest in phase unwrapping is due to many applications in applied optics that require an unwrapping process. Many phase unwrapping algorithms has been developed only for data from a particular application. There is no universal phase unwrapping algorithm that can solve wrapped phase data from any application. Moreover, phase unwrapping algorithms are generally a trade off between accuracy of solution and computational requirements. Even so, the most robust phase unwrapping algorithm cannot guarantee in giving successful or acceptable unwrapped results without a good set of weights.

2.3.1 Phase unwrapping definition

Commonly, most of phase unwrapping algorithms are based on one assumption that the true unwrapped phase data varies slowly enough that neighboring phase differences values are

within one half cycle (π radian) of each other. If this assumption is true everywhere the unwrapping process can be applied simply by integrating wrapped phase differences, or gradients, along any path from pixel to pixel throughout the phase data to obtain unwrapped phase. In one-dimensional phase unwrapping, this process is repeated from first end point region (first pixel) toward the second end point region (last pixel); hence, the phase difference can be calculated as follows:

$$\triangle\Psi^i = \Psi_i - \Psi_{i-1} \tag{2.9}$$

where Ψ_i is the wrapped phase at pixel i in phase map. When the phase difference, $\triangle\Psi^i$ is larger than a half cycle the wrapped phase is shifted one cycle, so the shifted difference is again smaller than a half cycle. This shift operation is same as the wrapping operation used to obtain the principal value of the true phase. The wrapping operator is defined as follows:

$$\Psi_i = W[\Phi_i] \cong \Phi_i - \mathrm{Int}\left[\frac{\Phi_i}{2\pi}\right] 2\pi \tag{2.10}$$

where $-\pi < W[\Phi_i] \leq +\pi$, Φ_i is the continuous true phase at pixel i in phase map and Int[.] means a function that returns the nearest integer. The wrapping operator $W[.]$ could be modified to specify the corrected gradient phase difference, $\hat{\nabla}\Psi^i$ between two successive pixels in the unwrapping path as:

$$\hat{\nabla}\Psi^i = W[\Psi_i - \Psi_{i-1}] \tag{2.11}$$

In two-dimensional phase unwrapping, there are paths with loop; it means that the last point can be considered as the first point. In the absence of discontinuity sources, the unwrapped result is independent on the unwrapping path; therefore, the unwrapped phase map is consistent. Consider that the path of loop consists of M points, using Eqs. (2.9)-(2.11) we can retrieve the true unwrapped phase as follows:

$$\Phi_M = \Phi_0 + \sum_{i=1}^{M} \hat{\nabla}\Psi^i \tag{2.12}$$

Thus, by using Eq. (2.12) phase unwrapping will be capable to retrieve the contiguous form of the phase map. However, in the presence of discontinuities, the path of integration becomes dependent and just taking any path is not possible anymore. If Eq. (2.12) is used by itself

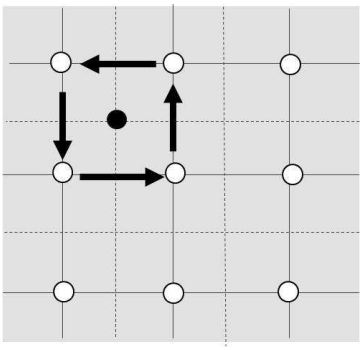

Figure 2.4: *Elementary path in two-dimensional coordinate for visualizing SP identification: the white circles denote points at which the phase values are defined, the thick arrows denote the direction of the path around the tested SP, the black circle illustrates the position of the tested SP.*

to retrieve the unwrapped phase map, it may result in the addition or subtraction of incorrect multiples of 2π which will then propagate throughout the rest of the phase map. Restrictions must be used on the unwrapping path in the corrupted areas, which result in the path being path-dependent. To avoid this situation, corrupted areas, which are singular points (SPs), must be identified, balanced and isolated using barriers (branch cuts) from the rest of the good pixels in the phase map. Once SPs are isolated, phase unwrapping will take an independent path avoiding these branch cuts, thus, retrieving the true phase.

2.3.2 Singular points and branch cuts

A path in the two-dimensional phase map consists of a sequence of horizontal and vertical segments joining adjacent points. To find SPs, consider a closed path starting in every point defined by the corners of a 2×2 square, as shown in Fig. 2.4. In the figure, the circles denote points at which the wrapped phases are defined. The thick arrows show the direction of the considered elementary path that surround the tested SP. The filled circle denotes the position of the tested SP, for simplicity every SP is defined at the center of the loop. The SPs are marked the start and end of 2π discontinuity line. They are identified by summing the wrapped phase gradient, $\hat{\nabla}\Psi^i$, as follows:

$$\sum_{i=1}^{N} \hat{\nabla}\Psi^i = 2\pi S \tag{2.13}$$

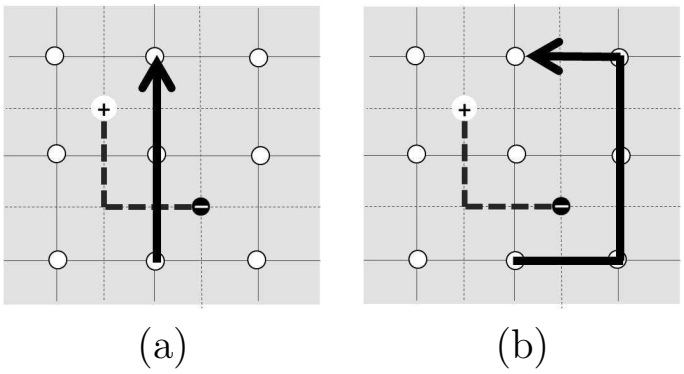

Figure 2.5: *Unwrapping path with the existence of the branch cuts in the phase map: the thick dashed line denotes the branch cut that connects two of opposite sign SPs, the thick arrow shows the direction of unwrapping path; (a) incorrect unwrapping path, (b) correct unwrapping path.*

where S is the SP residue. The SP is called a positive residue when S in Eq. (2.13) is $+1$; otherwise, it is called a negative residue when S is -1. While, $S = 0$ indicates that no residue exists. In the case of SP is presented, the result of Eq. (2.13) is always a $+1$ or -1 because the 2×2 closed path cannot encircle more than one residue[40].

When a closed path includes same number of SPs with positive residues and that ones with negative residues the integral of phase gradient along the chosen path is equal to zero, thus, the unwrapping process is carried out successfully. This can be achieved by placing lines between SPs with opposite signed residues, which are called branch cuts. These branch cuts act as barriers to prevent the unwrapping path to cross them [12–14, 16–18], as shown in Fig. 2.5 which illustrates the principle of unwrapping around the branch cuts. In Fig. 2.5(a) the unwrapping path is going thorough the branch cut which has been placed to connects two SPs in the wrapped phase map. Therefore, errors will propagate and create 2π discontinuities in the unwrapping phase map. On the other hand, Fig. 2.5(b) shows the correct unwrapping path that avoids the branch cut, consequently, error propagation in the unwrapping solution is avoided.

Many different kinds of SPs exist in the wrapped phase map caused by phase noise, spatial under-sampling of phase, object discontinuity, etc. SPs can have one of two forms, of which dipole SPs or monopole SPs. Dipole SPs are those SPs that exist in pairs of two opposite residues; meanwhile, monopole is a single SP in which no corresponding opposite residue

partner is existed in the wrapped phase map [17]. One specific type of dipole SPs is called phase noise generated dipole SPs. This is caused by the random fluctuation of phase due to noise, which results in the wrapped phase gradient exceeding $|\hat{\nabla}\Psi| > \pi$. Each pair of SPs for this dipole type is often found close to each other (generally one pixel apart). This dipole type can be easily identified and isolated in the phase map. An example of phase noise dipole SPs is shown in Figs. 2.6(a) and (b). The second type of SP dipoles are dipoles that result from under-sampling of the phase distribution. These dipoles are generated by the violation of sampling theorem where the phase is not represented with sufficient spatial resolution to correctly represent the contiguous phase. This results in spatial under-sampling steps greater than $+\pi/-\pi$. This type of SPs dipole is characterized by that these SPs tend to be well separated when sampling theorem is broken, at which makes them hard to identify as shown in Fig. 2.6(c).

Another kind of SP dipoles are dipoles caused by object discontinuity. Sometimes wrapped phase maps contain objects that are discontinuous by nature, such as holes, sharp edges, cracks or fluids of varying refractive index [13, 41]. These discontinuous objects often generate SP dipoles that are found on the discontinuity edges. The existence of these SP dipoles depends on the discontinuity size of the object. If the object discontinuity exceeds π when wrapped, this case will cause SPs. This object discontinuity SPs dipole is characterized by that its SPs tend to be well separated depending on the nature of the discontinuity, which makes them hard to identify as presented in Fig. 2.6(c).

Basically, SPs appear as pairs of poles of opposite sign. However, some isolated SPs or SPs of dipoles with long distances, which are called monopoles, may appear near the boundaries of the phase map because the measurement domain is finite, as shown in Figs. 2.6(d) and (e). This can lead to that the number of positive SPs and negative ones in the measurement area are different. Moreover, monopoles spread error throughout the entire measurement area [46]. Therefore, it is needed to balance the number of positive and negative SPs. One solution is to append virtual SPs (VSPs) outside the measurement area. Thus, branch cuts will link positive and negative sources with each other forming dipole pairs, and then the error of monopoles will be reduced. However, there are several positive and negative SPs in the phase map, hence, there will be numerous possible branch cuts between them. For any possible set of branch cuts,

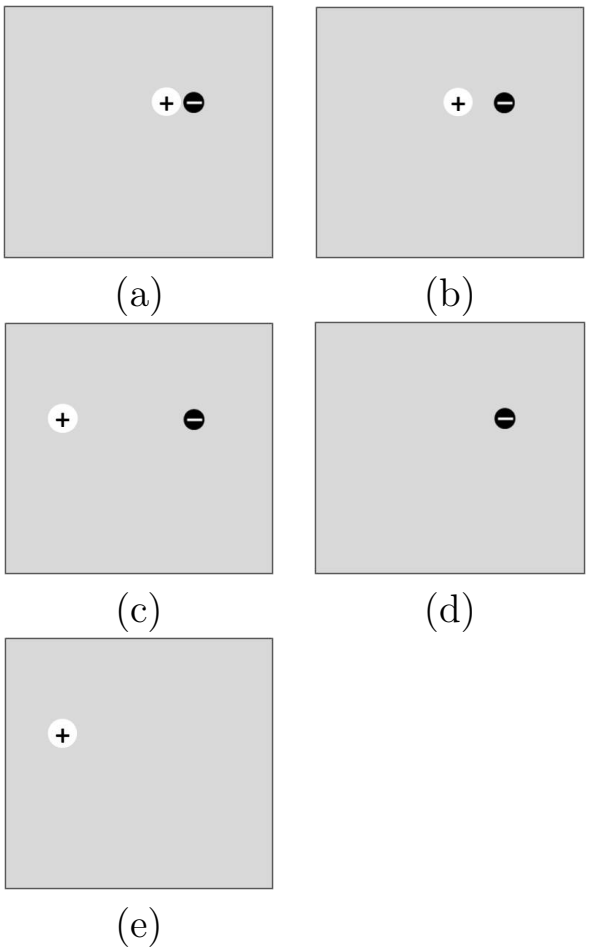

Figure 2.6: *Schematic figure shows SPs types: (a) one pixel apart dipole SPs generated by phase noise, (b) dipole SPs generated by phase noise several pixels apart, (c) dipole SPs generated by discontinuous objects and under-sampling have the tendency of lying far apart from each other and (d) & (e) are monopole SPs.*

the unwrapped phase map is not the same, in spite of this only one unwrapped phase map is correct. To find the correct set of branch cuts, a criterion has to be set as an evaluation for the quality of the unwrapped result. For example, Gutmann and Weber [17] used the distance distribution of SPs inside the whole measurement area to determine branch cuts set.

2.4 Existing phase unwrapping algorithms

In order to solve inconsistencies caused by SPs, many phase unwrapping algorithms have been proposed in the past. When we focus on the methods that handle the SPs directly, the phase

unwrapping algorithms are classified into two types according to the nature of the unwrapped results, which are path following phase unwrapping methods and least squares based methods. These phase unwrapping methods are presented in the following subsections. However, there is another classification for the existing unwrapping methods that includes the methods which do not handle the SPs such as denoising methods, we give a brief explanation about these methods through section 1.2 in chapter 1.

2.4.1 Path following methods

A simple local phase unwrapping methods use independent path integration between the starting point and the end point to retrieve the true unwrapped phase in the absence of SPs in the wrapped phase map. They are a pixel-to-pixel integration techniques rely on local wrapped phase values along a chosen path to construct the correct true phase refereed to as unwrapped phase. Thus, by using Eq. (2.12), these methods are capable of retrieving the contiguous form of the phase map. However, this is not always the case, due to that the presence of noise or corrupted areas in the wrapped phase map makes the integration path becomes dependent. When Eq. (2.12) is used by itself to retrieve the unwrapped phase map, it may result in adding or subtracting of incorrect multiples of 2π, which will then propagate throughout the rest of the phase map. Therefore, restrictions must be used on the unwrapping path in the corrupted areas, which result in the path being dependent. To avoid this situation, corrupted areas which are SPs must be identified, balanced and isolated using branch cuts from the rest of the good pixels in the phase map. Once SPs are isolated, phase unwrapping will take an independent path avoiding these branch cuts, thus, retrieving the correct phase data.

Goldstein et al. method

The tree branch cut placement method, which is called Goldstein et al., is one of the earliest branch cut methods [11]. This method creates trees that connect a number of nearest neighbor SPs where the net charge of every tree should be zero. Therefore, when this method produces a tree which is not neutral and is closer to the border than any neutralizing SP, this tree is neutralized by connecting it to the nearest border pixel. This method is very fast but it tends to

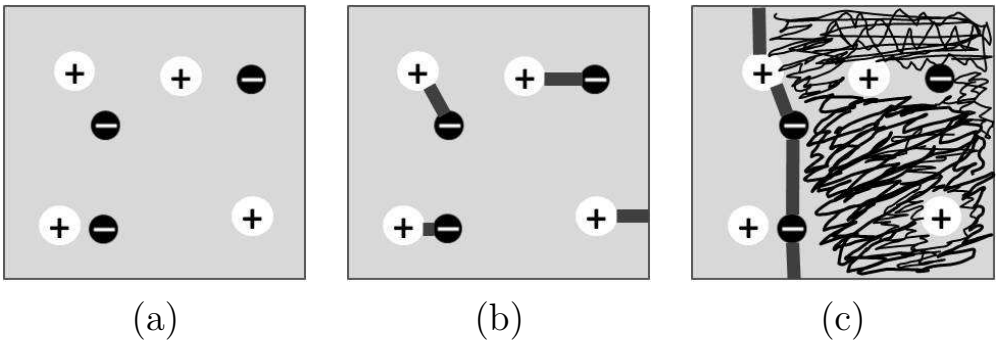

Figure 2.7: *Spreading of errors in regular regions due to the Goldstein method handling way for the singularity regions in the phase map: (a) SPs distribution map, (b) correct placement of branch cuts, (c) incorrect placement of branch cut lines and phase errors appear in regular regions.*

isolate areas with dense SPs because branch cuts in such areas often close on themselves. The weakness of this method is the lack of a weighting factor. Furthermore, the choosing wrong of a single branch cut causes errors propagate over the whole image. To explain that consider Fig. 2.7, this figure presents an example of SPs distribution map, shown in Fig. 2.7(a), and the handling way of Goldstein method for these singularity regions in the phase map. When Goldstein method successfully can place the correct branch cut set between SPs, as shown in Fig. 2.7(b); the obtained unwrapped phase result does not have any phase error and these results are perfect results. This case happen when the S/N ratio is high, thus the number of SPs is small. However, it is impossible to set the branch cuts correctly between SPs in the case of low S/N ratio due to the existence of many SPs, as shown in Fig. 2.7(c); making the placement process of branch cuts more complicated. Therefore, the unwrapping process can not carry out correctly, and a lot of phase errors and jumps are found, as shown in Fig. 2.7(c).

Noise-immune phase unwrapping method

The dipole branch cut method [12] uses the nearest neighbor heuristic search to find the nearest opposite polarity residue for every SP in the phase map. It connects the nearest possible SPs pair with opposite SPs polarity by a single branch cut, and does the same procedure to the rest of the SPs until there is no SP not connected by branch cut. In the case of a SP having the border closer than any balancing SP, the SP is connected by branch cut with the nearest border pixel, and this border as virtual SP. One disadvantage of this branch cut method

is that it often ends up with very long branch cuts. Many methods were proposed by using more sophisticated search strategies, such as improved nearest neighbor, simulated annealing, minimum-cost matching, stable marriages and reverse simulated annealing, to find the corresponding dipoles with the minimum total connection length [13, 14, 17]. An advantage of these dipole methods over the tree method is that they are less likely to create branch cuts that isolate noisy regions in the phase map. The major disadvantage of the tree and the dipole branch cut methods is that they use straight line branch cuts which leads to unrealistic discontinuities distorting the unwrapped phase map even though they attempt to balance the overall SP reside in the unwrapped phase map; the example of that situation is given in Fig. 2.7.

Flynn's minimum weighted discontinuity method

Flynn method [15] suggests that the discontinuities in the unwrapped phase, which are SPs, must be restricted to areas of noise and true discontinuity in the profile. These discontinuity areas can often be identified by their low quality. This method works with or without quality map to find the unwrapped phase surface that is matching to the wrapped phases and whose discontinuities are minimal in some sense. The elementary operation of this algorithm is to partition the phase image into two connected regions, then raise the unwrapped phase by 2π in one of the regions and reduce the minimal weighted sum of discontinuities. This is done repeatedly until no suitable partitions exist. The operations are found by creating paths that follow discontinuity curves and extending them to form complete partitions. The algorithm terminates these iteration processes when no path can be extended. The major disadvantage of Flynn method is that it required too high computational time cost since it use iteration process during found its unwrapped results by minimize the weighted sum of discontinuity magnitudes. Furthermore, if too many of the weights are high, this method may make poor SP pairing due to low weight paths connecting the SPs are not available. This is similar case as Goldstein method when it tries to place branch cuts for wrapped phase data has high number of SPs; therefore possibility of correct placement is poor and a lot of phase errors will appear in its unwrapped results, as illustrated in Fig. 2.7.

2.4.2 Least squares based methods

Least squares based methods are completely different than path following methods. These methods in general minimize up to a certain degree the difference between the gradients of the wrapped and the gradient of the unwrapped solution in both x and y direction. This problem is considered to be described by a solution of the partial differential equation (PDE) [24] by appending symmetrical images outside the original image, and taking the Neumann condition as a boundary condition [23, 24, 42]. Then Fourier transform (FT) or discrete cosine transform (DCT) is applied to facilitate faster computation [23, 25]. However, these methods do still indirectly deal with the SP problem because their solution is obtained by integrating over the SPs to minimize the gradient differences [10]. The unwrapped phase maps do not contain any continuous phase gaps, which had commonly appeared in the path following methods. The path dependency, which is considered as error or consequence of the inconsistencies, is spread throughout the whole domain in order to avoid any large localized errors [10, 16]. The distributed error in the unwrapped result is considered acceptable if it is smaller than the noise level of the wrapped noisy data in the measurement. However, the magnitude of error depends on distribution of the SPs that appear around inconsistent phase jumping segments. These methods that using least squares technique have the advantage that they are more noise tolerant and they achieve the global smoothness of the unwrapped solution.

Unweighted least squares method

The unweighted least squares method [25] minimizes the difference between the phase gradient estimate (unwrapped phase) and the true gradient in the least square sense,

$$\varepsilon^2 = \sum_{i=0}^{M-2}\sum_{j=0}^{N-1}\left|\Phi_{i+1,j} - \Phi_{i,j} - \hat{\nabla}\Psi^x_{i,j}\right|^2 + \sum_{i=0}^{M-1}\sum_{j=0}^{N-2}\left|\Phi_{i,j+1} - \Phi_{i,j} - \hat{\nabla}\Psi^y_{i,j}\right|^2 \quad (2.14)$$

Therefore, the solution that minimizes the difference shown in Eq. (2.14) is the unweighted least squares solution. This equation can be modified to the form presented as follows:

$$\Phi_{i+1,j} + \Phi_{i-1,j} + \Phi_{i,j+1} + \Phi_{i,j-1} - 4\Phi_{i,j} = \hat{\nabla}\Psi^x_{i,j} - \hat{\nabla}\Psi^x_{i-1,j} + \hat{\nabla}\Psi^y_{i,j} - \hat{\nabla}\Psi^y_{i,j-1} \quad (2.15)$$

Equation (2.15) can be further modified [10] to the following partial differential equations in a form as illustrates:

$$(\Phi_{i+1,j} - 2\Phi_{i,j} + \Phi_{i-1,j}) + (\Phi_{i,j+1} - 2\Phi_{i,j} + \Phi_{i,j-1}) = \rho_{i,j} \tag{2.16}$$

where $\rho_{i,j} = (\hat{\nabla}\Psi^x_{i,j} - \hat{\nabla}\Psi^x_{i-1,j}) + (\hat{\nabla}\Psi^y_{i,j} - \hat{\nabla}\Psi^y_{i,j-1})$.
Equation (2.16) is a discretization of Poisson's equation on a rectangular grid as

$$\frac{\partial^2}{\partial x^2}\Phi(x,y) + \frac{\partial^2}{\partial y^2}\Phi(x,y) = \rho(x,y) \tag{2.17}$$

Equation (2.16) can be transformed into matrix vector form to transform the problem into a linear system as

$$\mathbf{Q}\mathbf{\Phi} = \rho \tag{2.18}$$

where $\mathbf{Q}$ is a matrix that performs the discrete Laplacian operation on the vector $\mathbf{\Phi}$ shown on the left hand side of Eq. (2.16), Φ is a column vector containing the unwrapped phase values which is the solution and ρ a column vector containing the discrete Laplacian operation on the wrapped phase differences as shown in Eq. (2.16).

The unweighted least squares method is well defined mathematically. However, this method generates a very large number of linear equations to be solved equivalent to the total number of pixels in the phase map. There are many methods developed to solve the linear system in Eq. (2.18). In essence, such methods are directly based on the fast Fourier transform (FFT) or DCT or the unweighted multi-grid algorithm by Ghigilia [25].

Weighted least squares method

The weighted least squares method requires weights to achieve better results than the unweighted counterpart. These weights are user defined weights generated from quality-maps used to isolate corrupted areas with SPs by masking them out of the wrapped phase data to diminish their effect on the unwrapped solution. The weighted least-squares method is a modification of the unweighted one where Eq. (2.14) is modified to the equation presented in Eq. (2.19) [25]:

$$\varepsilon^2 = \sum_{i=0}^{M-2}\sum_{j=0}^{N-1} w^x_{i,j}\left|\Phi_{i+1,j} - \Phi_{i,j} - \hat{\nabla}\Psi^x_{i,j}\right|^2 + \sum_{i=0}^{M-1}\sum_{j=0}^{N-2} w^y_{i,j}\left|\Phi_{i,j+1} - \Phi_{i,j} - \hat{\nabla}\Psi^y_{i,j}\right|^2 \tag{2.19}$$

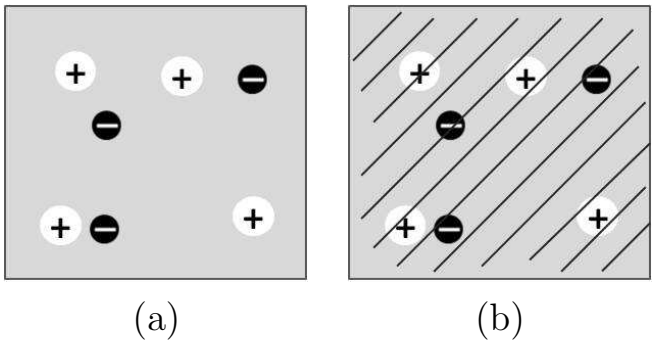

Figure 2.8: *Spreading of errors in regular regions due to the LS-DCT method handling way for the singularity regions in the phase map: (a) SPs distribution map, (b) phase errors appear in regular regions.*

where weights are defined as following:

$$w^x_{i,j} = \min(w^2_{i+1,j}, w^2_{i,j}), w^y_{i,j} = \min(w^2_{i,j+1}, w^2_{i,j}) \tag{2.20}$$

where $0 \leq w^x_{i,j}, w^y_{i,j} \leq 1$. The weights are squared because of the matrix operation $(W^T W)$ of the weighted least squares method. A drawback with these methods is the case that if some SPs are not masked out, they will cause the unwrapped phase to be severely corrupted depending on the density of these unmasked SPs. The most famous name is mentioned to least squares method is least-square method by using discrete cosine transform (LS-DCT). The natural of LS-DCT method is to spread the singularity of SPs to the whole domain of the measured phase data including regular regions that have no SPs. It means that phase errors occurred due to SPs are also propagated to regular region. Therefore the unwrapped results obtained by LS-DCT method has phase errors with unique density; an example of this case is given in Fig. 2.8. In the figure, SPs distribution map is shown in Fig. 2.8(a); the distribution of the phase errors appears in the measured domain due to the handling way of LS-DCT method for singularity regions of this example is presented in Fig. 2.8(b). These phase errors are different from those error produce due to handling way of Goldstein for the same singularity regions, as illustrated in Fig. 2.7(c).

Singularity spreading phase unwrapping algorithm

Singularity spreading phase unwrapping method (SSPU) [43] is classified into methods that is based on least squares approach. The basic idea of this algorithm depends on the characteristic

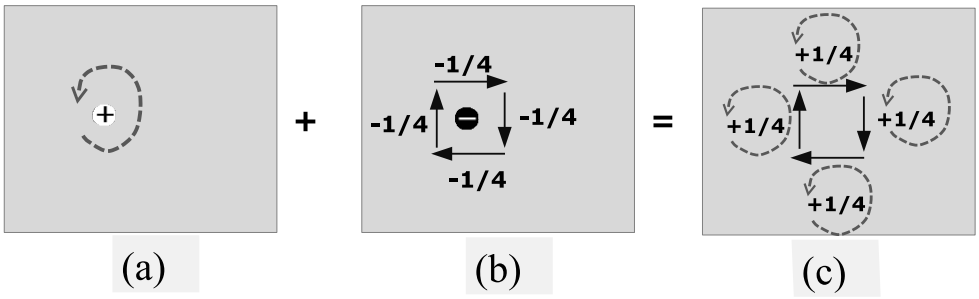

Figure 2.9: *Schematic of the singularity spreading phase unwrapping: (a) singular point, (b) compensator, (c) spread singularity.*

properties of the distribution of SPs. When a SP in a phase map is found, the amplitude at this point and in its vicinity is almost zero. This phenomenon is consistent with the fact that the amplitude should be zero when the phase is indeterminate. Furthermore, most of the SPs are found to be local $\pm 2\pi$ pairs. The phase data around these SPs is distorted and has incorrect value because the amplitude and phase in the SP vicinities are continuously affected by the interference of propagated electromagnetic wave. Therefore, the SPs should be compensated in a continuous manner with its vicinity instead of discrete 2π phase shift. In SSPU algorithm, compensators are not added only to the pixel values at the SPs but also those at around the SPs [43]. Continuous-valued compensators diffuse and spread the singularity in the phase image. The final distribution of the compensators is determined by the SP distribution.

Based on the aforementioned basic idea, Fig. 2.9 shows a schematic diagram of the SSPU algorithm. Figure 2.9 (a) shows the accumulation of wrapped phase difference, $R(x, y)$ at position (x, y) in the wrapped phase image which is defined as follows:

$$R(x,y) \equiv \frac{1}{2\pi}\{W[\Psi(x+1,y)-\Psi(x,y)] + W[\Psi(x+1,y+1)-\Psi(x+1,y)] \\ -W[\Psi(x+1,y+1)-\Psi(x,y+1)] - W[\Psi(x,y+1)-\Psi(x,y)]\} \quad (2.21)$$

where $\Psi(x, y)$ denotes observed wrapped phase value, and $W[.]$ means the principal value within $(-\pi, \pi]$. At an SP, $R(x, y) \neq 0$. Then, spread around and attenuate the phase inconsistency by adding fractions of inverse rotation to respective four phase derivatives around the SP as shown in Fig. 2.9(b) and (c). Repeat the same treatment over the whole image. After L times iterations of this process over the image, it can be obtained accumulative compensators in x and y directions. Then, the phase data can be unwrapped simply by summing the phase

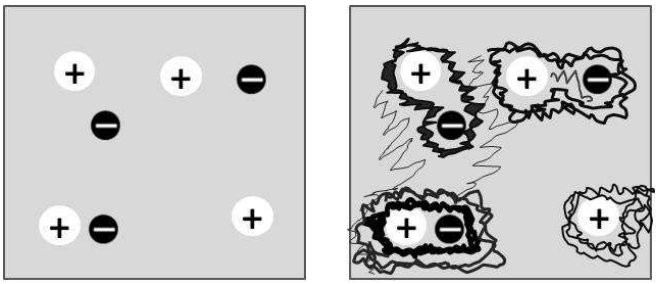

(a) (b)

Figure 2.10: *Spreading of errors in regular regions due to the SSPU method handling way for the singularity regions in the phase map: (a) SPs distribution map, (b) phase errors appear in regular regions.*

differences between the neighboring pixels. SSPU algorithm has an advantage to obtain continuous phase unwrapping; however, it has drawbacks. Firstly, actual phase gap such as a cliff in geographical map is also spread. In addition, it requires large computational time to obtain a suitable result. When the maximum residue value after the spreading process is not negligible value, means not very small, it is needed to repeat many times of processes. Figure 2.10 gives an example of SPs distribution map and the handling way of SSPU method to regulized the singularity regions in the measured domain and also illustrates the phase errors appears as a result of this handling way. SSPU method has the same properties of LS-DCT method for spreading SPs' singularities. However, the phase errors produced due to these singularities spreading for SSPU method are different in the spreading way and amplitude than LS-DCT method does, as illustrated in Fig. 2.8(b). Meanwhile, phase errors appear from singularity spreading of SSPU method are decrease at the regions that are far from SPs positions, as shown in Fig. 2.10(b).

2.5 Conclusions

This chapter has presented a background about the phase extraction and unwrapping processes. Regards phase extraction process, famous techniques used for this purpose are given and illustrated. A definition of the phase unwrapping process is also presented, with a review of some of the existing phase unwrapping algorithms. The problems that face many phase unwrapping algorithms have been briefly described. The major problem for all phase

unwrapping algorithms is the SPs problem and their effects on the unwrapping process.

In summary, it is obvious that phase unwrapping has faced great challenges especially when the data contains discontinuous and contiguous features at the same time. There is clearly a need for further investigation with particular emphasis to solve this problem even though less complex featured data rely extensively on weights to produce acceptable results. In essence, the following chapters are designed to address these issues, with the ultimate goal of improving the generality and accuracy methods.

CHAPTER 3

PHASE UNWRAPPING ALGORITHM BY USING ROTATIONAL COMPENSATOR

- Introduction
- Rotational compensator phase unwrapping method
- Results and discussion
- Conclusions

Chapter 3
Phase unwrapping algorithm by using rotational compensator

3.1 Introduction

The process of phase unwrapping for an image obtained by interferometer, which is noisy image data, may face difficulties. Traditional phase unwrapping algorithms used to estimate two-dimensional phase distribution include much estimation error due to effect of SPs. This chapter introduces an accurate phase unwrapping algorithm based on three techniques. The developed algorithm computes the compensator values through superposing the effect of each SP by adding an integral of isotropic singular function along any loops. The unwrapped phase result demonstrates that the accuracy is improved by using this developed algorithm compared with past methods based on the least squares approach.

3.2 Rotational compensator phase unwrapping method

In this chapter, we present the rotational compensator phase unwrapping method [46] to compensate the inconsistencies, and to decrease the effect of each one with increase of distance from SPs. The unwrapped result of this method is similar to that of the methods based on the least square methods; i.e., the rewrapped result is not identical to the original phase map. However, the unwrapping is carried out along successive pixels as similar to the path-following methods. The algorithm is based on a combination of three approaches, which are rotational compensator (RC), unconstrained singular point positioning (USP), and virtual singular points (VSP). The RC method evaluates the compensator directly without any iteration process. However, the accuracy is not much improved by only the RC technique itself. The other two USP and VSP are additional approaches to improve the accuracy. The purpose of

USP approach is to confine the effect of compensator to smaller region and to determine the dipole pairs. While, the VSP technique is used to locate SPs outside the measured area in which wrapped phase is obtained, these SPs have opposite polarities of the corresponding SPs in the measured area.

3.2.1 Rotational compensator technique

As described in section 2.3, the wrapped phase distribution, Ψ, is defined at discrete points called pixels. It is a real valued distribution between $(-\pi, \pi]$ radians as the principal value of an unrestricted phase. Phase unwrapping process is normally carried out by comparing adjoining pixels. If the true phase distribution is continuous and the difference between the phase of adjoining pixels does not exceed a half cycle, this condition is considered as sampling theorem. When the difference is larger than a half cycle, the wrapped phase is shifted one cycle so that the shifted difference is again smaller than a half cycle. This shift operation is same as the wrapping operation used to obtain the principal value of the unrestricted phase Φ, as given in Eq. (2.10). The difference vector between adjoining pixels is defined using the wrapping operator $W[.]$ as follows:

$$\boldsymbol{g}(\boldsymbol{r}, \boldsymbol{r}') \triangleq W\{\Phi(\boldsymbol{r}') - \Phi(\boldsymbol{r})\}\hat{\boldsymbol{s}}(\boldsymbol{r}' - \boldsymbol{r}) \tag{3.1}$$

where $\boldsymbol{r}$, $\boldsymbol{r}'$, and $\hat{\boldsymbol{s}}$ show position of the pixel of interest, position of the adjoining pixel, and unit vector of direction $\boldsymbol{r}' - \boldsymbol{r}$, respectively. If the pixels satisfy the sampling theorem, and the integral of the phase difference is independent of choice of the path, hence, the integral of $\boldsymbol{g}$ along a closed path c is zero:

$$\oint_c \boldsymbol{g} \cdot \hat{\boldsymbol{s}}\, \mathrm{d}l \; = 0 \tag{3.2}$$

In contrast, when some pixels violate the sampling theorem, the integral can take a non-zero value:

$$\oint_c \boldsymbol{g} \cdot \hat{\boldsymbol{s}}\, \mathrm{d}l \; = 2\pi \sum_k m_k = 2\pi K, \qquad m_k \in \{-1, 0, 1\} \tag{3.3}$$

where the right-hand side, K, corresponds to a sum of the number of that not satisfying the sampling theorem, and m_k is residue.

Yamaki and Hirose proposed the idea of introducing a compensator to cancel the singularity [43], which is briefly described in section 2.4.2 as SSPU method. The computations of compensator in SSPU method are dependent on iteration process, in contrast, the RC method computes the compensators directly without any iteration. According to Helmholtz's theorem [44], any vector is represented by sum of two kinds of vectors; i.e., an irrotational vector that is a gradient of some scalar potential, and a rotational vector that is a rotation of a vector potential. Since the unwrapped phase Φ must be a scalar field, the difference vector $\boldsymbol{g}$ in Eq. (3.1) satisfies following equation:

$$\boldsymbol{g} = \nabla\Phi + \nabla \times \boldsymbol{A} \tag{3.4}$$

Applying Stokes' theorem to an integral of the rotation of the above equation over a domain enclosed by a path c, the following relation can be obtained:

$$\oint_c \boldsymbol{g} \cdot \hat{\boldsymbol{s}}\,\mathrm{d}l = \oint_c \nabla \times \boldsymbol{A} \cdot \hat{\boldsymbol{s}}\,\mathrm{d}l \tag{3.5}$$

$$\tag{3.6}$$

Comparing this equation with Eq. (3.3), it can be found that the source of the singularity is the rotation of $\boldsymbol{A}$:

$$\oint_c \nabla \times \boldsymbol{A} \cdot \hat{\boldsymbol{s}}\,\mathrm{d}l = 2\pi \sum_k m_k \tag{3.7}$$

Since this relation is satisfied even for any elementary loop, the vector potential is considered as the superposed result of each vector potential corresponding to each SP:

$$\boldsymbol{A} = \sum_k \boldsymbol{A}_k \tag{3.8}$$

Rearranging Eqs. (3.4), (3.5) and (3.8), the difference of unwrapped phase between two points can be obtained as follows:

$$\Phi(\boldsymbol{r}) - \Phi(\boldsymbol{r}_0) = \int_{\boldsymbol{r}_0}^{\boldsymbol{r}} \nabla\Phi \cdot \hat{\boldsymbol{s}}\,\mathrm{d}l = \int_{\boldsymbol{r}_0}^{\boldsymbol{r}} \left(\boldsymbol{g} - \sum_k \nabla \times \boldsymbol{A}_k \right) \cdot \hat{\boldsymbol{s}}\,\mathrm{d}l \tag{3.9}$$

This equation shows that the singularity of the wrapped difference vector $\boldsymbol{g}$ is compensated by the rotation of vector potential $\boldsymbol{A}_k$. Thus, the integral of rotation of $\boldsymbol{A}_k$ is referred as the rotational compensator (RC).

In order to evaluate each RC, let's consider the cylindrical coordinate of (R, θ, z), where the k-th SP is located at the origin. Each vector potential satisfies the following relation:

$$\oint_c \nabla \times \boldsymbol{A}_k \cdot \hat{\boldsymbol{s}} \, \mathrm{d}l \, = 2\pi m_k \tag{3.10}$$

Each source of singularity has an axial symmetry where every component of the vector $\boldsymbol{A}_k$ is represented only in terms of a function of radial distance R as $\boldsymbol{A}_k = (a_R(R), a_\theta(R), a_z(R))$. Furthermore, the z-component of the unit tangential vector $\hat{\boldsymbol{s}}$ is zero. Therefore, the integrand is reduced as follows:

$$\nabla \times \boldsymbol{A}_k \cdot \hat{\boldsymbol{s}} = \frac{\partial a_z}{\partial R} \boldsymbol{e}_R \times \boldsymbol{e}_z \cdot \hat{\boldsymbol{s}} = -\frac{\partial a_z}{\partial R} \boldsymbol{e}_R \cdot \hat{\boldsymbol{n}}, \tag{3.11}$$

where $\boldsymbol{e}_R$ and $\boldsymbol{e}_z$ are unit vectors for R-axis and z-axis, respectively, and $\hat{\boldsymbol{n}}$ denotes the outward normal unit vector to the path ($\hat{\boldsymbol{n}} = \hat{\boldsymbol{s}} \times \boldsymbol{e}_z$). Since the integrand in the left-hand side in Eq. (3.10) is a regular function except at the origin, the integral path can be modified to an arbitrary path that surrounds the origin. In the case where the path is taken as a circular path with radius R, since $\hat{\boldsymbol{n}}$ is identical to $\boldsymbol{e}_R$, the left-hand side of Eq. (3.10) is readily obtained as $-2\pi R(\partial a_z / \partial R)$. Therefore, the partial derivative is represented as

$$\frac{\partial a_z}{\partial R} = -\frac{m_k}{R}. \tag{3.12}$$

Consequently, the integral along an arbitrary closed path expressed in Eq. (3.10) is rewritten as

$$\oint_c \nabla \times \boldsymbol{A}_k \cdot \hat{\boldsymbol{s}} \, \mathrm{d}l \, = \oint_c \frac{m_k}{R} \boldsymbol{e}_R \cdot \hat{\boldsymbol{n}} \, \mathrm{d}l \tag{3.13}$$

$$\tag{3.14}$$

The integral along a segment of which ends are $\boldsymbol{r}_1$ and $\boldsymbol{r}_2$ is evaluated by taking the closed path c as shown in Fig. 3.1. Since there is no SP in the domain surrounded by the closed path $\boldsymbol{r}_1$, $\boldsymbol{r}_2$, $\boldsymbol{r}_{\Delta_1}$, and $\boldsymbol{r}_{\Delta_2}$, the integral along the closed path vanishes. Each of the integrals along the two straight lines also vanishes because the normal unit vector is perpendicular to the $\boldsymbol{e}_R$. Thus, the compensator for the SP that is the integral along the segment may be estimated from the integral along the semicircle as follows:

$$\begin{aligned} C_k(\boldsymbol{r}_1, \boldsymbol{r}_2) &\triangleq -\int_{\boldsymbol{r}_1}^{\boldsymbol{r}_2} \nabla \times \boldsymbol{A}_k \cdot \hat{\boldsymbol{s}} \, \mathrm{d}l \, = -\int_{\boldsymbol{r}_1}^{\boldsymbol{r}_2} \frac{m_k}{R} \, \boldsymbol{e}_R \cdot \hat{\boldsymbol{n}} \, \mathrm{d}l \\ &= \int_{\boldsymbol{r}_{\Delta 1}}^{\boldsymbol{r}_{\Delta 2}} \frac{m_k}{R} \, \boldsymbol{e}_R \cdot \hat{\boldsymbol{n}} \, \mathrm{d}l \, = \int_{\theta_{1,s_k}}^{\theta_{2,s_k}} \frac{m_k}{\Delta} \boldsymbol{e}_R \cdot (-\boldsymbol{e}_R) \Delta \, \mathrm{d}\theta \\ &= -m_k \left(\theta_{2_{s_k}} - \theta_{1_{s_k}} \right) \end{aligned} \tag{3.15}$$

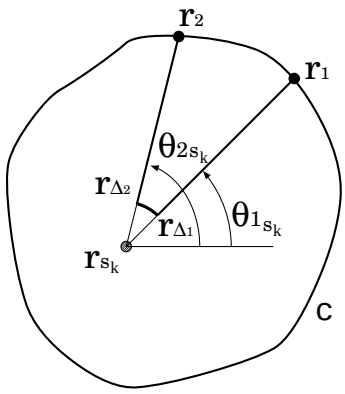

Figure 3.1: *Configuration to compute the rotational compensator*

where θ denotes the unbounded azimuthal angle from the x-axis and also $\theta_{2_{s_k}} > \theta_{1_{s_k}}$, and Δ is the distance between the points $\boldsymbol{r}_{\Delta_1}$ and $\boldsymbol{r}_{\Delta_2}$.

Taking the $\boldsymbol{r}_1$ and $\boldsymbol{r}_2$ in Eq. (3.15) as the adjoining pixels $\boldsymbol{r}$ and $\boldsymbol{r}'$, respectively, the wrapped phase can be unwrapped by applying the wrapped difference vector $\boldsymbol{g}$ and the compensators C_k as follows:

$$\Phi(\boldsymbol{r}') = \Phi(\boldsymbol{r}) + \boldsymbol{g}(\boldsymbol{r}, \boldsymbol{r}') \cdot \hat{\boldsymbol{s}}(\boldsymbol{r}' - \boldsymbol{r}) + \sum_k C_k(\boldsymbol{r}, \boldsymbol{r}'). \tag{3.16}$$

The compensator of a SP spreads throughout the whole measurement area. It shares a similar nature with the methods based on the least square approach, in which the effect of SPs also spread [10]. However, it is found that the compensator decreases with increasing R because the distance between $\boldsymbol{r}'$ and $\boldsymbol{r}$ is always kept constant at one pixel width. This characteristic is similar to path-following methods, in which the effect of a SP is confined into the region that surrounds the branch cut.

3.2.2 Unconstrained singular point positioning

The RC can remove the inconsistency by canceling the singularity effect. However, it introduces an undesired distortion of phase in wide area. In order to limit the distorted area in the narrower region around SP, unconstrained singular point positioning technique (USP) is proposed.

The RC, C_k, defined in Eq. (3.15) cancels a singularity of single SP. The effect of this single SP can be considered as a monopole, which is proportional to the reciprocal of the distance R:

$$\boldsymbol{E}_{\text{monopole}} = -\frac{1}{R}\boldsymbol{e}_R. \tag{3.17}$$

If there is another SP with opposite sign is located near the original one; this case corresponds to a dipole. The effect of the dipole in two-dimensional space is evaluated as follows:

$$\boldsymbol{E}_{\text{dipole}} = -\frac{1}{R^2}\left(2(\boldsymbol{d}\cdot\boldsymbol{e}_R)\boldsymbol{e}_R - \boldsymbol{d}\right), \tag{3.18}$$

where $\boldsymbol{d}$ is the difference vector from the negative SP to the positive SP, and the origin is taken at the center of the two SPs. The decay of the effect induced by SP dipole is faster than that by monopole SP. It is known that the distance of the nearest SP with an opposite sign is shorter than that with a same sign from an analysis of an actual noisy experimental wrapped phase [14]. Therefore, if every SP belongs to a dipole, the effect of compensator is $|\boldsymbol{d}|/R$ times smaller than that of a single compensator, and it means the effect is confined in a local region around the dipole.

SP is generally positioned at the center point of an elementary path that consists of four pixels aligned with square shape, and the minimum $|\boldsymbol{d}|$ is limited to the pixel size. If the accurate position of each SP is obtained, and if the distance of the dipole is closer than the pixel size, the effect of compensator is limited to a narrower region.

It is found from Eq. (3.15) that the compensator of a segment is represented as the difference of the azimuthal angle between the ends of the segment. This means that the following model of wrapped phase maps with singularities can be considered:

$$\Phi(\boldsymbol{r}) = W\{m\theta(\boldsymbol{r},\boldsymbol{r}_s) + \bar{\phi} + \delta\phi(\boldsymbol{r})\}, \qquad (m \in \{-1,+1\}), \tag{3.19}$$

where $\bar{\phi}$ and $\delta\phi(\boldsymbol{r})$ are a phase average and a non-singular phase fluctuation, respectively. Let's consider the following wrapped difference between adjacent pixels:

$$\Delta \triangleq W\{W\{\Phi' - \Phi\} - m(\theta' - \theta)\}, \tag{3.20}$$

in which the main feature means quantities at adjacent pixels. Substituting Eq. (3.19) to the difference and applying a characteristic of wrapping operator as $W\{W\{\Psi\}\} \equiv W\{\Psi\}$, the

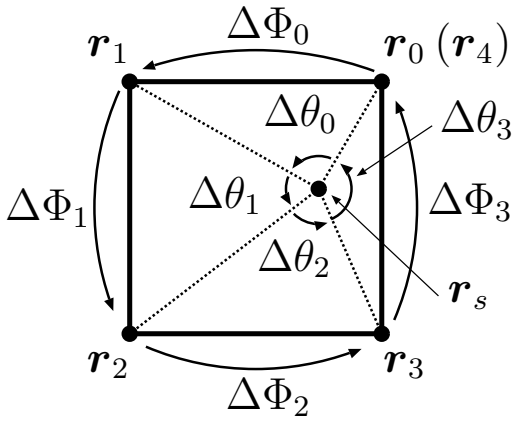

Figure 3.2: *Elementary path including an unconstrained singular point: The $\Delta\theta_l$ means the facing angle of the side with the ends $\boldsymbol{r}_l$ and $\boldsymbol{r}_{l+1}$. The $\Delta\Phi_l$ means the difference of the wrapped phases.*

wrapped difference can be reduced to:

$$\Delta = W\{\delta\phi' - \delta\phi\}. \tag{3.21}$$

This relation suggests that a minimum solution of $|\Delta|$ is equivalent to a solution minimizing $|W\{\delta\phi' - \delta\phi\}|$, hence, it can be assumed that the unknown phase fluctuation $\delta\phi$ is small. therefore, the problem to determine $\boldsymbol{r}_s$ is reduced to how can find the solution with minimized $|\Delta|$ in Eq. (3.20). Thus, the problem is defined by means of a nonlinear least square problem as follows:

$$\text{minimize } \sum_{l=0}^{3} \Delta^2 = \sum_{l=0}^{3} \Big(W\{W\{\Delta\Phi_l\} - m\Delta\theta_l(\boldsymbol{r}_s)\} \Big)^2, \tag{3.22}$$

$$\Delta\Phi_l \triangleq \Phi_{l+1} - \Phi_l, \quad \Phi_4 = \Phi_0, \tag{3.23}$$

$$\Delta\theta_l \triangleq \theta_{l+1}(\boldsymbol{r}_s) - \theta_l(\boldsymbol{r}_s) > 0, \quad \theta_4 = \theta_0 + 2\pi, \tag{3.24}$$

where l denotes the identifier of a segment or a pixel in an elementary loop shown in Fig. 3.2, and $l \in \{0, ..., 3\}$. Because this nonlinear minimization problem is difficult to solve analytically, a numerical method based on a genetic algorithm [45] is applied.

The developed algorithm (RC) spreads singularities effect of each SP throughout the whole measurement area includes the regular regions that do not have any SPs similar as LS-DCT method [25] and SSPU method [43]. However, LS-DCT method spreads the singularity in the regular regions with same amplitude of phase errors, as shown in Fig. 2.8(b); whilst the phase

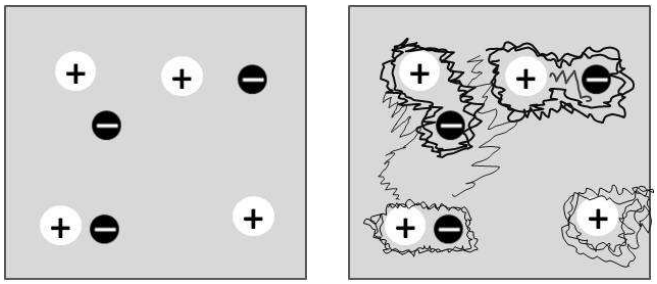

(a) (b)

Figure 3.3: *Spreading of errors in regular regions due to the RC method handling way for the singularity regions in the phase map: (a) SPs distribution map, (b) phase errors appear in regular regions.*

errors produce due to the using of SSPU method is decreased at the regions that are far from SPs positions, as illustrated in Fig. 2.10(b), however, these errors are big enough to affect the accuracy of SSPU method during producing its unwrapped phase results. Meanwhile, the RC method has the merit that the phase error for adjacent SPs dipoles is reduced than that errors of SSPU method. This is due to that the RC method uses USP technique to determine the SPs positions, hence, the distance between these dipoles becomes shorter and the effect of their singularities will be small than that effect produced in SSPU method. Figure 3.3 presents the errors appear in the regular regions of the phase map due to the handling way of the RC method for singularity regions. The example of SPs distribution map is shown in Fig. 3.3(a), while Fig. 3.3(b) illustrates the phase error locations.

3.2.3 Virtual singular points

Since the measurement area is finite, there are some isolated or split-dipoles SPs with long distances. The isolated SPs spread error throughout the entire measurement area. When virtual SPs (VSPs) having an opposite sign of the isolated SPs outside the area is found, the VSPs and the isolated SPs make dipoles, and then the error may be reduced. In the case where the isolated SP is located near the border of the area, the virtual SP is put at the symmetrical point to the border outside the area so that the center of the dipole is located just on the border. To find isolated SPs near the border, the following approach is attempted; schematic example is shown in Fig. 3.4.

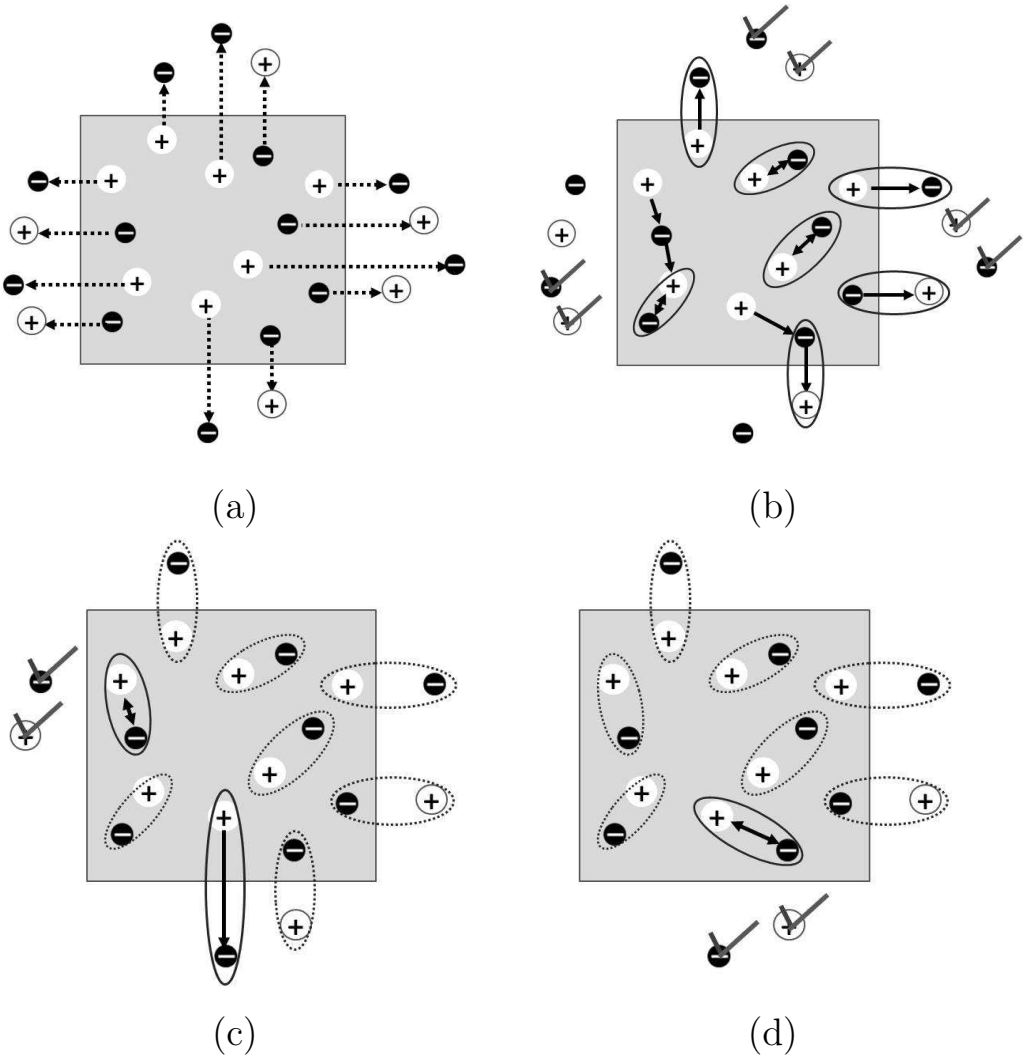

Figure 3.4: *Determination of dipole pairs: (a) definition of the virtual SP candidates, each dashed arrow shows the correspondence between original and virtual SP; (b) search nearest SP and pairing in the first iteration: each arrow shows the nearest opposite-signed SP, the SPs encircled are paired as dipoles, the checked virtual candidate is removed from the list of candidates in subsequent steps; (c) the second iteration: SPs enclosed with dashed ellipse have been already paired; (d) elimination of removable virtual SP pairs.*

(1) Preparation:

Mark all SPs as ‘isolated’.

For each SP, locate the symmetrical point to the nearest border point. The symmetrical point is defined and marked as a VSP candidate with opposite sign. The VSP candidates are shown as the end of arrow in Fig. 3.4 (a).

(2) Find the nearest SP:

For every SP with the mark ‘isolated’, find the nearest SP with opposite sign among SPs marked as ‘isolated’, also including the VSP candidate corresponding to the original SP.

(3) Virtual SP determination:

If the nearest SP is the VSP candidate, the original SP is marked as ‘dipole with virtual’, and the VSP candidate is marked as ‘virtual’. The pair of them is shown as an encircled pair with single headed arrow shown in Fig. 3.4 (b). In the figure the VSP candidates with checked symbol are eliminated in subsequent steps.

(4) Dipole determination:

For each positive SP with the mark ‘isolated’, if the nearest negative SP has no other positive SP that is closer than the original one, then both of the SPs are marked as ‘internal dipole’. The pair of them is depicted as an encircled pair with double headed arrow, as shown in Fig. 3.4 (b). The virtual candidates corresponding to these SPs are removed from the virtual candidates list.

(5) Repeating:

Repeat procedures from (2) to (4), until no more SPs marked with ‘isolated’ are found. After this step, all SPs are marked as ‘internal dipole’, ‘dipole with virtual’, or ‘virtual’. See Fig. 3.4 (c).

(6) Elimination of removable VSP pair:

For each SP that marked ‘dipole with virtual’, if the nearest opposite signed SP within the SPs located inside the border is also marked as ‘dipole with virtual’, let us examine whether this pair can become a new pair. If the twice distance of the new pair is shorter than the sum of the distances between the SP and the current partner with the mark ‘virtual’, the total branch cut length is shorter than the current pairs. In this case, the new pair is coupled and the old partners ‘virtual’ are removed; as shown in Fig. 3.4 (d).

3.3 Results and discussion

3.3.1 Simulated phase data

True phase in experimental result is unknown. Hence, to examine characteristics of unwrapping methods, a wrapped phase map that is a result from a known unwrapped phase map is used instead of a wrapped phase map obtained by an experiment. The prepared original continuous phase map is a noisy phase map with constant gradient; the image size is 100×100 pixel^2, the gradient is $(0.1, -0.1)$ cycle/pixel, and the noise has a normal distribution with 0.15 cycle standard deviation. The true phase map is shown in Fig. 3.5(a) together with its wrapped phase. In this wrapped phase the numbers of positive and negative SPs are 453 and 456, respectively, overall comprising almost 9% of number of all pixels. It should be noted that there are 3 unbalanced SPs which cannot make pairs even when coupling with longer distance is permitted. The distances of some USP dipoles are shorter than those of the original dipoles which consist of the constrained SPs. The distribution of distances between each positive SP and its nearest negative SP is shown in Fig. 3.6. From the distribution of the constrained SPs that are located in center of elementary loops, it is found that most of the distances are concentrated at 1 or $\sqrt{2}$. In contrast, the average distance of USPs is significantly shorter than that of constrained SPs. This suggests that the effect of compensator with the use of USP is confined in a narrower region than with constrained SP positioning.

In order to compare the characteristics, several algorithms are applied, which are Goldstein's path-following method [11], LS-DCT [25], SSPU [43], and the RC algorithm. Some results of the unwrapped phase maps together with their rewrapped phases are shown in Fig. 3.5(b)-(d). It can be noticed that some continuous phase gaps are found in the unwrapped phase map obtained by the Goldstein's method shown in Fig. 3.5(b). Although the unwrapped phase maps by both LS-DCT and RC methods shown in Fig. 3.5(c) and (d) have no phase gap, a smaller number of stripes in their rewrapped phase results than the original wrapped phase is found. This indicates that the gradient of unwrapped phase was underestimated. To demonstrate a quantitative comparison, gradients of the unwrapped phase maps are shown in table 3.1. In the table, the gradients are obtained by fitting to a planar function; i.e., $\tilde{\phi}(\boldsymbol{r}) = \nabla\tilde{\phi} \cdot \boldsymbol{r} + \tilde{\phi}_0$, and σ denotes the mean residual that is defined as a square root of a mean square residual from

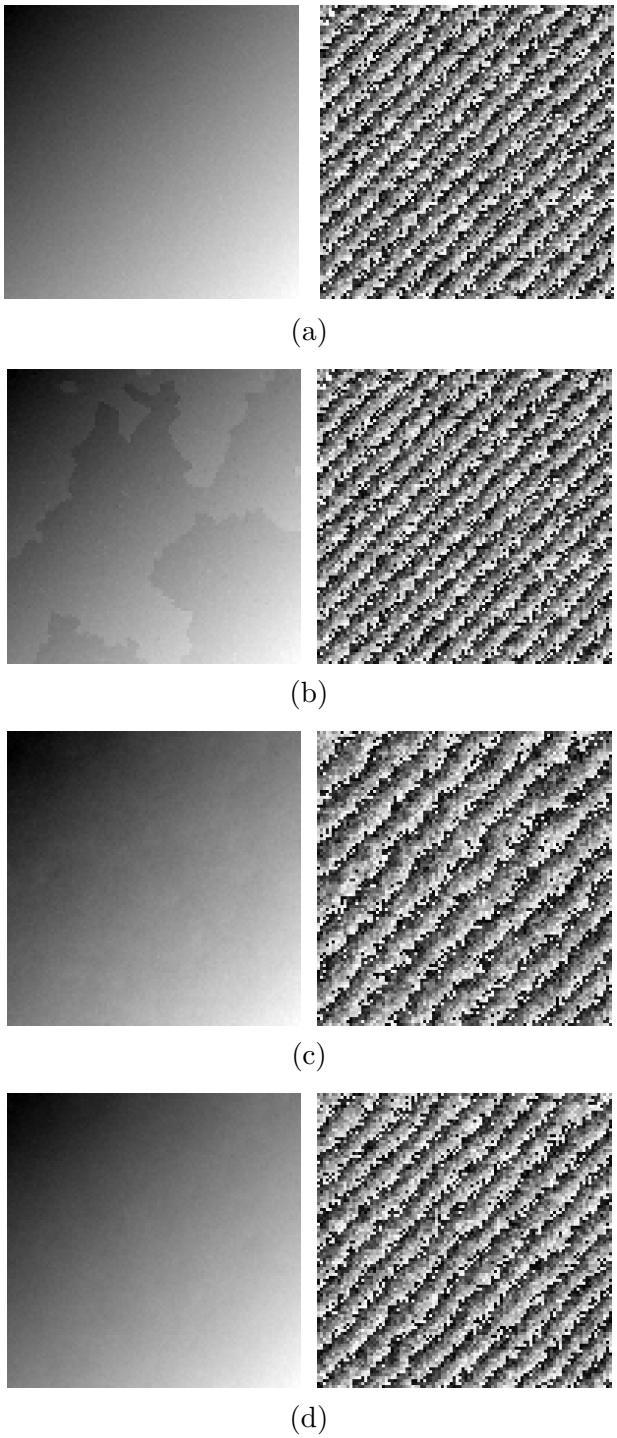

Figure 3.5: *Unwrapped and rewrapped phase map of simulated phase data has noise with* $\sigma = 0.15$ *cycle: In each figure, the left-hand side figure shows original or unwrapped phase map where phase increases with increasing of brightness, and the right-hand side figure shows wrapped or rewrapped phase map. (a) original phase map, (b) Goldstein's path-following method, (c) least squares method with DCT, (d) RC method.*

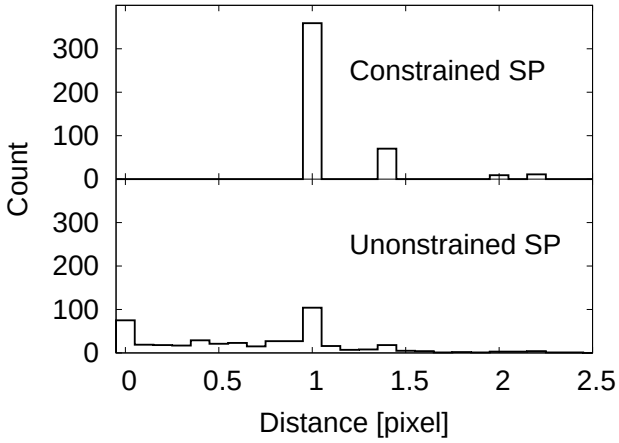

Figure 3.6: *Frequency histogram for distance from a positive SP to the nearest negative SP.*

$\tilde{\phi}$. Even in original data, the σ is not equal to zero because the original data contains the noise with the given standard deviation. The errors of gradient and mean residual, $\Delta\left(\nabla\tilde{\phi}\right)$ and $\Delta\sigma$, are estimated as the normalized difference between the unwrapped result and the original one, where the normalizing factor is the reciprocal of original one. From the table it is found that the gradients are underestimated by all of the algorithms. The best result in terms of $\Delta\left(\nabla\tilde{\phi}\right)$ and $\Delta\sigma$ is found for the unwrapped phase result obtained by RC method in which all of the approaches are applied: the rotational compensator, the unconstrained SP, and the virtual SP. Goldstein's method has a large $\Delta\sigma$. The reason of this is evident from the unwrapped image shown in Fig. 3.5(b); there is a continuous set of gaps. From the comparison in table 3.1 for the unwrapped results obtained by LS-DCT and SSPU methods, it is found that the errors of them are nearly same. In these methods, the inconsistencies by SPs are canceled; however, imbalance of the number of positive and negative SPs is not considered.

From a comparison among the last four rows in table 3.1, it seems that the virtual SP approach is more effective to improve the accuracy of the gradient, and the unconstrained SP positioning is more effective to reduce the error of the mean residual. These results can be explained by the nature of each approach. The error of the gradient shows global error, while the mean residual shows local error from the global distribution of the unwrapped phase. If isolated SPs that are not SPs containing dipoles are found in the measured area, the compensator affects the entire area, which should otherwise be confined into a local area. Since the virtual SPs are applied to avoid the existence of such isolated SPs, the global error of is reduced.

Algorithm	Gradient ($\nabla\tilde{\phi}$)	$\Delta\left(\nabla\tilde{\phi}\right)$ [%]	σ	$\Delta\sigma$ [%]
Original	(0.1000 , –0.1000)	(— , —)	0.149	—
Goldstein	(0.0892 , –0.0826)	(–10.8 , –17.4)	0.425	+184.9
LS-DCT	(0.0742 , –0.0731)	(–25.8 , –27.0)	0.179	+20.0
SSPU	(0.0743 , –0.0730)	(–25.7 , –27.0)	0.178	+19.7
RC(only)	(0.0816 , –0.0722)	(–18.4 , –27.9)	0.182	+21.7
RC(USP)	(0.0860 , –0.0756)	(–14.1 , –24.5)	0.173	+15.9
RC(VSP)	(0.0866 , –0.0860)	(–13.4 , –14.0)	0.186	+24.5
RC(USP+VSP)	(0.0908 , –0.0894)	(–9.2 , –10.6)	0.168	+12.3

Table 3.1: *Accuracy comparison among algorithms by planar function fitting for the simulated phase data with* 0.1 *[cycle/pixel] constant gradient and has noise with* 0.15 *[cycle] standard deviation. 'RC(only)' represents the case when the unwrapped result is obtained by using RC technique only; 'RC(USP)' in the case of using RC and USP techniques; 'RC(VSP)' when uses RC and VSP techniques; while 'RC(USP+VSP)' represents the case when using all technique (RC, USP, VSP) to obtain the unwrapped result.*

On the other hand, since it is found that the unconstrained SP positioning can make dipoles with shorter range, as shown in Fig. 3.6, the compensator to remove the dipole affects only a narrower region. These observations can be confirmed from the visualized images shown in Fig. 3.7. This figure shows the unwrapped results with contour lines for the for cases of using these techniques; where Figs. 3.7(a), (b), (c), and (d) present the unwrapped results obtained when use RC technique only, RC technique with using USP approach only, RC technique with using VSP approach only, and RC technique with using both USP and VSP approaches, respectively. by count the number of contour lines in each unwrapped result and compare this with the number of stirp line in the wrapped phase data shown in Figs. 3.5(a). It can be found that, when use RC technique only the number of contours is 14 line; while it is 15 lines when use RC technique with using USP approach only. In the case of using RC technique with using VSP approach only, the number of lines is 16, and it is 17 when use all approaches (RC, USP, VSP). Meanwhile, the number of stirps in the wrapped data is 20 line It can be inferred from above discussion, that by using the all approaches the developed RC algorithm has good accuracy but still under-estimation.

We consider the following two reasons why the developed RC method with all the approaches

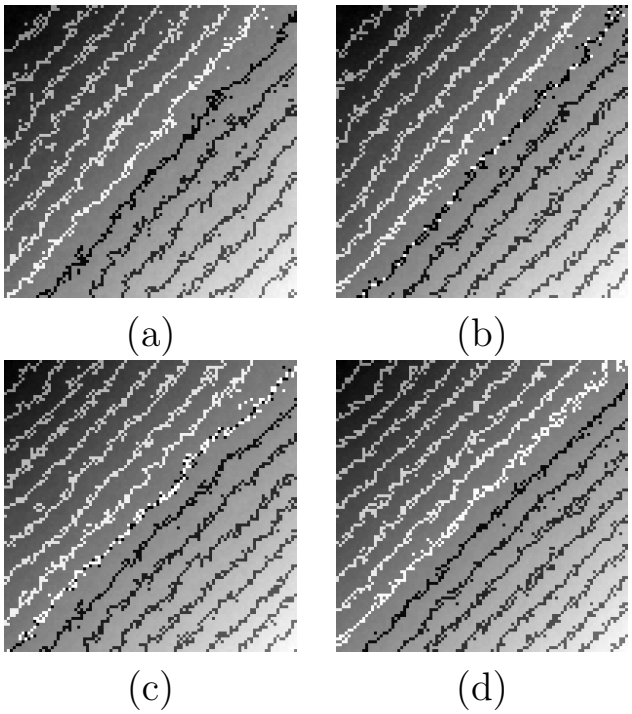

Figure 3.7: *Unwrapped phase results with contour lines for simulated noisy data with* 0.15 *cycle standard deviation, obtained when uses: (a) RC technique only, (b) RC technique with using USP approach only, (c) RC technique with using VSP approach only, (d) RC technique with using both USP and VSP approaches.*

still has some error. The first is the position of the VSP; due to there is no empirical basis to put the VSP at a symmetrical point to the nearest border. Even if the position of a VSP differs slightly from the true SP outside the region, the VSP still makes a dipole; therefore, the effect to the global error corresponding to the error of the gradient may be small. A more significant source of error in terms of VSP is induced by incorrect coupling through the method shown in section 3.2.3. If the detected isolated SPs are incorrect, the position of each VSP is taken at a more distant point from the true SP, and then it can induce the global error. The second source is the model to determine the wrapped phase shown in Eq. (3.19). If the fluctuation $\delta\phi$ is not sufficiently small, the approach to determine the USP is not suitable. This may affect to the local error corresponding to the error of the mean residual.

Figure 3.8 shows a comparison of required computational time for the LS-DCT and the RC methods to obtain their unwrapped phase results. In the method based on the RC the computational time is almost proportional to N^4 with $N > 200$, where N denotes the one-dimensional

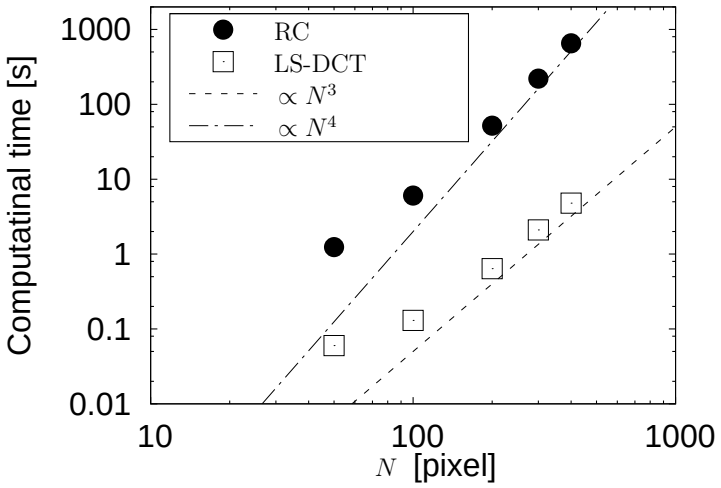

Figure 3.8: *Computational time: The horizontal axis N denotes one-dimensional area size in pixels. The computational time is measured with a PC including CPU of Intel Core 2 DUO (TM) with 2.13GHz clock in a single CPU operation mode.*

area size in units of pixels; this trend is reasonable. In these cases, when the overhead to the main computation is negligible, most of time is elapsed in evaluations of compensation. The amount of evaluation time is proportional to both the number of SPs and the number of the segments of path to be compensated. Since both are proportional to the area size ($\propto N^2$), the total evaluation time is proportional to N^4. In contrast, the computational time increases with N^3 in the method using LS-DCT. In this computation, a simple algorithm not a fast Fourier transform is used, but a two-dimensional buffer is used. Through the use of the buffer, the computational time of two-dimensional cosine transforms needs only N^3 multiplications. Thus, the method based on the RC is more time-consuming than that of LS-DCT.

3.3.2 Unwrapping for interferogram data

In order to demonstrate validity of the developed RC method to the actual experimental data, we applied the method to measuring the phase shift in candle flames. The result is shown in Fig. 3.9. The fringe shown in Fig. 3.9(a) is obtained by a Mach-Zehnder interferometer with existing of the candle flame. The fringe pattern is a superposed result of object light passing through the candle flame upon the reference light. The SP distribution map is shown in Fig. 3.9(c), where the S/N is low in fringe patterns. The difference between the simulation

data in the previous section and the experimental data is found in this distribution. The amount of SPs in all pixels within the image size 256×170 pixel^2, reaches around 6% for all pixels. The unwrapped results obtained by the LS-DCT [25] and developed RC methods are shown in Fig. 3.9(d) and (f), respectively. To evaluate the characteristics of the phase unwrapping methods, the rewrapped phases for the studied algorithms are also shown in Fig. 3.9(e) and (g). From a comparison between the original wrapped phase, shown in Fig. 3.9(b), and the rewrapped phase results obtained by each algorithm, we can find that the number of stripes in rewrapped results of the studied methods is less than that in wrapped phase data. However, the results of the RC method has the nearest number of stripes to the wrapped data, which shows the highest accuracy.

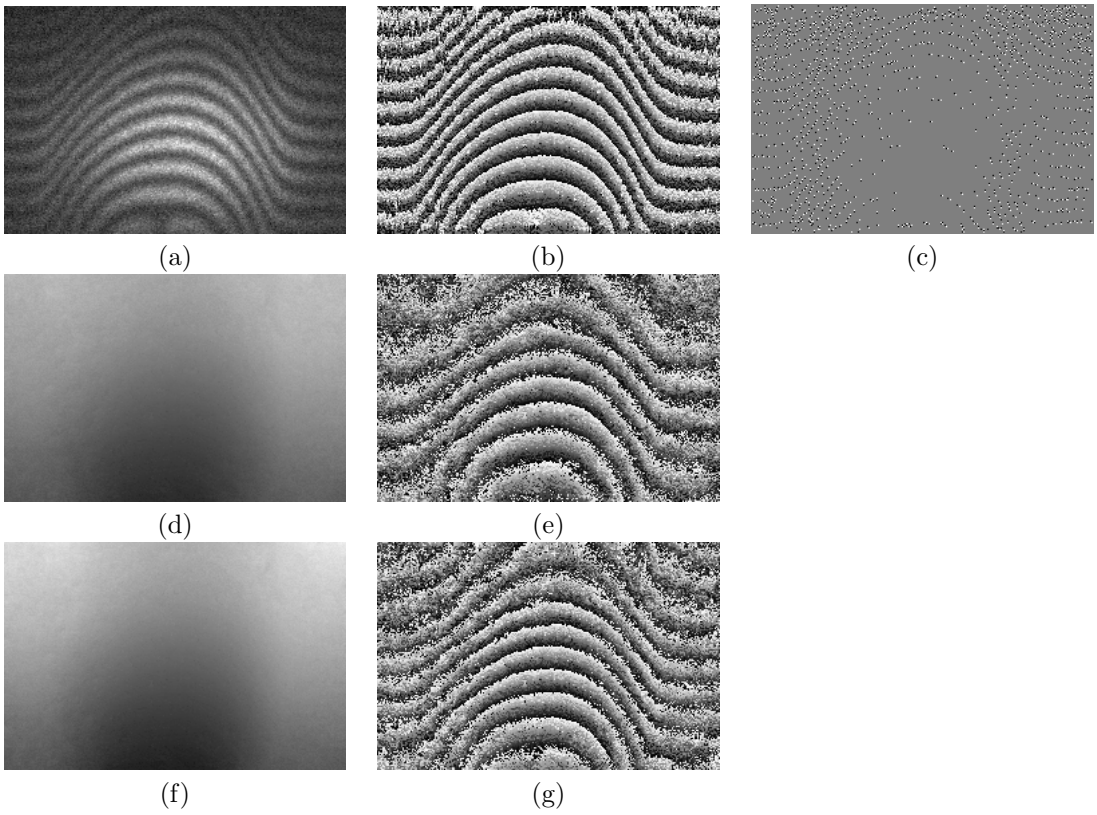

Figure 3.9: *Unwrapped phase of fringe by Mach-Zehnder interferometer for candle flame: (a) fringe pattern obtained with existence of flame, (b) wrapped phase map obtained by Fourier domain method, (c) SPs distributions, (positive and negative SPs are represented by white and black dots, respectively), (d) & (e) unwrapped and rewrapped phases map obtained by LS-DCT method, (f) & (g) unwrapped and rewrapped phases map obtained by the developed RC method.*

3.4 Conclusions

The developed phase unwrapping using rotational compensator method has been proposed for noisy phase data. This method is based on a combination of three approaches; RC, USP, and VSP. The RC acts to compensate the singularity of each SP for all unwrapping paths. The USP technique provides freedom to adjust SP positioning in order to improve accuracy of compensation. Since it can make some dipoles that have shorter distances than the pixel size, the undesired, longer effect of compensator is suppressed. The VSPs technique applies for unpaired SPs, isolated SPs are taken outside the area to confine the effect of compensator in local narrow regions around SPs.

In the comparisons of several methods of phase unwrapping through both a numerical simulation and an analysis of experimental fringe pattern, the RC method demonstrates good accuracy of unwrapping although it does not eliminate the phase error with underestimation. However, the RC method has a drawback of undesired phase error because the RC should be applied to the regular region with no SPs as well as to the singular region. In addition, the RC method required high computational time cost when the measured phase data contains many SPs. Hence, further research to reduce these drawbacks is needed to produce more accurate and efficient phase unwrapping. This is what is done in the following chapter.

CHAPTER 4

ROTATIONAL AND DIRECT COMPENSATORS PHASE UNWRAPPING ALGORITHM

- Introduction
- Basic concepts
- Direct compensator technique
- Phase unwrapping by RC and DC algorithm
- Results and discussion
- Conclusions

Chapter 4

Rotational and direct compensators phase unwrapping algorithm

4.1 Introduction

Here, we introduce a new phase unwrapping approach for noisy wrapped phase maps of continuous objects to improve the accuracy and computational time requirements of phase unwrapping using a rotational compensator method. The proposed algorithm is based on compensating the singularity of discontinuity sources. It uses direct compensation for adjoining SP pairs, and uses rotational compensation for other SP pairs.

In a manner similar to the phase unwrapping algorithm developed by Tomioka et al. [46], the main issues determine the behavior of the proposed algorithm: the RC, USP positioning and VSP approaches to compensate the inconsistencies and to confine the effect of each one in a local region. The proposed algorithm is based on their method, however, the way of computing the compensators for adjoining SPs pairs is different from RC.

4.2 Basic concepts

Phase unwrapping is an essential process of removing discontinuities by local neighborhood tests and corrections to produce consistent unwrapped phase maps. When a closed loop in a phase map includes SP, the integral along the loop will have a value of $-2\pi S$, where S is the residue of the SP, as shown in Eq. (2.13) in chapter 2. Representing an integral of a segment i, which is a member of the loop comprising N segments, as C^i, we can reduce Eq. (2.13)

$$\sum_{i=0}^{N-1}(\hat{\bigtriangledown}\Psi^i + C^i) = 0. \tag{4.1}$$

This suggests that the singularity of Ψ^i is regularized by compensator C^i, and phase unwrapping becomes an independent path. The RC for the i-th segment which is a path from $\mathbf{r}_i$ to $\mathbf{r}_{i+1}$ to cancel the singularity of the j-th SP, ${}^{R}C_j^i$, is represented as follows:

$$ {}^{R}C_j^i = -S_j(\theta_{i+1,j} - \theta_{i,j}), \tag{4.2}$$

where S_j denotes the residue of the j-th SP, $\theta_{i+1,j}$ and $\theta_{i,j}$ are azimuthal angles of both ends of the i-th segment, where the origin is located at the j-th SP.

When the measured data contains several SPs, the total compensator of the i-th segment is estimated as the summation of the ${}^{R}C_j^i$ with respect to j:

$$ {}^{R}C^i = \sum_{j=1}^{N_s} {}^{R}C_j^i. \tag{4.3}$$

where N_s denotes number of SPs in the phase map. Consequently, we can retrieve the true unwrapped phase data by summing the phase differences between the adjoining pixels and the total compensators as follows:

$$ \Phi_M = \Phi_0 + \sum_{i=1}^{M} (\hat{\bigtriangledown}\Psi^i + C^i), \tag{4.4}$$

where $C^i = {}^{R}C^i$.

It is noteworthy that Eq. (4.4) is the modification of Eq. (2.12) after removing the effect of SPs by compensating each SP with the compensator which has the opposite sign of SP. However, if the measured phase data contains several SPs, the computations of each compensator becomes a time-consuming process; this is one of the drawbacks of the RC method.

Despite the RC which can remove the inconsistencies in the phase map by eliminating the effect of singularity, it introduces an undesirable distortion of phase in a wide area. The effect of the RC for the j-th SP, ${}^{R}C_j^i$, is decreased with increasing the distance from that SP. It becomes small for the distant segment, however, it is not exactly zero. This means that RC affects the regular region and its effect is considered as an error of phase unwrapping. The effect of single SP, monopole SP, is proportional to the reciprocal of the distance R from the residue:

$$ |{}^{R}C_j^i| \propto \frac{1}{R}. \tag{4.5}$$

In contrast, phase unwrapping method based on avoiding branch cuts does not affect the distant segment at all. In other words, the branch cut approach can precisely confine the singularity of SP pairs within local region, but the RC method spreads the effect of singularity to the whole region. This is another drawback of RC method.

4.3 Direct compensator technique

Every SP has a residue of ± 1, and a pair of two SPs with different polarities is considered as a dipole. It was found from the distribution of SP dipole distances that there are a lot of dipole pairs with short distances [14]. Figure 4.1 shows an example of the dipole distance distribution for wrapped phase data. It can be seen that many dipoles are distributed around one pixel distance. Based on this finding, we have proposed a new phase unwrapping algorithm. The proposed algorithm reduces the drawbacks of the RC method, which are high computational time cost and undesired phase errors due to the RC effect on regular regions that have no SPs. The proposed algorithm offers simple computations to compensate the inconsistencies caused by the pairs of the adjoining SPs by adding a direct compensator (DC), so, the effect of each SP is confined within a closer local region. As a result, the drawbacks of RC method can be improved. The RC along a segment is defined by computing the summation of the differences between the azimuthal angles for the end points of that segment for all SPs, in which each SP is located at the origin, as illustrated in Eqs. (4.2) and (4.3). Hence, the summation value of the RC along all segments of 2×2 square loop should be equal to the summation of $\hat{\bigtriangledown}\Psi^i$ along the path with the opposite sign, as shown in Eq. (4.1). In DC case, the compensator value along the segment which crosses branch cut of adjoining pair equals to the value of the phase jump which is one cycle (2π radian).

An adjoining pair is a dipole consists of two SPs with opposite sign separated by one pixel horizontally or vertically. Figure 4.2 shows the configuration of the branch cuts placed between the adjoining SPs in the phase map and the concept of the direct compensation, for simplicity the SPs positions are defined at the center of the closed loops. In this figure, the thick arrows across the branch cut, which are shown as thick dashed lines, represent the positions of DCs. Figure 4.2(a) shows a case in which the branch cut is placed between a pair of

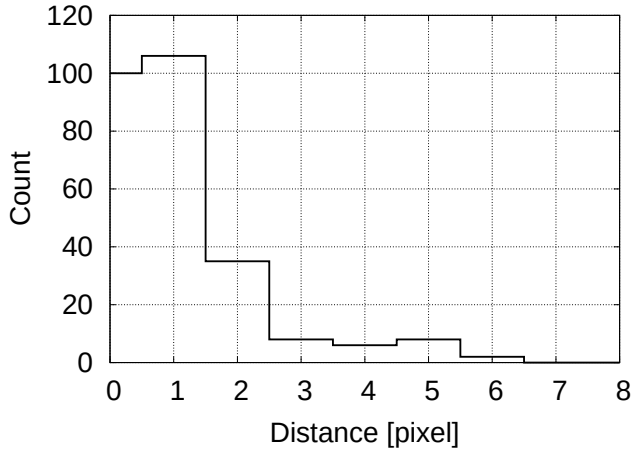

Figure 4.1: *Example of dipole distance distribution: the dipole distance is defined as the distance between one SP and the closest SP with opposite polarity.*

adjoining SPs horizontally, so that the DC will be added to the vertical segment which crosses the branch cut. The compensator value of the segment is divided into two compensator values and distributed through the two adjacent loops which contain the adjoining SPs, as illustrated in Fig. 4.2(b). The following equation explains the DC of a segment that is related to the adjoining pair:

$$ {}^{D}C_j^i = \begin{cases} T_j^i \pi S_j & \text{when the segment number } i \text{ is a member of the loop that} \\ & \text{has the } j\text{-th SP, which belongs to the adjoining pair;} \\ 0 & \text{otherwise;} \end{cases} \tag{4.6} $$

where T_j^i denotes the sign direction of ${}^{D}C_j^i$, and S_j denotes the residue of the j-th SP. When the DC of a segment is added, the sign direction of the DC for this segment, T_j^i, is dependent on the position of this segment with respect to the location of the tested SPs. For example, when a vertical segment is on the right-hand of the tested SP, the sign of T_j^i is negative "$-$", and vice versa, as shown in Fig. 4.2(b). On the other hand, Fig. 4.2(c) shows the case in which the branch cut is placed vertically between the adjoining SPs and the DC is added horizontally. Thus, when the segment is above the tested SP, the sign of T_j^i is positive "$+$", and vice versa, as shown in Fig. 4.2(d).

Also, it is important to discuss the complex distribution of SPs positioning patterns and how we compensate the singularities of these SPs. Figure 4.3 represents an example of the distribution with four SPs in the phase map. If we consider the distribution of these SPs in a

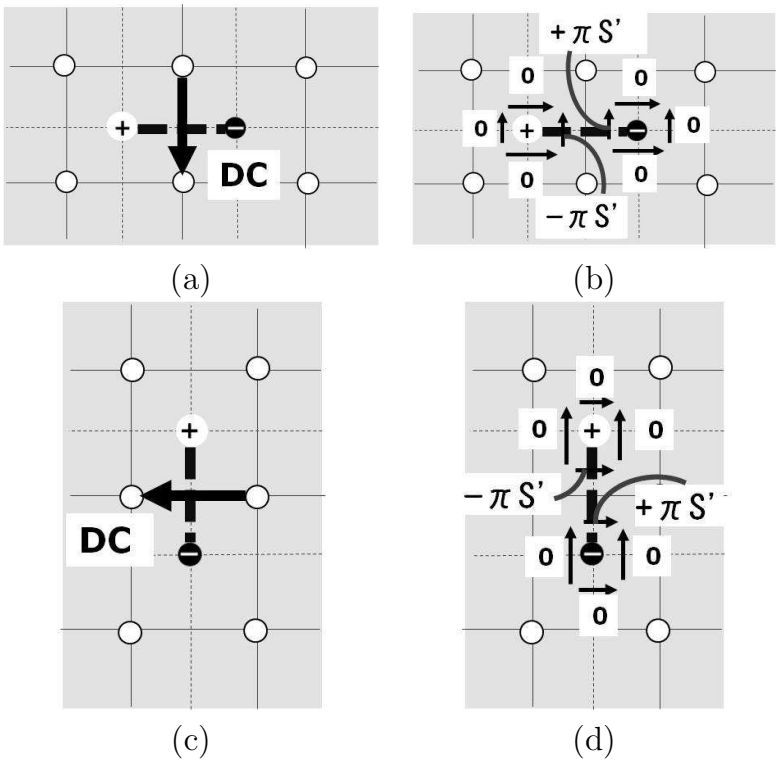

Figure 4.2: *The existence of the branch cuts between the adjoining SPs and the concept of direct compensation: the thick dashed line denotes the branch cut that connects two SPs of opposite sign, compensator position is denoted by thick arrow, the thin arrows show the direction and distribution of compensators for the segments of each SP where S and S' denote the residues of the SPs.*

discrete values, the distance between each other will be the same, as shown in Fig. 4.3(a). Therefore, it will be difficult to determine which SPs are the closest couple to each other, to form pairs. However, if we use USP technique to obtain an accurate positioning of each SP, as shown in Fig. 4.3(b), we can pick a SP and another one nearby, to form a pair. Therefore, the distance between the two SPs of each pair will be defined precisely and the type of pair will be distinguished without difficulty. Thus, DC is added to the adjoining pairs, as illustrated in Fig. 4.3(b).

Since the DC affects just on the branch cut, the effect of the compensator does not propagate to the regular region. Moreover, the DC of a segment i for all SPs, ${}^{D}C^{i}$, needs only two computations in contrast to the RC for another segment i, ${}^{R}C^{i}$, which needs multiple computations to evaluate effects of all SPs, according to Eq. (4.3). Therefore, the computational time requirements of the proposed algorithm for computing total compensators will be reduced and

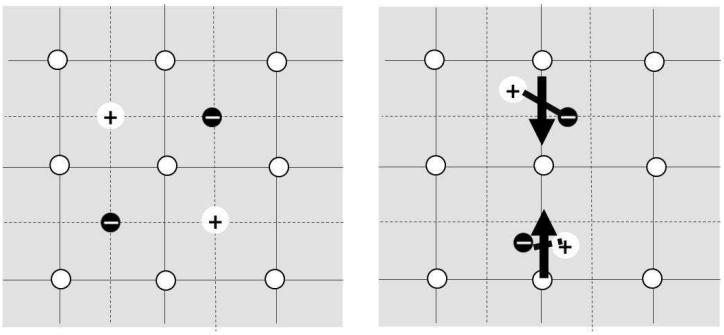

Figure 4.3: *Complex cases for the position patterns of SP pairs and the direct compensators for the adjoining SPs pairs: (a) SPs are distributed in discrete values, (b) SPs are distributed by using USP technique; in (b) the thick dashed line denotes the branch cut that connects two SPs of opposite sign and also shows the direct compensator positions are denoted by thick arrows.*

the accuracy of the unwrapped phase will be improved, as will be discussed in section 4.5.

4.4 Phase unwrapping by rotational and direct compensators algorithm

The proposed method (RC+DC) is based on coupling the RC and the DC to compute the compensators depending on the converging distance of SPs. In other words, it uses DC for computing the compensators for the pairs of adjoining SPs, and uses RC to compute the compensators for the other pairs. To explain that, it is assumed two new parameters $adj^{+}(i)$ and $adj^{-}(i)$, which are called adjoining parameters of the segment that is a member of the closed path of the adjoining SPs pair. The $adj^{+}(i)$ and $adj^{-}(i)$ denote the positive and negative SP numbers which belong to the adjoining pair, respectively, where i represents the segment number. It means when the segment i is a joint between the loop of the positive SP and that of the negative SP of the adjoining pair, these parameters have values; otherwise, they are undefined. Considering another parameter m_j^i, this parameter is defined as $m_j^i = 1$, when $adj^{+}(i)$ or $adj^{-}(i)$ has a value of j; otherwise $m_j^i = 0$. It is like Kroneckor's delta function as follows:

$$m_j^i = \delta_j^{adj^{+}(i)} + \delta_j^{adj^{-}(i)}. \tag{4.7}$$

Therefore, the total compensators can be estimated as follows:

$$C^i = \sum_{j=1}^{N_s} \overline{m_j^i}^R C_j^i + \sum_{j=1}^{N_s} m_j^{i\,D} C_j^i, \tag{4.8}$$

where $\overline{m_j^i} = 1 - m_j^i$. When $\overline{m_j^i}$ equals 1, i.e., the SP j does not belong to the adjoining pair, this represents the case of using RC to compute the compensator for the segment number i of the j-th SP. It should be noted that the times of $m_j^i \neq 0$ in the second summation is once for all i for each j related to the adjoining SPs pairs. By adding the compensator, C^i, to the wrapped phase differences according to Eq. (4.4), phase jumps were found due to the existence of SPs are canceled, therefore, the unwrapped phase can be retrieved successively.

The steps of the proposed algorithm (RC+DC) can be summarized as follows:

1. Calculate SPs in the wrapped phase map by the summation of the phase gradients of a 2×2 closed loop path. The positions of SPs are determined by USP technique.

2. Appending VSPs to the monopole SPs outside the measurement area, then analyze the SP pairs which consist of two real SPs laid inside the measurement area, or consist of one real SP and one VSP appended outside the measurement area. After that, define the adjoining SPs pairs.

3. For each segment i, the parameter m_j^i for every SP j is evaluated. If $m_j^i = 1$; i.e., a pair of SPs is an adjoining pair, a DC will be added, according to Eq. (4.6). Otherwise, RC will be computed using Eq. (4.2).

4. After that the total compensator for each segment through the whole phase map will be computed according to Eq. (4.8).

5. Finally, the unwrapped phase data can be retrieved by adding the compensators to the wrapped phase differences by using Eq. (4.4).

This description of direct compensation for the pairs of adjoining SPs makes the proposed algorithm simple and easy to implement. It provides a fast and efficient way to unwrap the phase map than the RC method does. The proposed RC+DC method improves the accuracy of

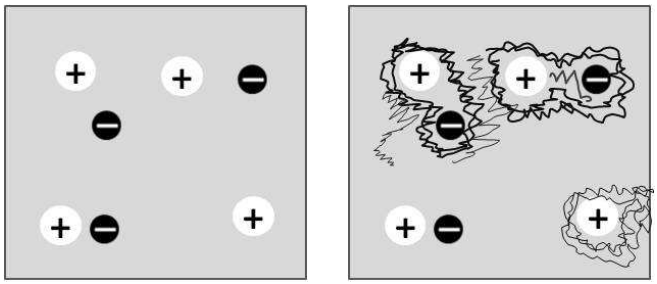

(a) (b)

Figure 4.4: *Spreading of errors in regular regions due to the proposed method (RC+DC) handling way for the singularity regions in the phase map: (a) SPs distribution map, (b) phase errors appear in regular regions.*

the RC method of confining the phase errors produce due to singularity effect of the adjoining SPs dipole pairs, which are shown in Fig. 3.3(b), by reducing the phase errors to zero by using the DC technique, as shown in Fig. 4.4(b). Figure 4.4 shows an example of phase errors spreading on the whole measured domain includes the regular regions produced when using the proposed method (RC+DC) to cancel the effect of singularity regions, which their distribution is shown in Fig. 4.4(a). However, the proposed algorithm still has phase errors due to the using of RC technique for nonadjoing SP pairs. In the following section, the performance and applicability of the proposed algorithm is examined.

4.5 Results and discussion

To evaluate the performance of the proposed algorithm (RC+DC), both simulated and real wrapped phase maps have been used.

4.5.1 Computer simulation results

In order to demonstrate the applicability of the proposed RC+DC method, a simulated noisy phase map with constant gradient is generated. This phase data has the image size 100×100 pixel^2, the gradient is $(0.1, -0.1)$ cycle/pixel, and the noise has a normal distribution with 0.15 cycle standard deviation. The original and wrapped phase data are shown in Fig. 4.5(a) and Fig. 4.5(b), respectively. In addition, Fig. 4.5 presents the distribution patterns of SP pairs

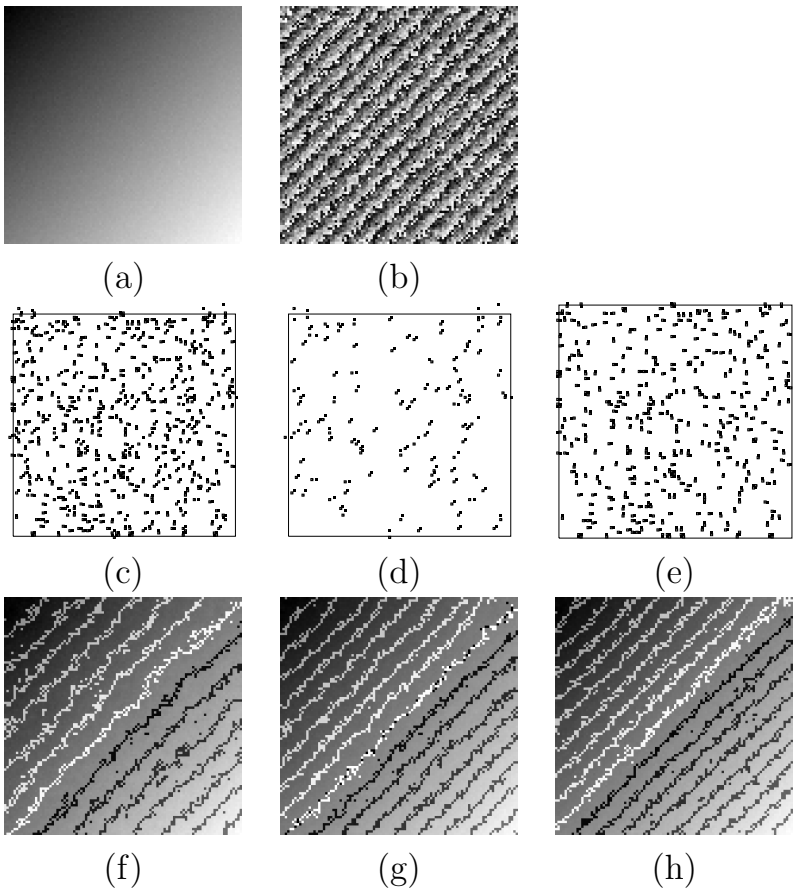

Figure 4.5: *A comparison of the unwrapped phase results for simulated phase data has noise with $\sigma = 0.15$ cycle: (a) the original phase data, (b) the wrapped data, (c) the positions of all SP pairs, (d) the positions of the pairs of non-adjoining SPs, (e) the positions of the pairs of adjoining SPs, (f) unwrapped result by LS-DCT, (g) unwrapped result by RC, and (h) unwrapped result by RC+DC. In (a), (b), and (f)-(h), the phase increases with the increases of brightness. In (f)-(h), contour lines of the phase with the interval of one cycle are also shown.*

for real and virtual SPs to show the position of SP pairs in the phase map. In Fig. 4.5(c), all SP pair positions are presented, while, in Fig. 4.5(d) and Fig. 4.5(e), the positions of the pairs of non-adjoining and adjoining SPs are shown, respectively. This indicates that most of SP pairs in the phase map are adjoining pairs, therefore, the use of DC will have obvious effect on the unwrapping process. Hence, the accuracy of the unwrapped phase will be improved and the computation time will be reduced as shown later. The unwrapped phase results obtained by the LS-DCT method [25], RC method [46] and the proposed RC+DC algorithm are shown through Fig. 4.5(f) to Fig. 4.5(h) with contour lines. To evaluate the characteristics of the phase

Algorithm	Gradient ($\nabla\tilde{\phi}$) [cycle/pixel]	$\Delta\left(\nabla\tilde{\phi}\right)$ [%]	σ [cycle/pixel]
Original	(0.1000 , –0.1000)	(— , —)	0.149
LS-DCT	(0.0742 , –0.0731)	(–25.8 , –27.0)	0.179
RC	(0.0912 , –0.0896)	(–8.7 , –10.4)	0.168
RC+DC	(0.0956 , –0.0951)	(–4.4 , –4.9)	0.168

Table 4.1: *A comparison of the accuracy for the simulation data, shown in Fig. 4.5.*

unwrapping methods, we can count the number of contour lines in the unwrapped results and compare them with the number of stripes in the wrapped data, shown in Fig. 4.5(b). From the comparison, we can find that the number of lines in the unwrapped results is less than that in the wrapped phase data. The wrapped phase data has 20 lines, the unwrapped result of LS-DCT method has 14 lines, the unwrapped result of RC algorithm has 17 lines, and the proposed algorithm's result has 18 lines. The unwrapped result of the proposed RC+DC algorithm has the nearest number of lines as wrapped data, which shows the highest accuracy.

Moreover, the accuracy of the proposed algorithm can be emphasized as shown in Table 4.1. This table shows a quantitative comparison of gradients for the original and unwrapped phase maps. In the table, the gradients are obtained by fitting them to a planar function, $\tilde{\phi}$, and the σ denotes the mean residual that is defined as a square root of a mean square residual from the fitted function, $\tilde{\phi}$. The σ of the original phase data is not equal to zero, because the original data contains noise with the given standard deviation. The errors of gradient, $\Delta\left(\nabla\tilde{\phi}\right)$ is estimated as the normalized difference between the unwrapped result and the original one, where the normalizing factor is the reciprocal of original one. From the table, it can be observed that the proposed algorithm, RC+DC, gives the smallest error in terms of $\Delta\left(\nabla\tilde{\phi}\right)$. This is due to the consideration of adjoining pair definition in computation of the compensators in the proposed algorithm. This result confirms that the proposed method (RC+DC) reduces the phase errors which exist mainly in the original RC method.

Figure 4.6 shows a comparison of required computational time of LS-DCT, RC and RC+DC methods for various image sizes; the horizontal axis N denotes one-dimensional area size in pixels. From the figure, the profiles of RC method and that of the proposed method show

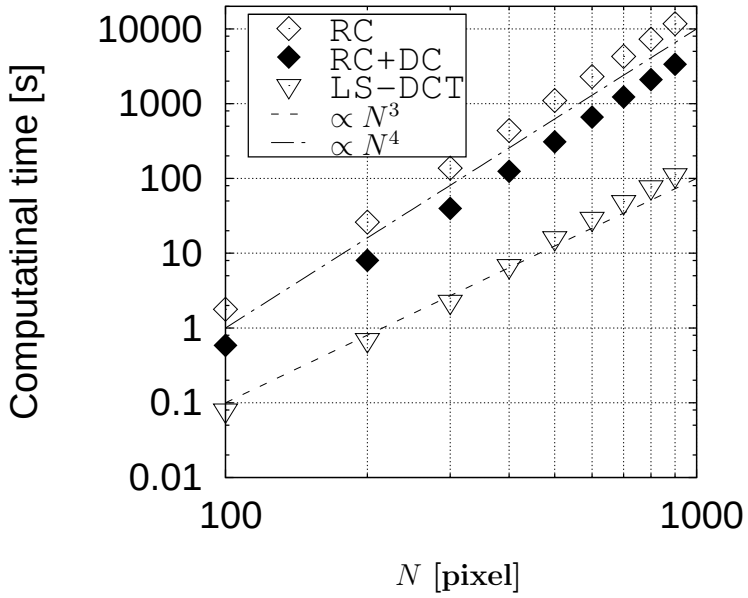

Figure 4.6: *Required computational time of each algorithm for various image sizes: The horizontal axis N denotes one-dimensional area size in pixels. "RC" shows the required time cost for RC method, "RC+DC" shows the required execution time for the proposed method, and "LS-DCT" shows the required time cost for LS-DCT method. The computational time is measured with a PC including an Intel Core 2 DUO CPU with 2.13 GHz clock in the single CPU operation mode.*

that the computation time is proportional to N^4. Furthermore, from Eq. (4.3), we can note that the time cost to compute the RC for all segments is proportional to the product of both the number of SPs and the number of the segments of path to be compensated. Since both are proportional to the area size ($\propto N^2$), the total evaluation time is proportional to N^4. In the RC+DC method, if the cost to compute the DC is adequately smaller than that of RC, the total cost might be similar to the case of RC algorithm, and it can be understood from Eq. (4.8). Conversely, when the number of the times of using DC computation is larger than that of RC in the proposed method, its execution time will be reduced compared to the RC method case. As a result, by coupling RC and DC computations, the execution time of the proposed method is almost one third of the execution time of the original RC method. In contrast, the computational time of LS-DCT method increases with N^3. In this computation, we use a matrix form of two-dimensional discrete FT [47]. Through the use of matrix form, the computational time of two-dimensional cosine transform needs only N^3 multiplications.

4.5.2 Experimental results

Experimental data obtained by interferometer

The proposed RC+DC algorithm has also been tested experimentally on two-dimensional wrapped phase map that resulted from the analysis of real fringe pattern taken from the experiment carried out by using Mach-Zehnder interferometer. The purpose of this experiment is to measure the phase shift in candle flames. The phase data has image size 256×170 pixel^2 and 2532 SPs (1267 for positive SPs and 1265 for negative SPs). The wrapped phase data and its corresponding SPs distribution map are shown in Fig. 4.7(a) and Fig. 4.7(b), respectively. Moreover, the unwrapped results, which have contour lines, obtained by RC method and the proposed RC+DC algorithm are given in Fig. 4.7(c) and Fig. 4.7(d), respectively. By comparing the number of stripe lines in the wrapped phase data and the number of contour lines in the unwrapped results from the mid-point on the base line of each figure, it can be observed that the wrapped data has 10 lines, the unwrapped result of RC algorithm has 8 lines and the proposed algorithm's result has 9 lines. The unwrapped results in both methods are underestimated, however, the underestimation in the proposed algorithm (RC+DC) is smaller than that in the RC method. This implies that the RC+DC algorithm succeed to reduce the phase errors produced by the original RC method.

The execution time of the proposed RC+DC algorithm varies depending on the number of SPs, data size and the ratio of the adjoining SPs. Table 4.2 presents the execution time for simulated and real phase maps discussed above for the RC method and the proposed RC+DC algorithm. The table shows the name, the size, the SPs ratio and the adjoining SPs ratio of each phase data. For noisy phase map, the SPs ratio, which is related to the data size, is around 9.1% and the adjoining SPs ratio is 80.9%. In this case, it was found that the overhead for each algorithm is the same. However, it is large enough compared to the execution time to compute the compensators for the RC+DC algorithm, i.e., T_{ovrh} is almost 0.7 times T_{comp}, hence, the saving time cost ratio of the proposed algorithm is reduced from 77.6% (saving time in compensators computation) to 67.2% (total saving time computation). On the other hand, flame data has SPs ratio of approximately 5.8% and the adjoining SPs ratio is around 60.4%. In this case, the overhead for the proposed algorithm (RC+DC) is relatively small compared to the execution time to compute the compensators, i.e., T_{ovrh} is almost 0.14 times

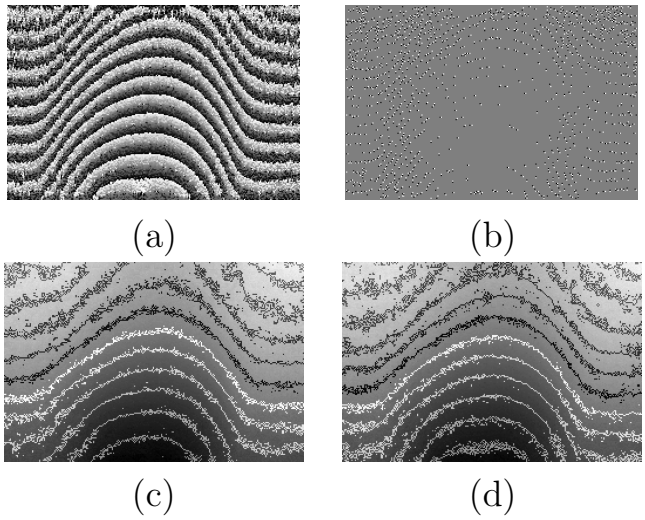

Figure 4.7: *Unwrapped phase result of experimental data for candle flame: (a) the wrapped data, (b) SPs distribution map, (positive and negative SPs are represented by white and black dots, respectively); (c) the unwrapped result of RC algorithm, (d) the unwrapped result of RC+DC,*

T_{comp}, so that the saving time cost ratio of the proposed RC+DC algorithm is reduce from 58.6% (saving time in compensators computation) to 55.5% (total saving time computation); however, the amount in reduction is not like noisy phase case. In other words, the saving time ratio to compute compensators is almost same to the adjoining SPs ratio. Therefore, the time to compute the DC is very small, so it is neglected and the saving time ratio to compute compensators is governed only by the RC computation.

From Table 4.2, it can be concluded that the execution time to search and analyze SPs is the same for the two examined algorithms. However, the execution time to compute the compensators in the RC+DC algorithm is reduced compared to that one of the original RC method. This reduction in the required computation time of the proposed algorithm is due to the direct calculation of the compensators for the adjoining SPs pairs.

Unwrapped results of phase extraction methods for object information obtained from interferograms

In the holographic measurement system, two fringe patterns should be measured to produce information of an object by using a similar setup of the interferometric experiment shown in

Data name	Data size: N_{all}	SPs ratio: N_s/N_{all} [%]	Adjoining SPs ratio: N_a/N_s [%]	RC T_{total} [s] T_{ovrh} [s] T_{comp} [s]	(RC+DC) T_{total} [s] T_{ovrh} [s] T_{comp} [s]	Saving time ratio [%]
Noisy phase	100x100	9.1	80.9	1.781 0.240 1.541	0.585 0.240 0.345	67.2 77.6
Flame	256x170	5.8	60.4	19.564 1.051 18.513	8.706 1.049 7.657	55.5 58.6

Table 4.2: *A comparison of the execution time cost between RC algorithm and the proposed RC+DC algorithm: The T_{ovrh} presents the required execution time for overhead procedure to search and analyse SPs' distribution. The T_{comp} presents the required execution time to compute the Compensators. The T_{total} is the summation, $T_{total} = T_{ovrh} + T_{comp}$. N_s and N_a, denote the total number of SPs and the number of SPs that form adjoining pairs, respectively. "Saving time ratio" $= 1 - T_{(RC+DC)}/T_{RC}$; where T_{RC} and $T_{(RC+DC)}$, represent the total execution times for RC method and the proposed method, respectively.*

Fig. 2.1. Firstly, a fringe pattern was obtained in the existence of an object. This fringe is referred as an object fringe and it is a superposed result of the object light passing through the object upon the reference light. The other fringe pattern is measured for background, which is the result from the same system but there is no object. To compute the information about the object, it is needed to eliminate the background fringe from the measured data. There are two ways to extract the phase shift caused by the object from the measured data, and these methods depend on the timing of the background exclusion. Figure 4.8 explains schematic diagrams to compute the phase shift of an object from experimental data. The first method is the pre-rejection of background data by subtracting the unwrapped phase of background data obtained without the existence of the object from the wrapped phase data obtained with the existence of the object. Then the phase difference is unwrapped to get the unwrapped phase shift result, as shown in Fig. 4.8(a). Meanwhile, the other method that is post-rejection of background data is carried out, as illustrated in Fig. 4.8(b). In this way, the phase difference is computed by excluding the unwrapped background phase data from the unwrapped phase of the object.

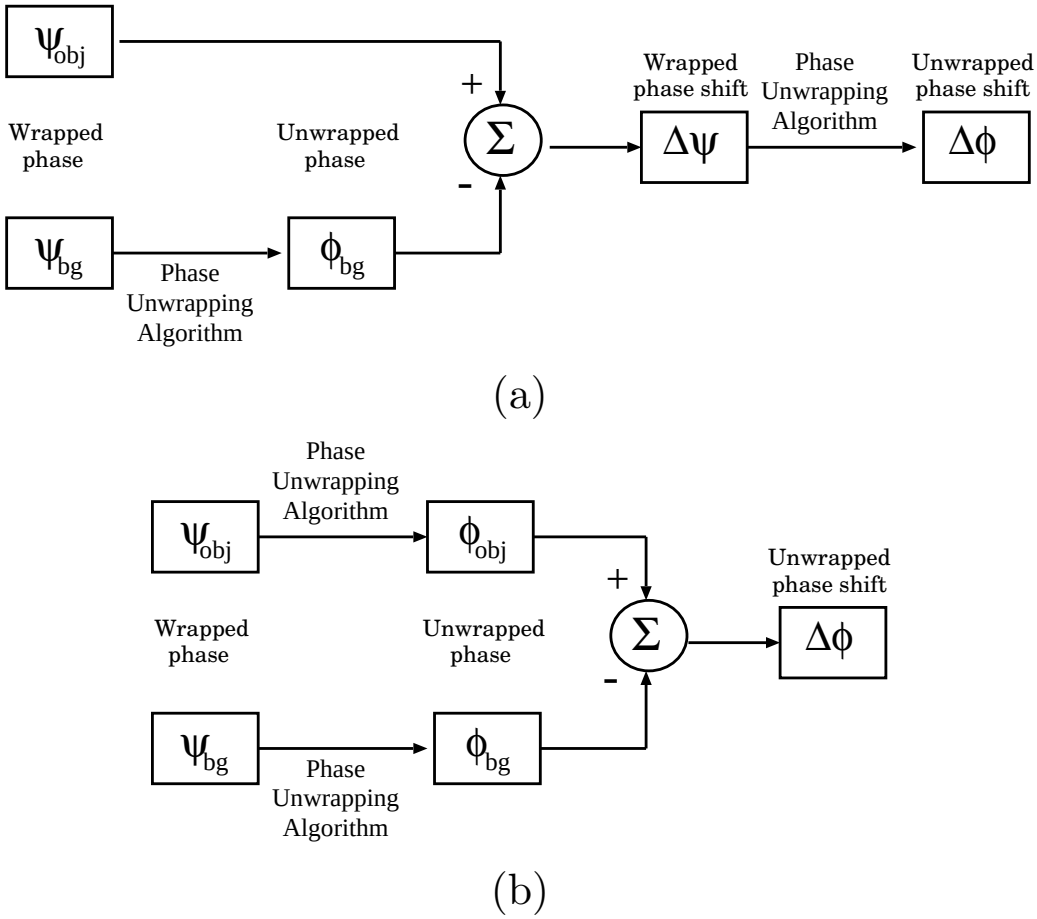

Figure 4.8: *The way of an object extraction from experimental data: (a) pre-rejection of background. (b) Post-rejection of background.*

Here, we examine the effect of these extraction ways on the unwrapped results of the phase shift caused by an object for interferograms. The object of this experiment is the temperature measurement of the heated gas (Air) around a candle flame through measuring the phase shift caused by the flame using Mach-Zehnder interferometer [46]. The fringe pattern obtained in existence of candle is referred as object fringe. In this measurement, the exposure time cannot be set long enough because the flame varies in time by convection flow around the flame itself. For this reason, the exposure time is set to 1ms. This setting cause two problems: firstly, the fringe has low S/N; secondly, we cannot apply the phase shift techniques [6, 8, 9] that use several fringes with different reference lights to obtain a wrapped phase. Spatial filtering for interferograms by using Fourier transform method [5–7] is hence applied to extract the phase information, as shown in Fig. 2.2. In addition, the background phase map in this experiment

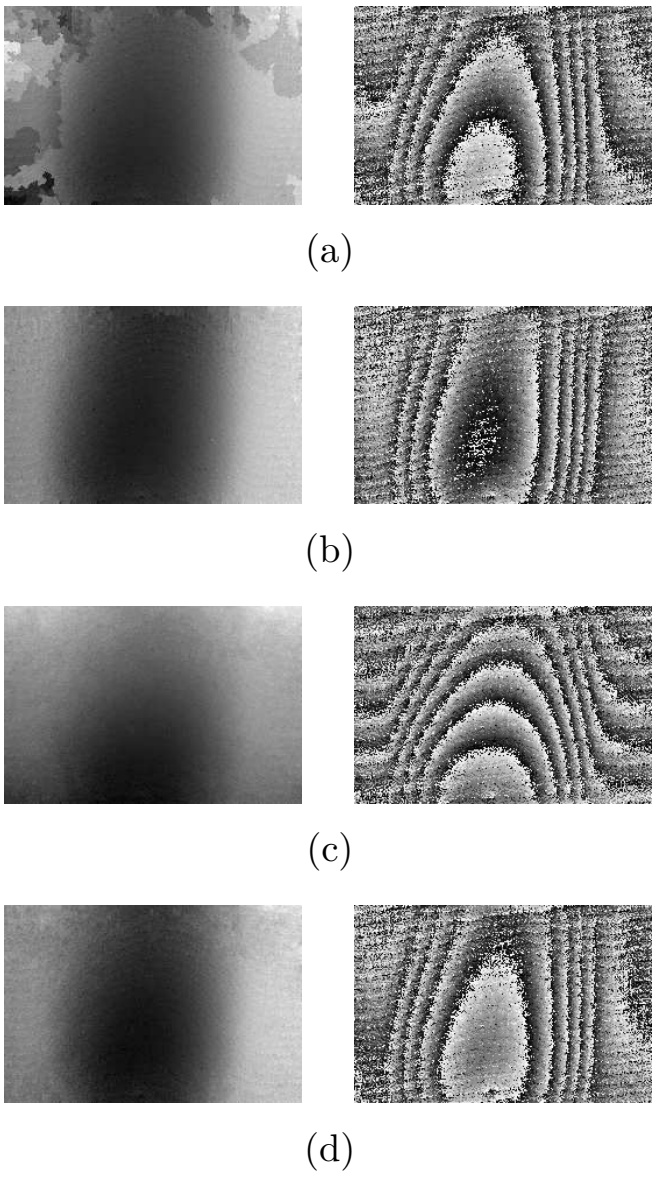

Figure 4.9: *A comparison of the accuracy of the examined phase unwrapping algorithms' results of candle flame for **pre-rejection** of background way to extract the object. The left column shows the unwrapped phase results. The right column shows the rewrapped phase results. (a) results obtained by Goldstein et al. method, (b) results obtained by Flynn method, (c) results obtained by LS-DCT method, (d) results obtained by RC+DC method.*

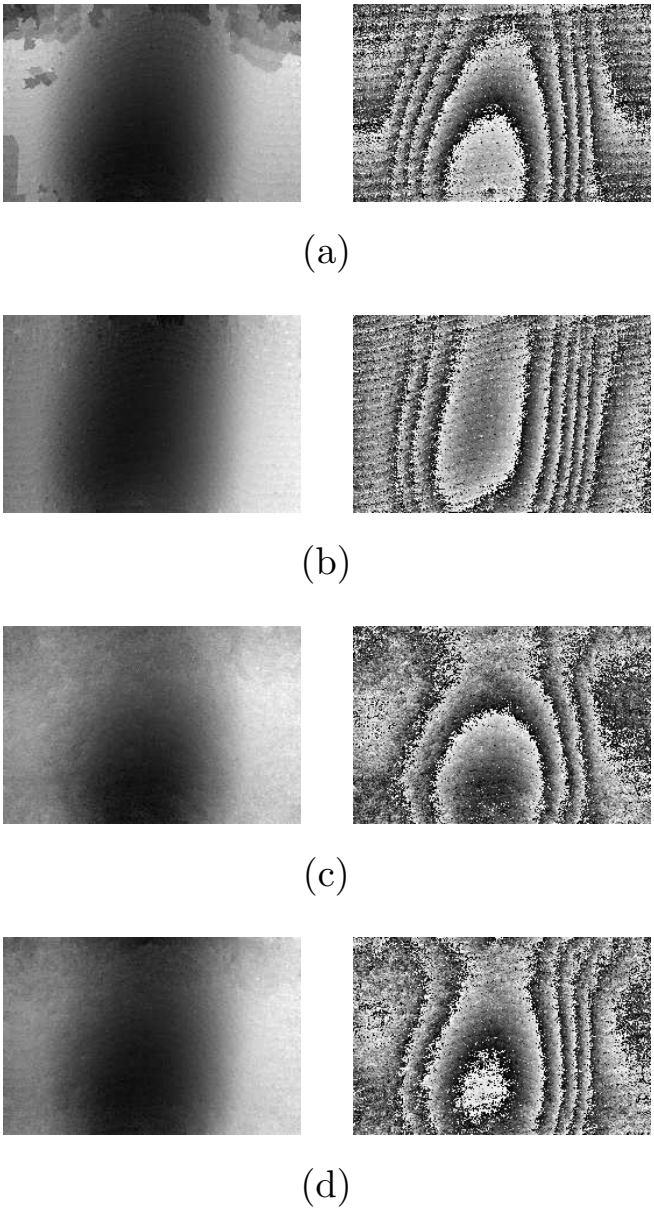

Figure 4.10: *A comparison of the accuracy of the examined phase unwrapping algorithms' results of candle flame for* ***post-rejection*** *of background way to extract the object. The left column shows the unwrapped phase results. The right column shows the rewrapped phase results. (a) results obtained by Goldstein et al. method, (b) results obtained by Flynn method, (c) results obtained by LS-DCT method, (d) results obtained by RC+DC method,*

is obtained by fitting to a planar function by using information from the wrapped phase data extracted from the object fringe pattern. This information is taken from the area where the object light did not pass through the flame in the wrapped data.

Figures 4.9 and 4.10 show the unwrapped and rewrapped results of the phase shift of the candle flame depending on the extracting ways of the object. These shown results are obtained by using the proposed (RC+DC) method and other three existing phase unwrapping methods, which are Goldstein et al.'s path-following method [11], Flynn's minimum weighted discontinuity algorithm [15], and LS-DCT method [25] to show their performance for such this kind of phase data. Figure 4.9 presents a comparison of the accuracy of the examined phase unwrapping algorithms' results of the candle flame for pre-rejection of the background way to extract the object. Meanwhile, Fig. 4.10 shows the compared results for the post-rejection way. From the figures, it can be found that the unwrapped result of the Goldstein et al. method causes phase jumps; however, the other three methods have no phase jumps. Although, there is no phase jump in the unwrapped results obtained by LS-DCT method for both ways (pre-rejection and post-rejection) of background, its rewrapped results produced by both ways are different, as shown in Figs. 4.9(c) and 4.10(c). This implies that the accuracy of LS-DCT method remains in doubt. On the other hand, the rewrapped phase results in both ways for object extraction, which are pre-rejection and post-rejection, are quite similar for either Flynn method or the RC+DC algorithm , as shown in Figs. 4.9 and 4.10. Therefore, it can be said that Goldstein et al. and LS-DCT methods provide inaccurate phase results. Meanwhile, Flynn method and the RC+DC algorithm produce accurate results. However, the unwrapped results of the examined algorithms are affected by the way of object extraction. It is understood that in the way of post-rejection for the background, Goldstein et al., Flynn and LS-DCT methods give better results than those results in the pre-rejection way. The reason is that the number of SPs from the wrapped phase data in post-rejection way, which is 2532 for the studied unwrapping algorithms, is smaller than its number of SPs in pre-rejection way, which is 3046 for Goldstein method, 3208 for Flynn algorithm and 2690 for LS-DCT method. In contrast, the unwrapped phase result obtained by the RC+DC method in the way of pre-rejection for the background is better than its unwrapped result obtained in the post-rejection way. This is due to that the ratio of adjoining pair of SPs for the wrapped phase data in pre-rejection way, which is 70.41%, is larger than its ratio of 60.54% in post-rejection way. This implies the

benefit of the RC+DC algorithm which uses DC to compensate the singularities of adjoining pair of SPs to reduce the unwrapping error.

In addition, the execution time required for each studied algorithm to obtain the unwrapped results is also evaluated. It is found that the highest time cost to produce the unwrapped results in the both ways of object extraction are for Flynn method, which are 736.60 sec in the pre-rejection way and 450.90 sec in the post-rejection way. In the meantime, the execution time of the RC+DC algorithm to obtain its unwrapped result for both ways of the object extraction showed better performance than Flynn method did, which are 8.84 sec in pre-rejection way and 8.85 sec in post-rejection way. Hence, it can be concluded from above discussion that the developed method (RC+DC) gives results with acceptable quality and with low computational time cost. Moreover, the best unwrapped phase result is the unwrapped result shown in Fig. 4.9(d), which obtained by the RC+DC method.

Experimental data obtained by FTP

A three-dimensional object surface is measured in our experiment; the object is a ping-pong ball with a diameter of roughly 40 mm. The measurement system consists of a digital projector and a CCD camera, and it conforms to the conventional cross-optical-axes geometry system, as shown in Fig. 2.3(a). The system parameters are $l_0 = 320$ mm and $d_0 = 110$ mm. The deformed grating image captured by the CCD camera and the wrapped phase image and its corresponding SP distribution map are shown in Fig. 4.11. The image size is 408×312 pixels. The wrapped phase obtained by filtering in Fourier space has 580 SPs, most of which are found in the background and around the boundary of the object, as shown in Fig. 4.11(c) as white and black pixels.

Figure 4.12 shows a comparison of the accuracy for Flynn's method [15] and the proposed RC+DC algorithm in regard to the unwrapped phase shift results of the object, the rewrapped phase results and the profile of the object's height. Figures 4.12(a) and 4.12(b) show the unwrapped results of the object's phase shift for Flynn's method and the proposed algorithm, respectively. Figures 4.12(c) and 4.12(d) are the rewrapped results of the unwrapped results shown in Figs. 4.12(a) and 4.12(b), respectively. Comparing these figures we can find

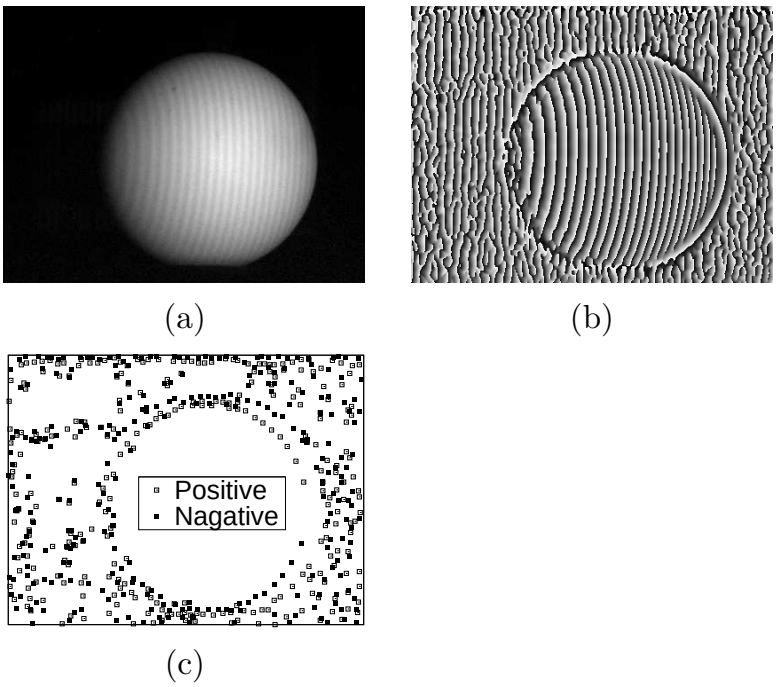

Figure 4.11: *Experimental measured data: (a) deformed grating image, (b) wrapped phase image, and (c) map of distribution of SPs.*

that there are phase distortions in the background and on the edge of the object in the unwrapped result of Flynn's method (Figs. 4.12(a) and 4.12(c)). It shows that Flynn's method cannot remove the effect of singularity in these regions. In contrast, the proposed algorithm (Figs. 4.12(b) and 4.12(d)) can compensate the singularity of SPs located around the object and in the background. Moreover, Figs. 4.12(e) and 4.12(f) show the comparison of cross-sectional profiles of the object height for three different y-positions, where $y = 0$ mm is corresponding the cross-section going through the center of the ball. In the background regions (the left-hand side of 20 mm or the right-hand side of 55 mm), the large fluctuation can be clearly observed on Flynn's result in Fig. 4.12(e). The height in these regions should be zero, as shown for the result of the proposed algorithm in the left side in Fig. 4.12(f). In the background area on the right side of both figures the height is not zero. The reason for this is the illuminated light by the projector. Since the light is illuminated as an oblique incidence with angle θ, a part of the right side of the object is not illuminated. Therefore, the right side of the object is shadowed and the height of the boundary of the shaded area is not zero. In addition, the execution time required for Flynn algorithm to obtain the unwrapped result, which is

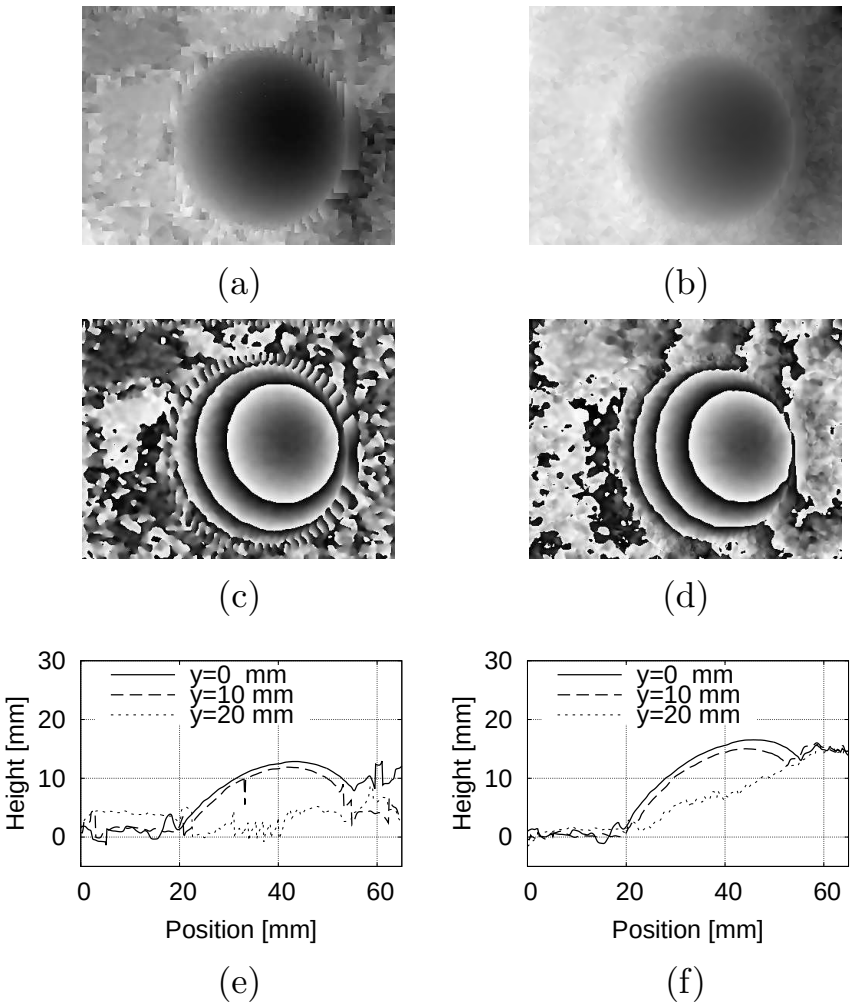

Figure 4.12: *Comparison of the accuracy of the examined phase unwrapping algorithms' results for the measured data: the first row shows the unwrapped phase shift of the object, the second row shows the rewrapped phase shift of the object, the third row shows the cross-sectional profile of the object's height. (a), (c), and (e) show the results of Flynn's method. (b), (d), and (f) show the results of RC+DC algorithm.*

7277.26 sec, is too long compared with the execution time of the proposed algorithm to obtain its unwrapped result, which is 14.83 sec. Hence, it can be concluded from above discussion that the proposed method gives results with acceptable quality and with short computation time.

4.6 Conclusions

Phase unwrapping for noisy data by using RC had good performance among the other existing methods. However, the RC method has drawbacks of computational time requirements and an undesirable phase distortion in the regular regions. To overcome these drawbacks, we propose a new method based on coupling the existing RC and the DC. The DC compensates the singularity of the pair of adjoining SPs connected by a branch cut with the length which is shorter than one pixel. The compensator along the segment that crosses the branch cut is just 2π. For the SPs that are not members of adjoining pairs, RC is applied as a compensator. The proposed algorithm (RC+DC) is tested on both computer-simulated and experimental noisy phase data. The results show that the RC+DC algorithm has a smaller computational time requirement compared to the original RC method.

Furthermore, the performances of the developed phase unwrapping algorithm (RC+DC) and of other existing phase unwrapping methods for two examples of phase measurement applications, which are interferometric and Fourier transform profilometry measurements are compared. In addition, the methods to extract phase information about the object from interferogram maps are also investigated. The results show that the proposed algorithm (RC+DC) gives results with acceptable quality and with low computational time cost compared to the existing methods.

CHAPTER 5

LOCALIZED COMPENSATOR BASED ON ROTATIONAL AND DIVERGENCE OPERATORS FOR UNWRAPPING

- Introduction
- Phase unwrapping compensation methods
- Proposed localized compensator method based on rotational and divergence operators (LC.rot+div)
- Results and discussion
- Conclusions

Chapter 5
Localized compensator based on rotational and divergence operators for unwrapping

5.1 Introduction

Phase unwrapping for a noisy image suffers from many SPs. Methods based on spreading singularity are useful for noisy phase images to regularize the singularity. However, these methods have a drawback of distorting phase distribution in regular areas those contain no SPs. When the SPs are confined in some local areas, the regular regions are not distorted. In terms of accuracy, the method using localized compensator [48] is superior to the other methods. However, this method has major disadvantages of memory shortage and computational cost since it requires high time cost to produce its unwrapped results. In this chapter, an effective and fast phase unwrapping algorithm is presented. The proposed algorithm solves the problem of memory shortage and reduce the computational time requirements of the localized compensator method to a minimum, and together with that it keep the same level of results accuracy.

5.2 Phase unwrapping compensation methods

In the wrapped phase data, SPs prevent straightforward unwrapping. Moreover, the existence of SPs causes the phase unwrapping process to be path-dependent. Therefore, many algorithms have been proposed based on compensating the phase singularities to cancel their effect. The idea of singularities compensation was proposed in the SSPU method [43] and in the methods using RC [46], RC+DC [49] or a localized compensator (LC) [48] techniques. However, these methods compensate the singularities in different ways. The SSPU method

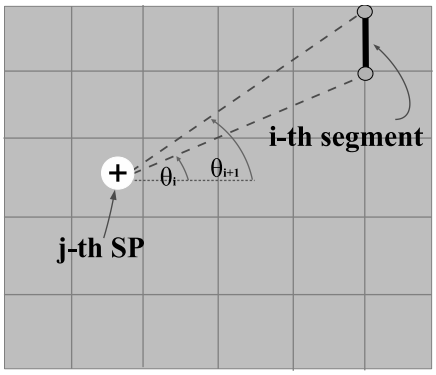

Figure 5.1: *Schematic of rotational compensator phase unwrapping method: the singularity of $j-th$ SP is canceled by computing the RC of $i-th$ segment using eq. (5.1).*

requires an iteration process to compute the compensators. The RC method can compute the compensators through superposing the effect of each SP by adding an integral of isotropic singular function along any loops. While, the RC+DC method is coupling the rotational and direct techniques to compute the compensators depending on the converging distance of SPs. On the other hand, the LC method regularizes the inconsistencies only in a local areas, which are clusters, around the SPs by integrating the solution of Poisson's equation for each cluster to compute the compensators.

The SSPU algorithm [43] is firstly defines SPs distribution in the phase map. Next, the compensators are not added only to the pixel values at the SPs but also those at around the SPs. Then, this method repeat the same process over the whole image. However, SSPU method spreads the singularities to the entire domain of the image and this is consider as disadvantage of SSPU method. Another disadvantage is found in this method, which is the requirement of large computational time to obtain a suitable result. When the maximum residue value after the spreading process is not negligible value, means very small, it is needed to repeat many times of processes. Further details regards SSPU method, are given in section 2.4.2 in chapter 2.

The RC method [46] uses local phase information to compensate the singularity parts of phase map caused by existence of SPs. This method can cancel the singularity of the j-th SP, by computing the RC of i-th segment, which is ${}^{R}\boldsymbol{c}_j^i$, in terms of its azimuthal angles as follows:

$$ {}^{R}\boldsymbol{c}_j^i \triangleq -m_j(\theta_{i+1,j} - \theta_{i,j}), \tag{5.1}$$

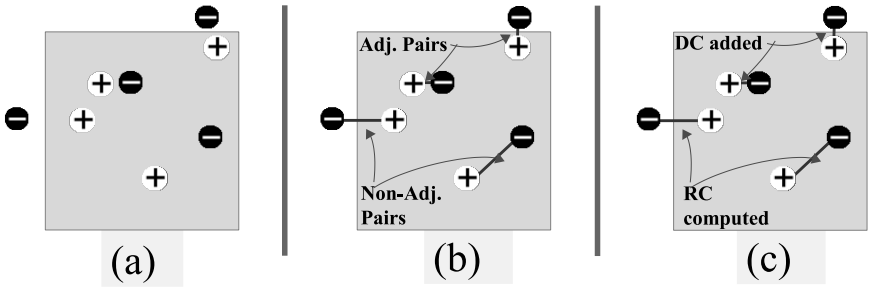

Figure 5.2: *Schematic of rotational and direct compensator phase unwrapping method: (a) defined SPs, (b) create SPs pairs and defined adjoining and nonadjoining pairs, (c) add DC for adjoining pairs and compute RC for nonadjoining pairs.*

where m_j denotes the residue of the j-th SP. Also, $\theta_{i,j}$ and $\theta_{i+1,j}$ represent the azimuthal angles of the beginning and the end points of the i-th segment, as shown in Fig. 5.1. However, the RC method has a drawback of undesired phase error because the RC should be applied to the regular region with no SPs as well as to the singular region. In addition, the RC method required high computational time cost when the measured phase data contains many SPs.

The RC+DC method [49] is based on coupling the RC and the DC techniques to compute the compensators depending on the SPs locations. Figure 5.2 illustrates the main steps in the RC+DC method. First, identifying SPs locations, then creating SPs pairs and defined adjoining and nonadjoining pairs. The RC+DC method uses DC as the compensators for the adjoining SP pairs, and uses RC to compute the compensators of nonadjoining pairs. The adjoining pair is a dipole consists of two SPs with opposite signs separated by one pixel horizontally or vertically. The RC+DC method is fast, however, its accuracy is not guaranteed. Its accuracy is depending on reducing the times of using the RC technique that increases the phase distortion in the unwrapped results.

The LC method [48] regularizes the inconsistencies in local areas, which are clusters, around the SPs by integrating the solution of Poisson's equation for each cluster to evaluate the compensators. In other words, firstly, LC method needs to determine cluster groups, then it computes the compensators depending on the solution of Poisson's equation for each cluster. In terms of accuracy, the LC method is superior to the other methods; despite this, the LC method has a major disadvantage of computational cost since this method requires long time cost to compute the compensators.

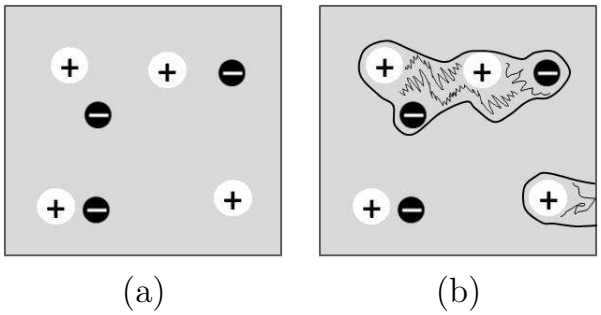

Figure 5.3: *Spreading of errors in regular regions due to the handling way of the LC method for the singularity regions in the phase map: (a) SPs distribution map, (b) phase errors appear in regular regions.*

The LC method has the same merit of the RC+DC method regards the phase errors spread due to the singularity effect of the adjoining SP dipole pairs on the regular regions that contains no SPs. Since the phase errors of these pairs by using RC+DC method is zero, as shown in Fig. 4.4(b). Figure 5.3 shows an example of phase errors spreading on the whole phase map includes the regular regions produced when uses the LC method to cancel the effect of singularity regions, which their distribution is shown in Fig. 5.3(a). The LC has no phase error during compensating the singularity effects of adjoining SP pairs, in addition, this method (LC) confines the phase error for other SPs in local regions which are cluster, as shown in Fig. 5.3(b).

5.3 Proposed localized compensator method based on rotational and divergence operators (LC.rot+div)

The LC unwrapping method confines the effect of inconsistencies due to existence of SPs in local areas, which are clusters, by integrating the solution of Poisson's equation for segments in each cluster to evaluate the compensators according to a certain mechanism. It uses boundary element method (BEM) [50] to get the compensator values. BEM produces large errors in the results when the singularity sources are position near to the segments which compensators are computed for them. Therefore, singular value decomposition (SVD) method is used to fix the errors produce by BEM step. We will mention to the original LC method by LC.bem+svd. A flowchart illustrates the two main steps of LC.bem+svd method is shown in Fig. 5.4.

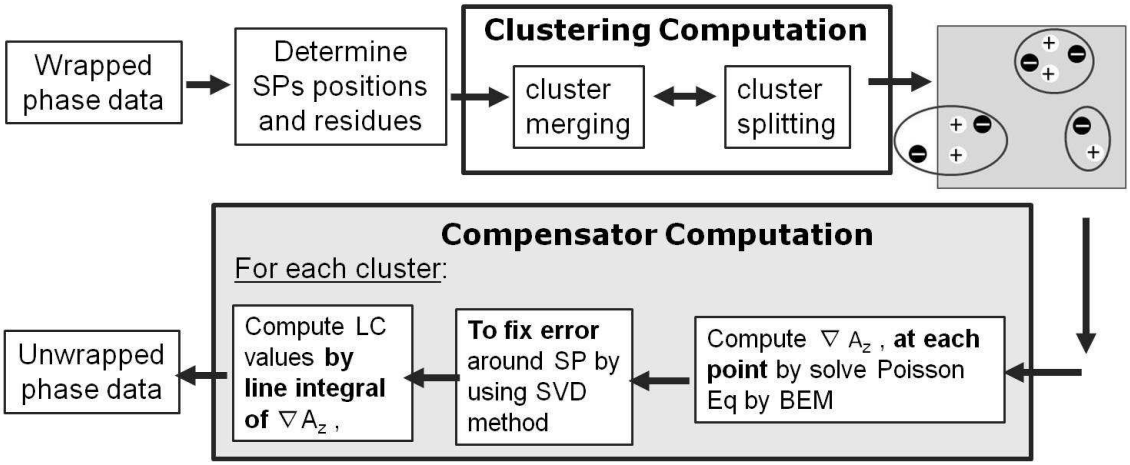

Figure 5.4: *A flowchart of the original LC method (LC.bem+svd) shows the two main steps for this method.*

In terms of accuracy, the LC.bem+svd method is superior to the other methods. Despite this, LC.bem+svd method has a major disadvantage of computational cost since this method requires long time cost to compute the compensator values and to reduce errors. Therefore, to overcome these drawbacks, we use a new way to produce the compensator values.

5.3.1 The principles of the Localized compensator technique

When a closed loop includes SP, the integral along the loop will have a value of $-2\pi m$, as shown in Eq (2.13), where m is S in the mentioned equation. Representing an integral of a segment i, which is a member of the loop comprising N segments, as $\boldsymbol{c}^i$, we can reduce Eq. (2.13) as in Eq. (4.1). This suggests that the singularity of Ψ^i is regularized by compensator $\boldsymbol{c}^i$ for each segment. In the case of an arbitrary closed path, C, since this path is considered as a boundary of the region that is connected with sub-regions of elementary loops, the integral of C is expressed as

$$\oint_C \sum_{i=1}^{M} \hat{\nabla}\Psi^i \, dl \; = 2\pi \sum_k m_k. \tag{5.2}$$

For example, when two adjacent loops have two SPs with opposite polarity shown in Fig. 5.5, the compensator value along internal segment which is common segment between the two loops is equal to the value of the phase jump which is one cycle (2π radian); meanwhile, the compensator values for the other segments which are the boundary segments for these loops

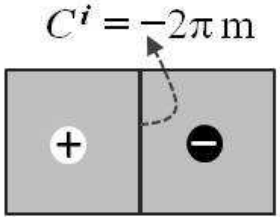

Figure 5.5: *Example of two adjacent loops have two SPs with opposite polarity, presenting the compensator value for the internal segment.*

are equal zero. By connecting Eqs. (4.1) and (5.2), we can obtain the following relation:

$$\oint_C \sum_{i=1}^{M} \boldsymbol{c}^i \, dl \; = -2\pi \sum_k m_k. \tag{5.3}$$

The last example give us two conditions required to compute the compensators for a specific domain. The first condition is that the number of positive and negative SPs must be equaled in the domain, means they must balance each other out in the localized domain, which is called source condition, as

$$\sum_k m_k = 0. \tag{5.4}$$

It means that the phase map is divided to regions, which are called clusters, depending on a certain mechanism. Each cluster must have the same number of positive and negative SPs. The second condition is that the compensator must vanish on every boundary segment, and this is called boundary condition. If the wrapped phase difference of two adjoining nodes ($\boldsymbol{r}$ and $\boldsymbol{r}' = \boldsymbol{r} + \hat{\boldsymbol{s}}\,\Delta l$) is defined as vector quantity ($\boldsymbol{g} \cdot \hat{\boldsymbol{s}}$), it is transformed as follows:

$$\begin{aligned} \boldsymbol{g} \cdot \hat{\boldsymbol{s}} &\triangleq \frac{1}{\Delta l} W\{\Delta\phi_w\} \\ &= \frac{1}{\Delta l}\left(\Delta\phi - \mathrm{Int}\left[\frac{\Delta\phi}{2\pi}\right] 2\pi\right) \\ &= \nabla\phi \cdot \hat{\boldsymbol{s}} - \mathrm{Int}\left[\frac{\Delta\phi}{2\pi}\right] \frac{2\pi}{\Delta l}, \end{aligned} \tag{5.5}$$

where both $\boldsymbol{g}$ and $\nabla\phi$ are constant on the segment between $\boldsymbol{r}$ and $\boldsymbol{r}'$, and $\hat{\boldsymbol{s}}$ is the unit vector of direction $\boldsymbol{r}' - \boldsymbol{r}$.

Therefore, Eqs. (4.1), (5.2) and (5.3) can be rewritten as follows:

$$\oint_C (\boldsymbol{g} + \boldsymbol{c}) \cdot \hat{\boldsymbol{s}}\, dl = 0, \tag{5.6}$$

$$\oint_C \boldsymbol{g} \cdot \hat{\boldsymbol{s}}\, dl = 2\pi \sum_k m_k. \tag{5.7}$$

$$\oint_C \boldsymbol{c} \cdot \hat{\boldsymbol{s}}\, dl = -2\pi \sum_k m_k. \tag{5.8}$$

Since the unwrapped phase ϕ must be a scalar field, the difference vector of wrapped phase $\boldsymbol{g}$ in Eq. (5.5) satisfies the following equation using the divergence free vector function, $\boldsymbol{A}$:

$$\boldsymbol{g} = \nabla\phi + \nabla \times \boldsymbol{A}, \tag{5.9}$$

$$\nabla \cdot \boldsymbol{A} = 0. \tag{5.10}$$

By applying Stokes' theorem to an integral of the rotation of Eq. (5.9) over a domain enclosed by a path C, and by comparing the result with Eq. (5.7), the following relations can be obtained:

$$\boldsymbol{c} \triangleq -\nabla \times \boldsymbol{A}, \tag{5.11}$$

Once the compensator, $\boldsymbol{c}$ that satisfies Eq. (5.8) is found, phase unwrapping can be successively carried out using the following integration or accumulation of compensators:

$$\phi(\boldsymbol{r}) = \phi(\boldsymbol{r}_0) + \int_{\boldsymbol{r}_0}^{\boldsymbol{r}} \boldsymbol{g} \cdot \hat{\boldsymbol{s}}\, dl + \int_{\boldsymbol{r}_0}^{\boldsymbol{r}} \boldsymbol{c} \cdot \hat{\boldsymbol{s}}\, dl. \tag{5.12}$$

The integrand, $\boldsymbol{c} \cdot \hat{\boldsymbol{s}}$, of the last term in Eq. (5.12) can be transformed as follows with using of Eq. (5.11):

$$\begin{aligned}
\boldsymbol{c} \cdot \hat{\boldsymbol{s}} &= -(\nabla \times \boldsymbol{A}) \cdot \hat{\boldsymbol{s}} \\
&= -(\nabla \times \boldsymbol{A}) \cdot (\hat{\boldsymbol{z}} \times \hat{\boldsymbol{n}}) \\
&= \hat{\boldsymbol{n}} \cdot (-\nabla \times \boldsymbol{A} \times \hat{\boldsymbol{z}}) \\
&= \hat{\boldsymbol{n}} \cdot \{-(\hat{\boldsymbol{z}} \cdot \boldsymbol{A})\nabla + (\hat{\boldsymbol{z}} \cdot \nabla)\boldsymbol{A}\} \\
&= \hat{\boldsymbol{n}} \cdot \nabla A_z,
\end{aligned} \tag{5.13}$$

where $\hat{\boldsymbol{n}}$ is the outward normal unit vector of the boundary, $\hat{\boldsymbol{z}}$ is the perpendicular unit vector to the domain surface, the directions of these unit vectors satisfy $\hat{\boldsymbol{s}} = \hat{\boldsymbol{z}} \times \hat{\boldsymbol{n}}$; and $A_z = \boldsymbol{A} \cdot \hat{\boldsymbol{z}}$, $\hat{\boldsymbol{z}} \cdot \nabla \equiv 0$ is applied for two-dimensional problem. The quantity $\hat{\boldsymbol{n}} \cdot \nabla A_z$ presents a normal flux density of ∇A_z. Therefore, the boundary condition for the localized compensator technique is reduced to Neumann condition as:

$$\hat{\boldsymbol{n}} \cdot \nabla A_z = 0. \tag{5.14}$$

In the meantime, the closed integral along any path C, as in Eq. (5.8), can be transformed by using Stokes' theorem and Eqs. (5.11) and (5.10) as follows:

$$\begin{aligned} \oint_C \boldsymbol{c} \cdot \hat{\boldsymbol{s}}\, dl &= \int_S \nabla \times (-\nabla \times \boldsymbol{A}) \cdot \hat{\boldsymbol{e_z}}\, dS \\ &= \int_S \nabla^2 A_z\, dS = -2\pi \sum_k m_k. \end{aligned} \tag{5.15}$$

In addition, a residue m_k at the point $\boldsymbol{r}_k$ can be expressed by Dirac's delta function as:

$$m_k = \int_S m_k\, \delta(\boldsymbol{r} - \boldsymbol{r}_k)\, dS. \tag{5.16}$$

Therefore, Poisson's equation can be obtained for A_z from Eqs. (5.15) and (5.16), as:

$$\nabla^2 A_z = -2\pi \sum_k m_k\, \delta(\boldsymbol{r} - \boldsymbol{r}_k). \tag{5.17}$$

The solution of Poisson's equation shown in Eq. (5.17), A_z, expresses the flux density that describes the spreading of singularities, which are shown in the right-hand side of Eq. (5.17). The solution found in Eq. (5.17) is calculated with the boundary condition given in Eq. (5.14) for the domain which is satisfying Eq. (5.4). To solve, A_z any filed solver can be applied. In the orignal LC method (LC.bem+svd), BEM is used as a basic solver. However, when the point to estimate the field is located near the source points, which are SPs, the BEM has a large computational error. To reduce this error, SVD is used to find a minimum norm solution. Further details are found in section 5.3.3.

Once the solution is obtained, compensator along every segment placed in the domain is computed as an integral of the flux density by Eq. (5.13). However, the outward normal vector $\hat{\boldsymbol{n}}$ cannot be defined at the segment in the domain, since the boundary loop is not defined. In

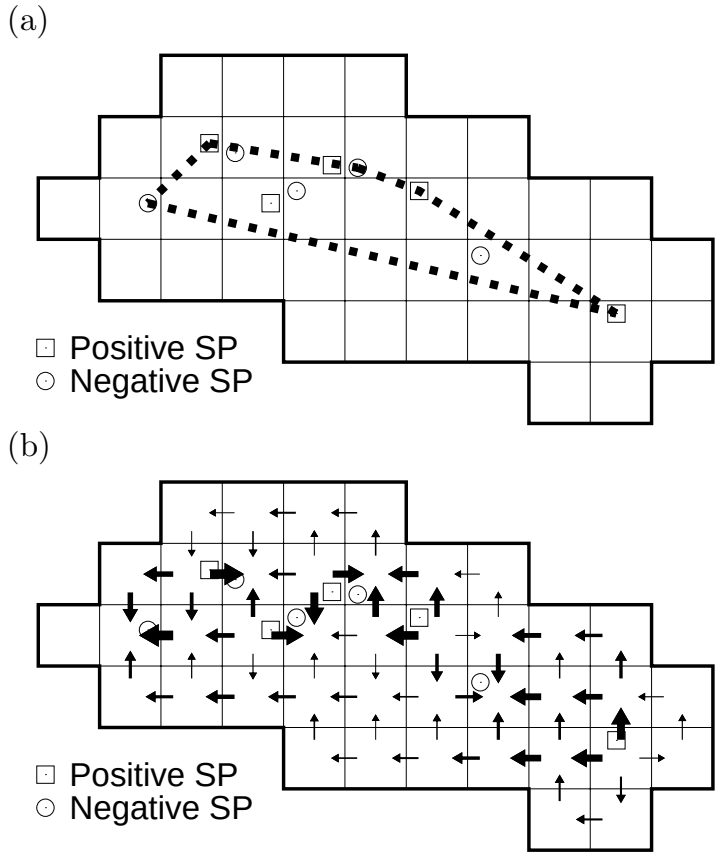

Figure 5.6: *Definition of local domain and flux density around SPs: (a) local domain including SPs, (b) flux distribution in the local domain. Outmost closed thick line is a boundary of the local domain, and the grids are segments of elementary loops. The dashed line in (a) represents concave polygon that contains all SPs. The arrows in (b) are the flux density of which line width expresses the magnitude.*

this case, the normal vector can be replaced by $\hat{\boldsymbol{s}} \times \hat{\boldsymbol{z}}$ where $\hat{\boldsymbol{s}}$ indicates the direction of the segment. As a result, the integral of the compensator is rewritten as below:

$$\int_{\boldsymbol{r}_0}^{\boldsymbol{r}} \boldsymbol{c} \cdot \hat{\boldsymbol{s}}\, dl = \int_{\boldsymbol{r}_0}^{\boldsymbol{r}} \hat{\boldsymbol{s}} \times \hat{\boldsymbol{z}} \cdot \nabla A_z\, dl. \tag{5.18}$$

By using this relation, the wrapped phase can be unwrapped by Eq. (5.12).

Figure 5.6 shows an example of a determined local region and an evaluated flux density distribution. From the result in Fig. 5.6(b), it can be said that a large flux density distribution was found around SPs while it was comparatively small near the boundary.

5.3.2 Clustering

The clustering process generates zero-charged groups which are named 'clusters', and they satisfy Eq. (5.4). Gutmann and Weber proposed a clustering algorithm to search branch cut efficiently using a simulated annealing method [17]. Their clustering algorithm may be applicable to determine the local domain; however, it needs experimental parameters. In the LC method, a new clustering algorithm is proposed without a use of experimental parameters. As shown in section 5.3.1, although the phase compensators defined in a cluster's region can regularize the singularity, it distorts the regular region. Therefore, the region of the cluster needs to be as small as possible. If the measurement area is infinitely wide, all the zero-charged clusters can be found because the total numbers of them are always same. However, the actual area is finite. If the total numbers of positive and negative SPs in the area are different, the solution could not be found. Even when the total numbers are the same, a SP to be coupled to the other SP may be placed near the border of the area, but it is outside the area. In this case, SPs in the area may become larger sized clusters. To avoid this problem, virtual SPs are introduced to be located outside the finite area [46]. The clustering procedure to find small sized clusters consists of two stages: cluster merging, and cluster splitting, as illustrated in the flowchart of the LC.bem+svd method shown in Fig. 5.4. The cluster merging process usually increases the size of cluster, while the cluster splitting which reduces the size. The main concerning in the proposed algorithm is regard the compensator computations step, while the proposed algorithm will use the same computations for the cluster step. The complete details about the cluster method is found in [48].

5.3.3 BEM to solve Poisson's equation

For each cluster determined in the LC method, the domain to apply the local compensator is defined as one pixel (elementary loop) width wider area than the region of the convex shaped area that contains all SPs in the balanced cluster. The boundary of the domain is set on the outermost segments; an example was shown in Fig. 5.6(a). As shown in Eq. (5.13), the compensator for phase unwrapping is equivalent to the flux density of ∇A_z when A_z satisfies a Poisson's equation shown in Eq. (5.17) with the boundary condition given by the Neumann condition with zero-flux density as presented in Eq. (5.14).

The original LC method (LC.bem+svd) uses BEM [50] as a basic solver to solve A_z. In the BEM, the unknown boundary values at the boundary nodes (A_z) are solved as a set of discretized boundary integral equations for the all boundary nodes shown in Fig. 5.7. After solving this set of equations, all boundary values, A_z and $(\nabla A_z \cdot \hat{\boldsymbol{n}})$, are determined. Internal flux density at arbitrary points are evaluated as hyper-singular integrals, e.g. [51–53], from the all boundary values. Several integration points on a segment are set to estimate the integral of the flux density on each segment, as shown in Fig. 5.7. However, when the point to estimate the field is located near the source points, which correspond to the SPs, the BEM has a large computational error.

The following flux conservation law for every elementary loop cannot be satisfied due to the error:

$$\oint_c \nabla A_z \cdot \hat{\boldsymbol{n}}\, dl \;= -2\pi \sum_k \int_S m_k\, \delta(\boldsymbol{r} - \boldsymbol{r}_k)\, dS, \tag{5.19}$$

which is derived from Eq. (5.17) using the Gauss' divergence theorem. To reduce this error, a SVD is applied to find a minimum-norm solution. The error vector on the j-th segment in the k-th elementary loop, $\boldsymbol{e}_{k,j}$, is defined as a difference between the gradient computed by BEM, $(\nabla A_z)'_{k,j}$, and the gradient satisfying the flux conservation law, $(\nabla A_z)_{k,j}$:

$$\boldsymbol{e}_{k,j} = (\nabla A_z)'_{k,j} - (\nabla A_z)_{k,j}. \tag{5.20}$$

The flux conservation law shown in Eq. (5.19) for the elementary loop k is rewritten as

$$\sum_{j=1}^{4} \left((\nabla A_z)'_{k,j} - \boldsymbol{e}_{k,j}\right) \cdot \hat{\boldsymbol{n}}_{k,j} = -2\pi m_k. \tag{5.21}$$

The number of equations is identical to that of loops, N_l, and the number of unknown variables of $\boldsymbol{e}_{k,j} \cdot \hat{\boldsymbol{n}}_{k,j}$ is $4N_l$ because each loop has four segments. However, the $\boldsymbol{e} \cdot \hat{\boldsymbol{n}}$ is known as zero on the boundary segments of which the number is N_b. Furthermore, since every internal segment belongs to two loops, the error vectors in these two loops can be defined by a vector on a segment,

$$\boldsymbol{e}_{k,j} = \boldsymbol{e}_{k',j'} = \boldsymbol{e}_i, \tag{5.22}$$

where the two subscript pairs of k, j and k', j' indicate the same segment i. Thus, the number of unknowns is reduced to that of internal segments; i.e. $N_s = (4N_l - N_b)/2$. In contrast

to the error vector, two direction vectors, $\hat{\boldsymbol{n}}_{k,j}$ and $\hat{\boldsymbol{n}}_{k',j'}$, on the segment i have the different direction. A new unit vector, $\hat{\boldsymbol{d}}_i$, is introduced that is identical to either $\hat{\boldsymbol{n}}_{k,j}$ or $\hat{\boldsymbol{n}}_{k',j'}$, the normal unit vector can be defined as

$$\hat{\boldsymbol{n}}_{k,j} = d_{k,i}\hat{\boldsymbol{d}}_i, \tag{5.23}$$

where $d_{k,i}$ can take either ± 1, depending on the loop as well as the segment. Thus, Eq. (5.21) can be transformed to the following matrix form:

$$\mathbf{D}\,\mathbf{e} = \mathbf{r}, \tag{5.24}$$

$$(\mathbf{D})_{k,i} = d_{k,i}, \quad (\mathbf{e})_i = \hat{\boldsymbol{d}}_i \cdot \boldsymbol{e}_i,$$

$$(\mathbf{r})_k = 2\pi m_k - \sum_i d_{k,i}\hat{\boldsymbol{d}}_i \cdot (\nabla A_z)'_i. \tag{5.25}$$

In Eq. (5.24), the $\mathbf{D}$ is an N_l-by-N_s matrix. In most clustered domains, the relation between the dimensions of the matrix is given as $N_l < N_s$ except a few cases in which the domain consists of one-dimensionally aligned loops or a 2-by-2 aligned loop. Therefore, the set of equations is a rank-deficient, under-determined system of linear equations that cannot be solved in an ordinal way. However, since the solution list, $\mathbf{e}$, is the list of errors that should be small, the following condition can be imposed:

$$\text{minimize} \sum_i \left| (\mathbf{e})_i \right|^2. \tag{5.26}$$

To solve Eq. (5.24) with this condition, SVD routine provided by LAPACK [54] is used in the LC.bem+svd method. The flux is updated by the error:

$$(\nabla A_z)_{k,j} = (\nabla A_z)'_{k,j} - \boldsymbol{e}_{k,j}. \tag{5.27}$$

An example of the ∇A_z was shown in Fig. 5.6(b).

After the ∇A_z is obtained, the compensator for the segment is evaluated by Eq. (5.18). In the case where a segment belongs in several cluster domains, the compensator is accumulated as

$$\boldsymbol{c} = \sum_m \boldsymbol{c}_m, \tag{5.28}$$

where $\boldsymbol{c}_m$ is the compensator to the segment of the m-th domain.

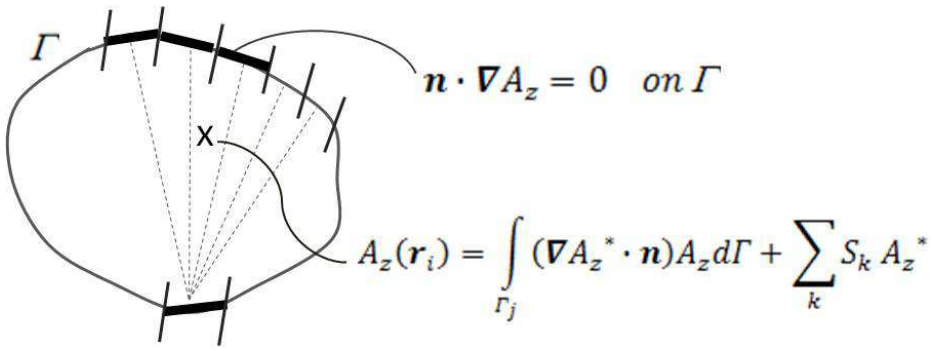

Figure 5.7: *Schematic of BEM to solve flux density A_z: shows the steps of BEM to compute the flux, the condition in boundary Γ is $\hat{\boldsymbol{n}} \cdot \nabla A_z = 0$, and for internal point inside the specific domain is, $A_z(\boldsymbol{r}_i) = \int_{\Gamma_i} (\nabla A_z^* \cdot \hat{\boldsymbol{n}}) A_z \, d\Gamma + \sum_k S_k A_z^*$.*

Figures 5.8, 5.9 and 5.10 present examples of unwrapped phase results obtained for two simulated data and one experimental phase data, respectively; to show comparison of the unwrapped results when they obtained by the old LC method by using BEM only, and when LC method uses BEM and SVD. In addition, Fig. 5.10 show accuracy comparison for the unwrapped results of experimental data obtained by the RC+DC method and the old LC method. Figures 5.8 and 5.9 illustrate the comparison of the simulated phase examples, The simulated phase data are two phase map with the same gradient $(0.1, -0.1)$ [cycle/pixel], and the image area 100×100 [pixel^2]. However, they contain a set of noise with normal distributions but different standard deviations. The first simulated noisy phase map with standard deviation 0.15 cycle is shown as original and wrapped phase in Fig. 5.8(a) and (b), respectively. This phase data has 453 positive SPs and 456 negative SPs, as shown in Fig. 5.8(c); the sum of them exceeds 9% of the number of all pixels. The unwrapped result with contour lines obtained by the old LC method by using BEM only is shown in Fig. 5.8(d). Meanwhile, the result obtained when using both BEM and SVD is shown in Fig. 5.8(e). From the figure it can be seen that in the case when the old LC method is used BEM only to obtained its unwrapped result, has fluctuation. This is indicated that the gradients for this unwrapped result are not accurate as it can be seen from the errors image generated due to using of BEM only for unwrapped result shown in Fig. 5.9(f) comparing the errors image produced due to the difference between the original phase data and the unwrapped result obtained by using BEM and SVD, as shown in Fig. 5.9(g). Moreover, these observations can be confirmed from Table 5.1. This table shows a quantitative comparison of gradients of the original and unwrapped phase maps. In the table,

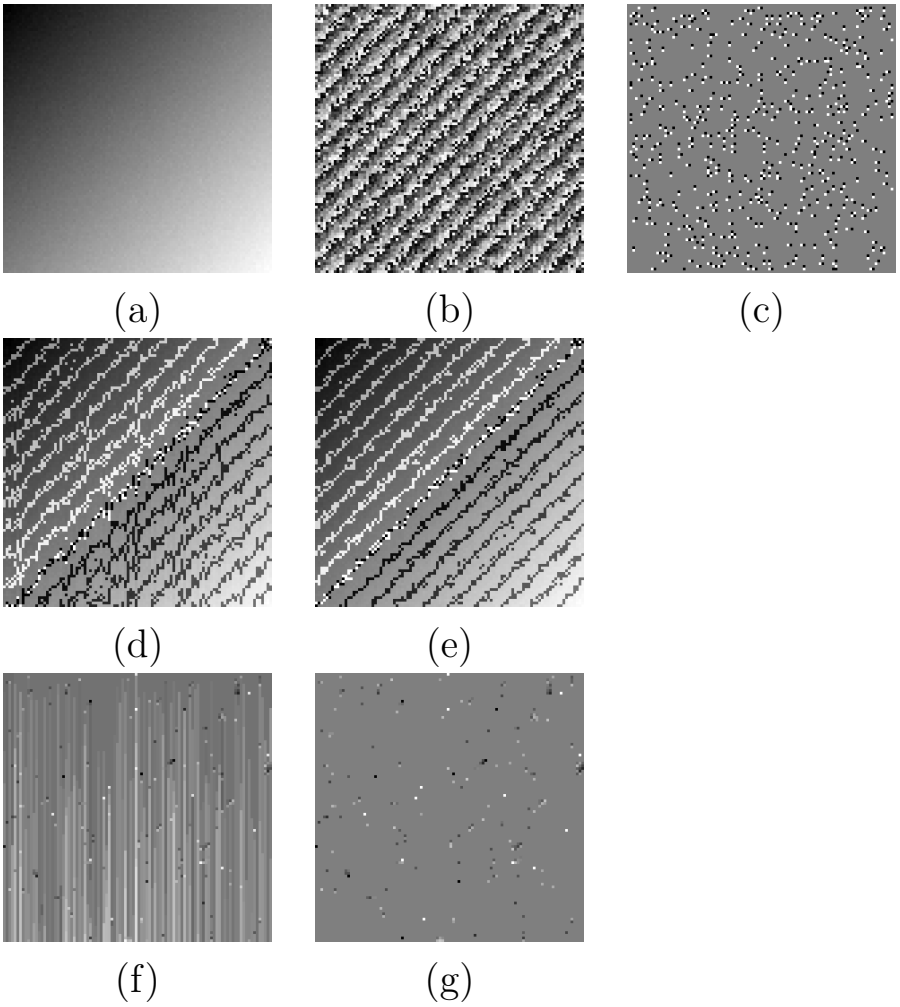

Figure 5.8: *An example of unwrapped phase results for simulated phase data has noise with standard deviation* 0.15 *cycle, to show the errors produce when use BEM only for the old LC method: (a) original phase data, (b) wrapped data, (c) SPs distribution map (positive and negative SPs are represented by white and black dots, respectively), (d) unwrapped result of the old LC method by using BEM only, (e) unwrapped result obtained by the old LC method using both BEM and SVD, (f) errors generated due to using of BEM only for unwrapped result the range of values is* $[-0.3\pi : 0.4\pi]$*, and (g) errors generated due to using both BEM and SVD to produce unwrapped result the range of values is* $[-0.3\pi : 0.3\pi]$*. In (a), (b), and (d), (e), the phase increases with the increases of brightness. In (d), (e), contour lines of the phase with the interval of one cycle are also shown.*

Algorithm	Gradient ($\nabla\tilde{\phi}$) [cycle/pixel]	R^2	$Time$ [sec]
Original	(0.1001 , –0.1001)	—	—
LC.bem	(0.1000 , –0.0974)	0.0318	0.18
LC.bem+svd	(0.1000 , –0.1000)	0.0047	0.19

Table 5.1: *A comparison of the accuracy for the simulated noisy data with* 0.15 *cycle standard deviation, shown in Fig. 5.8; "LC.bem" is the old LC method by using BEM only, and "LC.bem+svd" is the old LC method by using both BEM and SVD.*

the gradients are obtained by fitting them to a planar function, $\tilde{\phi}$, while, R^2 is the squared error between the original phase data and the unwrapped results. It can be seen from this table that the gradient for $x-$direction of the result obtained by BEM only has error value comparing with the gradient of the result obtained by both BEM and SVD, and this can be approved from the R^2 values, since its value is a little higher for the case of using BEM only.

The second simulated phase data has 0.2 cycle standard deviation of noise, is shown as original and wrapped phase in Fig. 5.9(a) and (b), respectively. This phase data has 1033 positive SPs and 1031 negative SPs, as shown in Fig. 5.9(c); the sum of them exceeds 20% of the number of all pixels. The unwrapped and rewrapped results obtained by the old LC method by using BEM only are shown in Fig. 5.9(d) and (f), respectively. Meanwhile, the results obtained when using both BEM and SVD are shown in Fig. 5.9(e) and (g), respectively. It can be observed that the unwrapped result of BEM only is not accurate and there are many phase jumps in it, as shown in Fig. 5.9(d). While, the unwrapped result obtained by both BEM and SVD shown in Fig. 5.9(e) is smooth. In addition, the stripes in the rewrapped result provided by BEM only are not distinguished, indicates that the gradients for this unwrapped result are not accurate as also seen from the errors image generated due to using of BEM only for unwrapped result shown in Fig. 5.9(h) comparing the errors image produced due to the difference between the original phase data and the unwrapped result obtained by using BEM and SVD, as shown in Fig. 5.9(i). Furthermore, these observations can be confirmed from Table 5.2. This table shows a quantitative comparison of gradients of the original and unwrapped phase maps. It can be seen from this table that the gradient for $x-$direction of the result obtained by BEM only has large error value comparing with the gradient of the result

Algorithm	Gradient ($\nabla\tilde{\phi}$) [cycle/pixel]	R^2	$Time$ [sec]
Original	(0.1001 , –0.1001)	—	—
LC.bem	(0.0789 , –0.0913)	0.5797	7.22
LC.bem+svd	(0.0864 , –0.0946)	0.3125	11.00

Table 5.2: *A comparison of the accuracy for the simulated noisy data with* 0.2 *cycle standard deviation, shown in Fig. 5.9; "LC.bem" is the old LC method by using BEM only, and "LC.bem+svd" is the old LC method by using both BEM and SVD.*

obtained by both BEM and SVD, and this can be approved from the R^2 values, since its value is more higher for the case of using BEM only. However, the computational time required to obtained the unwrapped result obtained by both BEM and SVD is higher than that time for using BEM only. This is considered a big disadvantage of the old LC method (LC.bem+svd) which uses both computations of BEM and SVD to produce its unwrapped results.

Figure 5.10 shows the unwrapped results of wrapped phase map that resulted from the analysis of real fringe pattern taken from the experiment carried out by using Mach-Zehnder interferometer. The purpose of this experiment is to measure the phase shift in candle flames [46]. The phase data has image size 256×170 pixel^2 and 2532 SPs. The wrapped phase data and its corresponding SPs distribution map are shown in Fig. 5.10(a) and (b), respectively. Moreover, the unwrapped results, which have contour lines, obtained by RC+DC method and old LC method when it uses BEM only and when it uses both BEM and SVD are given in Fig. 5.10(c), (d) and (e), respectively. From the figure, it can be noticed that the contour lines of the unwrapped result obtained by BEM only has many disturbance and fluctuation indicates that this result has errors and not accurate. As well, the unwrapped result of RC+DC method also has fluctuation in its contour lines, which means that the RC+DC method produces not accurate unwrapped result. Meanwhile, the unwrapped result obtained by the old LC method when using both BEM and SVD is smooth, and the shape of its contour lines are similar to the stipes of the wrapped data. However, the time cost for the LC.bem+svd method when it uses both BEM and SVD is the highest computational time cost, which is 21.87 sec, among the studied algorithm. While, the computational time cost of old LC method when using BEM only is 11.86 sec; also, the computational time cost required for RC+DC method is 8.8 sec.

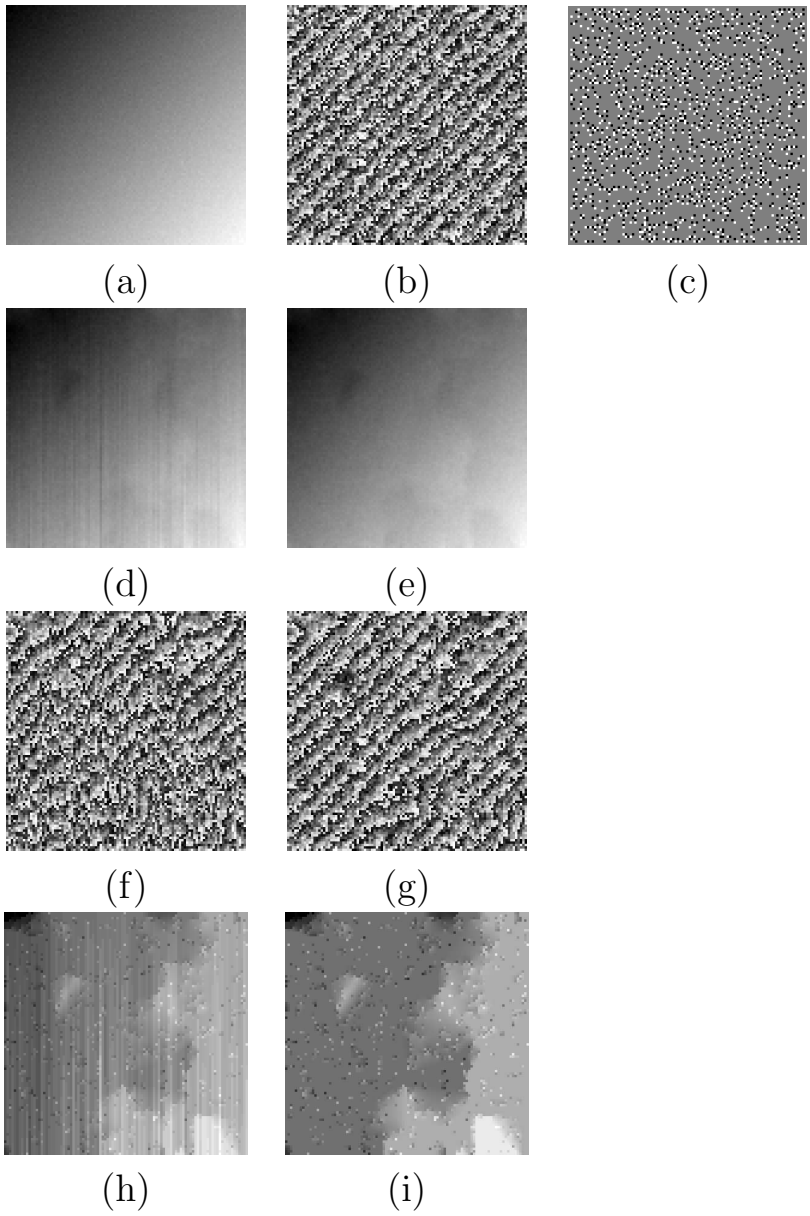

Figure 5.9: *An example of unwrapped phase results for simulated phase data has noise with* 0.2 *cycle standard deviation to show the errors produce when use BEM only for the old LC method: (a) original phase data, (b) wrapped data, (c) SPs distribution map (positive and negative SPs are represented by white and black dots, respectively), (d) unwrapped result of the old LC method by using BEM only, (e) unwrapped result obtained by the old LC method using both BEM and SVD, (f) rewrapped result of the old LC method by using BEM only, (g) rewrapped result obtained by the old LC method using both BEM and SVD, (h) errors generated due to using of BEM only for unwrapped result the range of values is* $[-0.06\pi : 1.8\pi]$*, and (i) errors generated due to using both BEM and SVD to produce unwrapped result the range of values is* $[-0.05\pi : 1.3\pi]$.

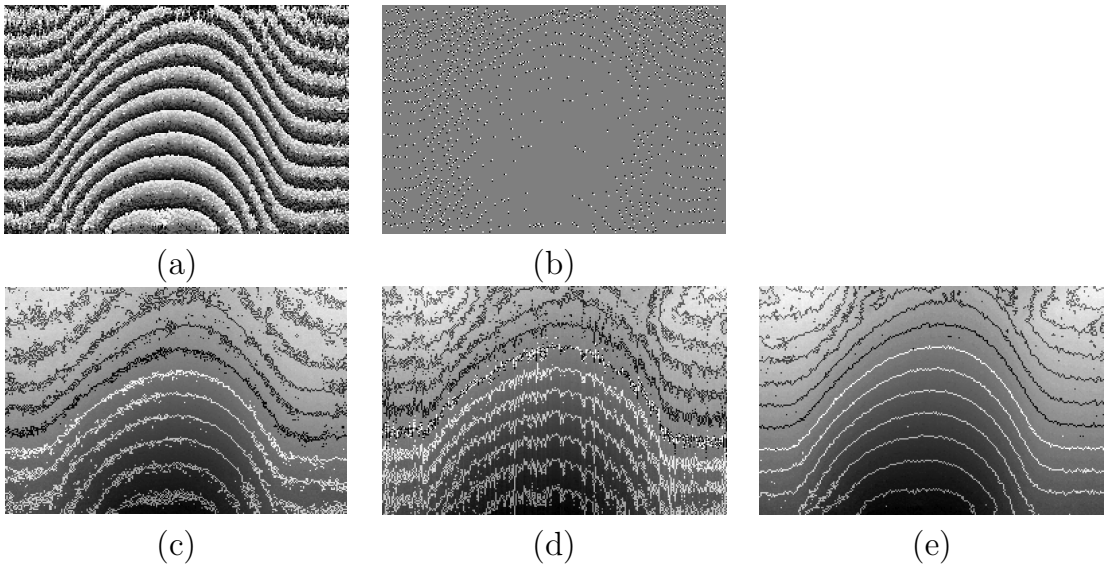

Figure 5.10: *Accuracy comparison for unwrapped phase results of experimental data for candle flame: (a) wrapped data, (b) SPs distribution map (positive and negative SPs are represented by white and black dots, respectively), (c) unwrapped result of the RC+DC method, (d) unwrapped result of the old LC method by using BEM only, and (e) unwrapped result obtained by the old LC method using both BEM and SVD. In (c), (d) and (e), contour lines of the phase with the interval of one cycle are also shown.*

The too high computational time cost of the old LC method when it uses both BEM and SVD is considered a big problem for this method, specially when the wrapped phase data has large image size or includes high noise ratio, and this is what we will solve in the next section.

5.3.4 The description of the proposed algorithm (LC.rot+div)

The purpose of the current proposed phase unwrapping algorithm is to improve the performance of the localized compensator phase unwrapping method (LC.bem+svd). This is happened by reducing the computational time cost required to solve Poisson equation with Neumann condition to compute the flux, ∇A_z, to evaluate the compensator values with line integral of ∇A_z shown in Eq.(5.18). To explain the idea of the proposed algorithm, consider A_z as a scalar potential, ϕ; and consider the source charges in the right-hand in Eq.(5.17) which are electrostatic charges as $S = \rho$, where ρ is normalized by ϵ_0. Therefore, it is just considered as a potential problem in electromagnetics, and Poisson's equation shown in Eq. (5.17) can

be modified as follows:

$$\nabla^2\phi = S \tag{5.29}$$

From identity of vector calculus we can get:

$$\nabla \cdot \nabla\phi = S \tag{5.30}$$

In the case of static fields, it is in general not necessary to describe the problem by vectors; and the electric field at point is equal to the negative gradient of the scalar electric potential,

$$\boldsymbol{E} = -\nabla\phi \tag{5.31}$$

Hence, we can obtain the divergence of the electric field shown in Eq. (5.30) as total charge density divided by the permittivity of free space,

$$\nabla \cdot \boldsymbol{E} = S \tag{5.32}$$

Equation (5.32) illustrates that the integral of the electric flux, which is the compensator value along the line segment, out of a closed surface is equal to the charge enclosed. Therefore, by getting the solution of Eq. (5.32), the compensator values are directly evaluated; and this is the merit of our proposed algorithm. In contrast, the BEM computes the solution of Poisson equation as point values of flux, hence it requires integration of these flux points to obtain the compensator values. As a result, this is evaluation by using BEM to obtain the compensator values produces errors, especially when the charge sources, which are SPs, are located near to the segments that required to compute their compensator values. Therefore, SVD technique is used in the original LC method (LC.bem+svd) to fix these error, means that high time cost is required. In contrast, the proposed algorithm does not need this step, since it computes the line integral directly, means that it reduces the required computational time cost.

Unfortunately, every elementary loop (2×2 pixel path) in each cluster has only one divergence equation, Eq. (5.32), with four segments (have unknown flux values). Hence, to solve these unknown variables, more equations are needed. These equations can be provided from Eq. (5.31) by applying rotational operator for this equation, we can get the following relation:

$$\nabla \times \boldsymbol{E} = -\nabla \times \nabla\phi \tag{5.33}$$

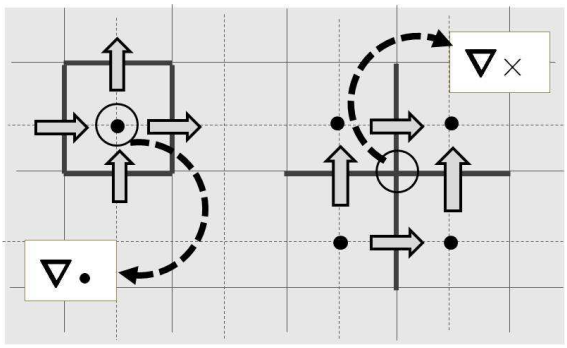

Figure 5.11: *A schematic for the proposed algorithm to illustrate the way for solving Poisson's equation to compute the flux values. This way uses rotational, ($\nabla\times$), and divergence, ($\nabla\cdot$) operators to produce the flux density values directly without any integration to evaluate the compensators.*

Because that the rotational of a scalar function equals zero, hence:

$$\nabla \times \boldsymbol{E} = 0 \tag{5.34}$$

Equation (5.34) represents that the induced electromotive force in any closed loop equals zero in the case of static field. The position of divergence and rotational equation points for the flux density are depended on SP positions. Figure 5.11 shows a schematic for the proposed algorithm to illustrate the way for solving Poisson's equation to compute the flux values. The divergence equation is shown the divergence between the flux lines, its position is in the center of the loop as shown in Fig 5.11. Meanwhile, the central point position for the grid of the rotational operator is shifted with 0.5 pixel size width from the divergence point position, as shown in Fig 5.11. Furthermore, the orientations (signs), $+1$ or -1, for rotational and divergence matrices are dependent on the direction of flux lines and also are respect to their directions for the axis x and y. For cluster size of $M \times N$, the number of unknown variables is $2MN-3(N+M)+4$. Moreover, the number of divergence equations is $(M-1)(N-1)$, and the number of rotational equations is $(M-2)(N-2)$. Therefore, the number of total equations is $2MN-3(N+M)+5$, means it is greater than the number of unknown variables with one redundancy equation. To solve the rotational and divergence equations, simultaneous equation can be generated by joint the rotational and divergence matrices as,

$$\mathbf{Ax} = \mathbf{b} \tag{5.35}$$

where **A** matrix is resulted as rearranging of the rotational and divergence matrices, **x** denotes the list of line integral of electric flux, which are the required the compensator values, and **b**

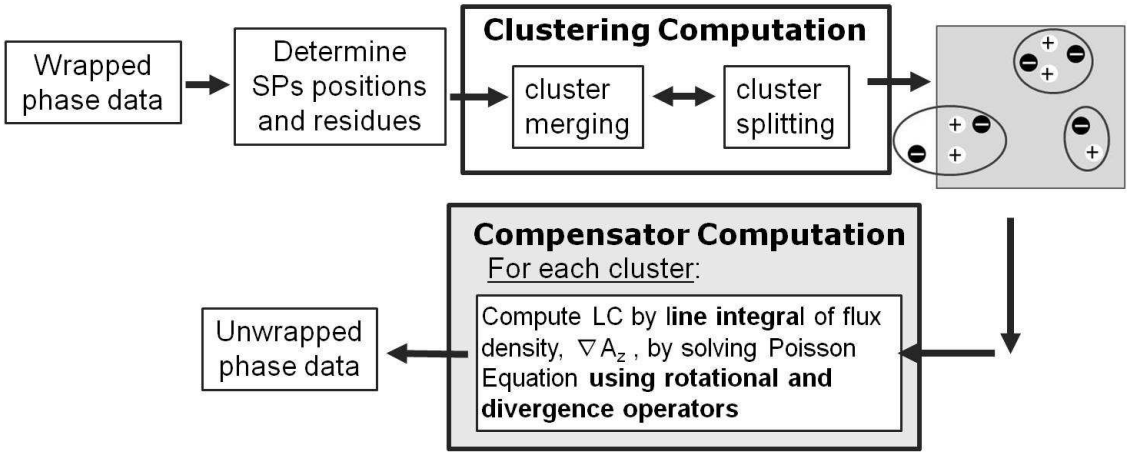

Figure 5.12: *A flowchart of the proposed algorithm (LC.rot+div).*

represents the list of source term. These equations consist a linear equations set, in which the matrix of equations has square shape. Since, the **A** matrix is a sparse matrix of which most of its components are zero and the non-zero elements are $+1$ or -1, it can be saved the memory by compressing the **A** matrix. In the proposed algorithm, we convert this square sparse matrix to band matrix, then a routine solver provided by LAPACK [54] is used for band matrix. This is reduce the restriction of memory shortage in the original LC method (LC.bem+svd). We refer to the proposed algorithm as localized compensator phase unwrapping method based on rotational and divergence operators (LC.rot+div). Figure 5.12 illustrates a flowchart of the proposed algorithm (LC.rot+div), to show the main steps in the compensator computation. This description of using rotational and divergence operators to solve Poisson equation to evaluate the compensator values through computing the flux density, A_z, makes the proposed algorithm (LC.rot+div) simple and easy to implement. It provides a fast and efficient way to unwrap the phase map, by reducing the computational time required to compute the compensator values. In the following section, the performance and applicability of the proposed algorithm is examined.

5.4 Results and discussion

In this section, two examples of noisy wrapped phase maps are presented. One is a simulated phase map where the true phase is known to evaluate the accuracy of the proposed algorithm

Algorithm	Gradient ($\nabla\tilde{\phi}$) [cycle/pixel]	$\Delta\left(\nabla\tilde{\phi}\right)$ [%]	σ [cycle/pixel]
Original	(0.1001 , –0.1001)	(— , —)	0.199
LC.bem+svd	(0.0864 , –0.0946)	(–13.7 , –5.5)	0.361
LC.rot+div	(0.0865 , –0.0944)	(–13.6 , –5.7)	0.359

Table 5.3: *A comparison of the accuracy for the simulation data, shown in Fig. 5.13; "LC.bem+svd" is the old LC method, and "LC.rot+div" is the proposed method.*

quantitatively. The other is the experimental data obtained with interferometer to demonstrate the performance of the proposed method for noisy phase data.

5.4.1 Simulated wrapped phase for known phase map

In order to demonstrate the applicability of the proposed algorithm, a simulated noisy phase map with constant gradient has 0.2 cycle standard deviation is generated, shown as original and wrapped data in Fig. 5.13(a). The unwrapped phase results obtained by the old LC method (LC.bem+svd) [48] and the proposed modified LC algorithm (LC.rot+div) are shown in Fig. 5.13(b) and (c), respectively; with their rewrapped results. We can noticed that the unwrapped phase results of the compared algorithms are smooth and look likes the original phase data, as shown in the left-hand side of Fig. 5.13. This observation can be confirmed from the phase error shown Fig. 5.13(d), which is the difference between the two unwrapped results obtained by the LC.bem+svd and the proposed LC.rot+div methods. Moreover, the accuracy of the proposed algorithm can be emphasized as shown in Table 5.3. This table shows a quantitative comparison of gradients for the original and unwrapped phase maps. In the table, the gradients are obtained by fitting them to a planar function, $\tilde{\phi}$, and the σ denotes the mean residual that is defined as a square root of a mean square residual from the fitted function, $\tilde{\phi}$. The σ of the original phase data is not equal to zero, because the original data contains noise with the given standard deviation. The errors of gradient, $\Delta\left(\nabla\tilde{\phi}\right)$ is estimated as the normalized difference between the unwrapped result and the original one, where the normalizing factor is the reciprocal of original one. From the table, it can be observed that the accuracy of the LC.bem+svd method and the proposed LC.rot+div algorithm is similar.

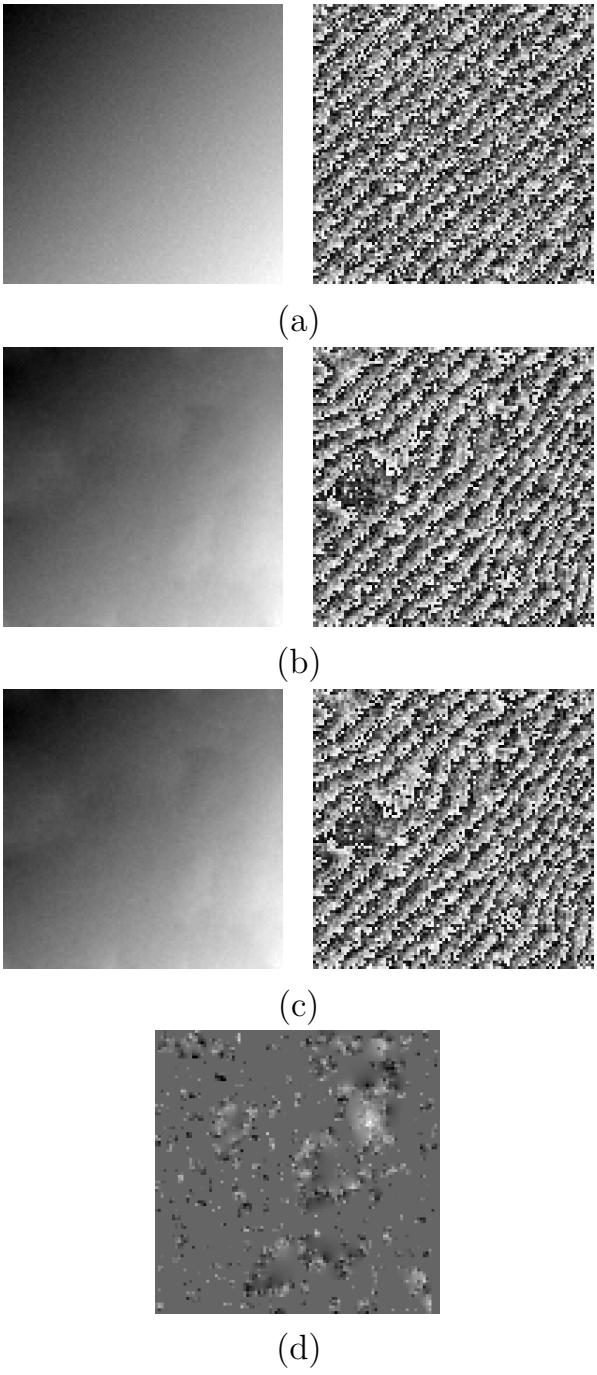

Figure 5.13: *A comparison of the unwrapped phase results for simulated phase data has noise with $\sigma = 0.2$ [cycle]: (a) the original and wrapped phase data, (b) the unwrapped and rewrapped results obtained by the old LC method (LC.bem+svd), (c) the unwrapped and rewrapped results obtained by the proposed modified LC method (LC.rot+div), (d) the phase difference between the unwrapped results the range of values is $[-0.1\pi : 0.2\pi]$. The left side in (a) to (c), the phase increases with the increases of brightness.*

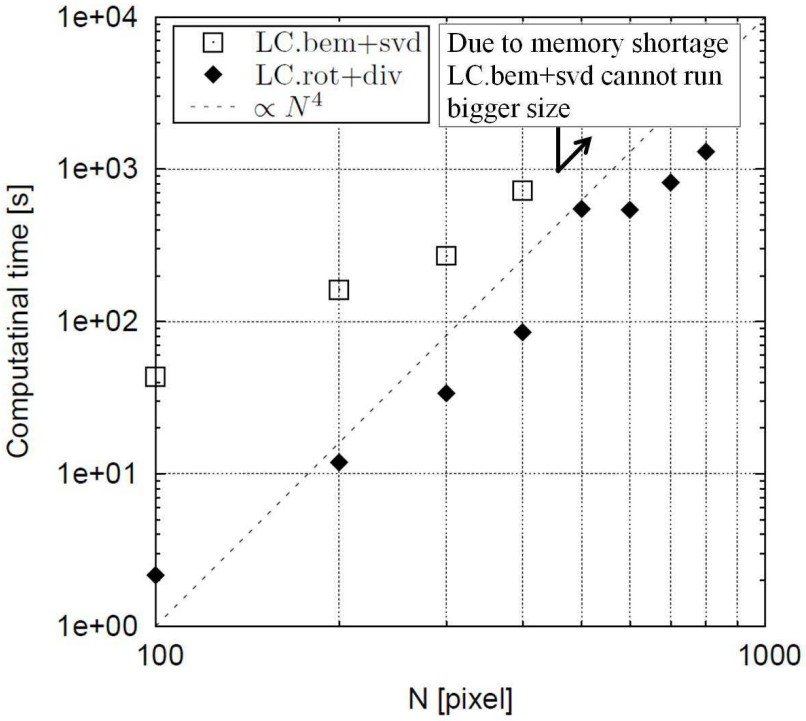

Figure 5.14: *Required computational time of each algorithm for various image sizes: The horizontal axis N denotes one-dimensional area size in pixels. "LC.bem+svd" shows the required time cost for the old LC method, and "LC.rot+div" shows the required execution time for the proposed method.*

Figure 5.14 shows a comparison of required computational time for the old LC.bem+svd method and the proposed modified LC.rot+div method for various image sizes, with the same data component regards the gradients and the standard deviation of the noise contained in the data. In the figure, the horizontal axis N denotes one-dimensional area size in pixels. The computational time for each phase unwrapping algorithm is measured using a PC with Intel Core 2 DUO CPU installed, with 2.13 GHz clock in a single CPU operation mode. The computing language used to implement the compared phase unwrapping algorithms is C language. From the figure, we can observed two big problems related to the computational time cost of the LC.bem+svd method. The first problem is that the old LC.bem+svd algorithm can not provide unwrapped results for noisy phase data with image sizes greater than 400×400 pixel^2, due to memory shortage. This is due to that the LC.bem+svd method required very large memory size to compute the compensator values by SVD method to fix the errors of the results, although there is no memory restriction by BEM method itself. In addition, the

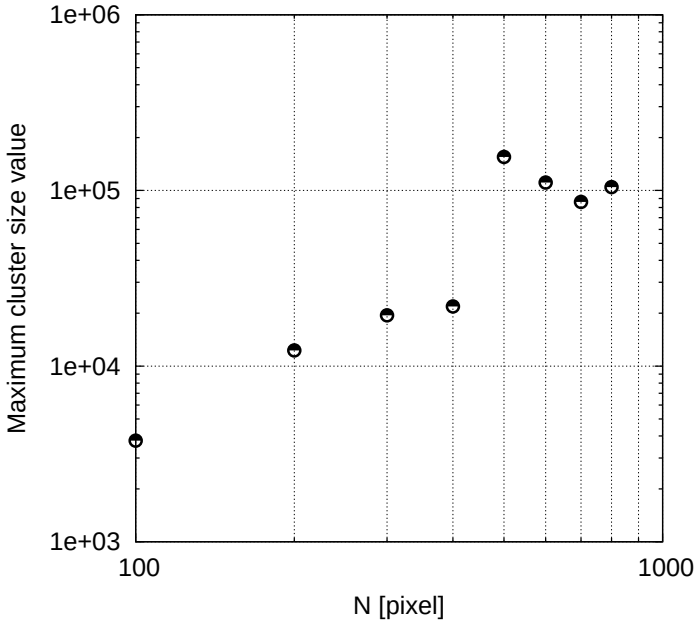

Figure 5.15: *The maximum cluster size for various image sizes: The horizontal axis N denotes one-dimensional area size in pixels.*

LC.bem+svd method has higher computational time cost to obtain its unwrapped results for smaller image sizes comparing with the proposed LC.rot+div method for the same data, as shown in the figure. However, we can see that the computational time cost for the proposed method to obtain its unwrapped result for the phase data with size 500×500 pixel^2 is the highest cost among the execution time of other phase data size. The reason for that is the cluster distribution and size for this data, as shown in Fig. 5.15. It can be noticed that this size has the maximum cluster size comparing with the other data sizes.

From above-mentioned discussion, it can be concluded that the execution time to compute the compensators in the proposed algorithm LC.rot+div is reduced compared to that one of the original LC.bem+svd method and solve the problem of memory shortage for larger phase data size.

5.4.2 Experimental data obtained by interferometer

The proposed LC.rot+div algorithm has also been tested experimentally on two-dimensional wrapped phase map that resulted from the analysis of real fringe pattern taken from the ex-

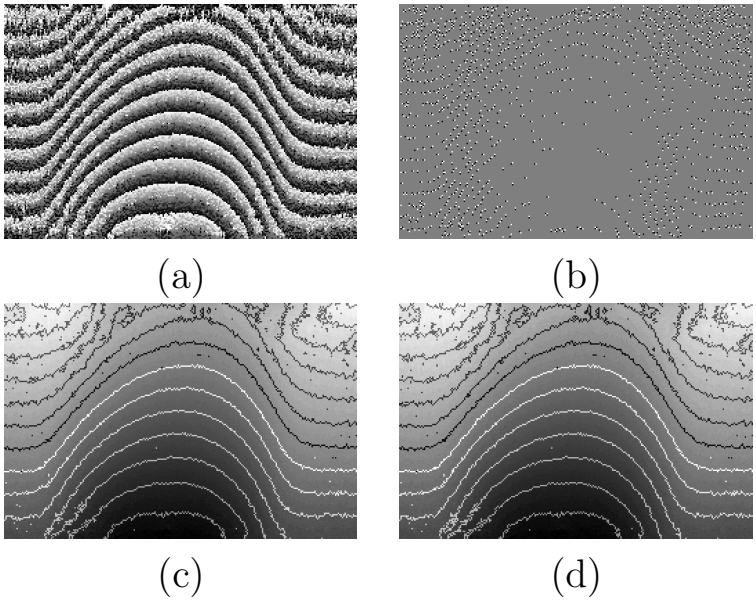

Figure 5.16: *Unwrapped phase results of experimental data for candle flame: (a) wrapped data, (b) SPs distribution map (positive and negative SPs are represented by white and black dots, respectively), (c) unwrapped result of the old LC method (LC.bem+svd), and (d) unwrapped result obtained by the proposed method (LC.rot+div). In (c) and (d), contour lines of the phase with the interval of one cycle are also shown.*

periment carried out by using Mach-Zehnder interferometer. This data is the same data that used in section 5.3.3. The purpose of this experiment is to measure the phase shift in candle flames [46]. The wrapped phase data and its corresponding SPs distribution map are shown in Fig. 5.16(a) and Fig. 5.16(b), respectively. Moreover, the unwrapped results, which have contour lines, obtained by LC.bem+svd method and the proposed algorithm (LC.rot+div) are given in Fig. 5.16(c) and Fig. 5.16(d), respectively. The accuracy of phase unwrapping methods can be evaluated by comparing the shape of phase discontinuity in the wrapped data and the shape of contour lines in the unwrapped phases. It can be found that the accuracy of the LC.bem+svd method and the proposed method have similar level of accuracy. However, the execution time required for the LC.bem+svd method to obtain the unwrapped result, which is 24.59 sec, is much higher compared to that of the proposed LC.rot+div method to obtain its unwrapped result, which is 2.91 sec. Therefore, it can be said that the proposed method (LC.rot+div) provides its unwrapped result with same accuracy and smaller computational time requirement compared to the LC.bem+svd method does.

5.5 Conclusions

To solve phase unwrapping problems, many methods have been developed, nevertheless, providing satisfactory results with better quality leads to a time consuming process. Phase unwrapping for noisy data by using LC.bem+svd method had higher accuracy than the other existing methods. However, it has drawbacks of memory shortage and computational time requirement, since, it is needed high time cost to solve Poisson's equation to produce the compensator values. To overcome these drawbacks, we use a new way to produce the compensator values. The proposed algorithm (LC.rot+div) solves the Poisson's equation by using rotational and divergence operators to get the compensators without any effect of the singularity source positions. The proposed algorithm was tested on both computer-simulated and experimental noisy phase data. The results show that the proposed LC.rot+div algorithm provides the unwrapped results with same accuracy and smaller computational time requirement compared to the original LC.bem+svd method.

CHAPTER 6

CONCLUSIONS

Chapter 6
Conclusions

There has been an increasing interest in the automation of fringe analysis over the last decade. The main stages of fringe analysis technique are phase extraction and phase unwrapping. Phase unwrapping has been a research area for more than two decades. Despite no small amount of efforts, however, the problem remains unresolved. Phase unwrapping has faced great challenges especially when the wrapped data contains discontinuous and contiguous features at the same time. There is clearly a need for further investigation with particular emphasis to solve this problem. Our work here is meant to present a good insight to propose more accurate phase unwrapping algorithms.

This dissertation has made investigations in fringe pattern analysis process, specially for phase unwrapping stage. A general review to the main stages for fringe analysis process, which are phase extraction and phase unwrapping has been introduced. However, large concerning is given for the unwrapping stage, since it is the object of this study. Therefore, the phase unwrapping problem was presented, and the problems that face many phase unwrapping algorithms have been briefly described. The major problem for all phase unwrapping algorithms is the singularity problem and effect on the unwrapping process. SPs are local inconsistencies that prevent straight forward unwrapping. Furthermore, a brief review for some of existing phase unwrapping methods is also introduced.

This thesis has presented two novel phase unwrapping methods for the purpose of more accurate phase unwrapping for noisy wrapped phase maps for various optical applications. The first proposed method is named rotational and direct compensators phase unwrapping (RC+DC). The proposed RC+DC phase unwrapping algorithm uses local phase information to compensate parts of the field, which are SPs, that cause inconsistencies in the unwrapping results. It is based on three techniques rotational and direct compensators, unconstrained singular point, and virtual singular points. It uses DC for adjoining SP pairs, and uses RC for

other SP pairs. The adjoining pair is a dipole consists of two SPs with opposite signs separated by one pixel horizontally or vertically. The RC+DC method is fast, however, its accuracy is not guaranteed. Since, its accuracy is depending on reducing the times for using the RC technique which increases the phase distortion in the regular region, where SPs are not located the unwrapped results.

The second proposed phase unwrapping algorithm is based on singularity compensation for cluster regions of SPs; it aims to improve the performance of phase unwrapping using a localized compensator (LC.bem+svd) method regards the memory shortage and computational time requirements. The LC.bem+svd method regularizes the inconsistencies in local areas, which are clusters, around the SPs by integrating the solution of Poisson's equation for each cluster to evaluate the compensators. In terms of accuracy, the method using LC.bem+svd is superior to the other methods. Despite this, LC.bem+svd method has a major disadvantage of computational cost since this method requires long time cost to compute the compensators. Hence, to overcome these drawbacks, we use a new way to produce the compensator values. The proposed algorithm LC.rot+div solves the Poisson's equation by using rotational and divergence operators to get the compensators without any effect of the singularity source positions. The proposed LC.rot+div algorithm is tested on both computer-simulated and experimental noisy phase data. The results show that the proposed algorithm (LC.rot+div) is faster compared to the original algorithm with LC.bem+svd, meanwhile it keeps the same level of accuracy of the unwrapped results.

The proposed algorithms are tested on both simulated and experimental phase data. In regard to the unwrapped phase results of simulated data, the proposed algorithms give the best solution with high quality compared to the examined algorithms which are Goldstein's method and the least squares method with DCT. Moreover, the unwrapping methods have been applied on the measured phase maps obtained by interferometer for measuring a heated air around candle flame through measuring the phase shift caused by this flame. Also, the proposed methods give the best accuracy for unwrapping this type of measured data. Therefore, the proposed phase unwrapping algorithms are suitable for the complex wrapped phase data with large number of SPs. The reason for the better accuracy by the proposed algorithms results due to

Algorithm	Gradient ($\nabla\tilde{\phi}$)	$\Delta\left(\nabla\tilde{\phi}\right)$ [%]	σ	Time [sec]
σ_{noise}: 0.15 [cycle] ($N(\mathbf{s}^+) = 453$, $N(\mathbf{s}^-) = 456$)				
Original	(0.1000 , –0.1000)	(— , —)	0.149	—
Goldstein	(0.0892 , –0.0826)	(–10.8 , –17.4)	0.425	0.12
Flynn	(0.1000 , –0.1000)	(0.0 , 0.0)	0.159	47.81
LS-DCT	(0.0742 , –0.0731)	(–25.8 , –27.0)	0.179	0.16
SSPU	(0.0743 , –0.0730)	(–25.7 , –27.0)	0.179	5.10
RC	(0.0912 , –0.0896)	(–8.7 , –10.4)	0.168	3.98
RC+DC	(0.0955 , –0.0952)	(–4.4 , –4.9)	0.169	0.68
LC.bem+svd	(0.1000 , –0.1000)	(0.0 , 0.0)	0.145	2.74
LC.rot+div	(0.1000 , –0.1000)	(0.0 , 0.0)	0.146	0.44
σ_{noise}: 0.20 [cycle] ($N(\mathbf{s}^+) = 1033$, $N(\mathbf{s}^-) = 1031$)				
Original	(0.1000 , –0.1000)	(— , —)	0.199	—
Flynn	(0.0999 , –0.0999)	(–1.0 , –1.0)	0.260	136.30
LC.rot+div	(0.0865 , –0.0944)	(–13.6 , –5.7)	0.3590	0.60

Table 6.1: *Accuracy and computational time cost comparisons among the studied algorithms, for two examples of simulated noisy phase data.*

it confining the effect of singularities to the local region around each SP.

Table 6.1 provides a summary for quantitative comparison among six existing methods, which are Goldstein's path-following method [11], Flynn method [15] the LS-DCT method [25], the SSPU method [43], the RC method with using all approaches (RC, USP, VSP)[46] and the old LC method (LC.bem+svd). In addition the comparison includes the two proposed algorithms, which are RC+DC method, and LC.rot+div algorithm. The table shows the accuracy in two cases where the standard deviation of noise is 0.15 cycle and 0.20 cycle. The induced noise caused disturbances, which are SPs, in the phase map. The number of SPs is also shown in the table. The total numbers of SPs are 9% and 20% of the number of all pixels for each case. In the table, the gradients are obtained by fitting them to a planar function, $\tilde{\phi}$, and the errors of gradient, $\Delta\left(\nabla\tilde{\phi}\right)$ is estimated as the normalized difference between the unwrapped result and the original one, where the normalizing factor is the reciprocal of original one. While, σ denotes the mean residual that is defined as a square root of a mean square residual from the fitted function, $\tilde{\phi}$. The σ of the original phase data is not equal to zero, because the original data contains noise with the given standard deviation. The last column in the table shows the execution time required for each algorithm to obtained its unwrapped result. In the case

of noise with 0.15 cycle, it can be revealed from Table 6.1 that both Flynn method and the proposed algorithm (LC.rot+div) exhibited the best accuracy between the studied algorithms, because they give the smallest error in terms of $\Delta\left(\nabla\tilde{\phi}\right)$. However, the computational time cost of Flynn method is the highest cost as compared to all algorithms. Furthermore, In the case of 0.2 cycle standard deviation of noise, the comparison is given only for Flynn method and the proposed LC.rot+div algorithm to explore their performance in the case of high noise since they showed the best accuracy for 0.15 cycle noise. It is clear that Flynn method is better in terms of the accuracy although it has a higher computational time cost to produce its unwrapped results than the LC.rot+div does, as shown in the table. Therefore, it can be said that the proposed LC.rot+div algorithm gives accurate unwrapped phase results with low computational time cost.

As a summary, the presence of noise in the measured data, in which many SPs are found, often makes general phase unwrapping algorithms fail to produce accurate unwrapped results. Therefore, it is necessary to use a powerful phase unwrapping method to recover the desired smooth phase surface. For this reason, we propose our new phase unwrapping methods, those are applicable for actual measured phase data that is extracted from various applications. One example of these applications is dynamic three-dimensional shape measurement. When a measured object is varied with time, enough long exposure time cannot be allocated to obtain a deformed fringe pattern. The obtained fringe pattern with short exposure time has a low signal-to-noise ratio. Our proposed unwrapping methods (RC+DC, LC.rot+div) are successfully unwrapping such that kind of actual phase data and produce smooth and accurate unwrapped phase results with low computational time cost. Another example about the applicability of our proposed unwrapping methods for actual measured phase data is applications that are required large phase data size measuring, means these applications need to generate many phase images to collect the desired information related to these applications, such as computed tomography (CT) measurements.

BIBLIOGRAPHY

Bibliography

[1] Y. Ichioka, and M. Inuiya, "Direct phase detection system," Appl. Opt. **11**, 1507–1514 (1972).

[2] P. H. Chan, P. J. Bryanston-Cross, and S. C. Parker, "Spatial phase stepping method of fringe pattern analysis," Opt. and Laser Eng. **23** 343–354 (1995).

[3] A. Dursun, S. Ozder, and F. N. Ecevit, "Continuous wavelet transform analysis of projected fringe pattern," Measurement Science and Technology **15**, 1768–1772 (2004).

[4] M. Gdeisat, D. Burton, and M. Lalor "Spatial carrier fringe pattern demodulation by use of a two-dimensional continuous wavelet transform," Appl. Opt. **45**, 8722–8732 (2006).

[5] M. Takeda, H. Ina, and S. Kobayashi, "Fourier-transform method of fringe-pattern analysis for computer-based topography and interferometry," Opt. Soc. Am. **72**, 156–160 (1982).

[6] K. E. Perry, Jr. and J. McKelvie, "A comparison of phase shifting and Fourier methods in the analysis of discontinuous fringe patterns," Opt. and Lasers in Engineering **19**, 269–284 (1993).

[7] E. Cuche, P. Marquet, and C. Depeursinge, "Spatial filtering for zero-order and twin-image elimination in digital off-axis holography," Appl. Opt. **39**, 4070–4075 (2000).

[8] J. H. Bruning, D. R. Herriott, J. E. Gallagher, D. P. Rosenfeld, A. D. White, and D. J. Brangaccio, "Digital wavefront measuring interferometer for testing optical surfaces and lenses," Appl. Opt. **13**, 2693–2703 (1974).

[9] B. Breuckmann and W. Thieme, "Computer-aided analysis of holographic interferograms using the phase-shift method," Appl. Opt. **24**, 2145–2149 (1985).

[10] D. C. Ghiglia and M. D. Pritt, *Two-Dimensional Phase Unwrapping : theory, algorithms, and software* (Wiley, New York, 1998).

[11] R. M. Goldstein, H. A. Zebker, and C. L. Werner, "Satellite radar interferometry: Two-dimensional phase unwrapping," Radio Science **23**, 713–720 (1988).

[12] J. M. Huntley, "Noise-immune phase unwrapping algorithm," Appl. Opt. **28**, 3268–3270 (1989).

[13] J. R. Buckland, J. M. Huntley, and S. R. E. Turner, "Unwrapping noisy phase maps by use of a minimum-cost-matching algorithm," Appl. Opt. **34**, 5100–5108 (1995).

[14] R. Cusack, J. M. Huntley, and H. T. Goldrein, "Improved noise-immune phase-unwrapping algorithm," Appl. Opt. **34**, 781–789 (1995).

[15] T. J. Flynn, "Two-dimensional phase unwrapping with minimum weighted discontinuity," Opt. Soc. Am. A. **14**, 2692 – 2701 (1997).

[16] M. Costantine, "A novel phase unwrapping method based on network programming," IEEE Trans. Geoscience and Remote Sensing **36**, 813–821 (1998).

[17] B. Gutmann and H. Weber, "Phase unwrapping with the branch-cut method: Clustering of discontinuity sources and reverse simulated annealing," Appl. Opt. **38**, 5577–5593 (1999).

[18] S. A. Karout, M. A. Gdeisat, D. R. Burton, and M. J. Lalor, "Two-dimensional phase unwrapping using a hybrid genetic algorithm," Appl. Opt. **46**, 730–743 (2007).

[19] D. L. Fried, "Least-square fitting a wave-front distortion estimate to an array of phase-difference measurements," Opt. Soc. Am. **67**, 370–375 (1977).

[20] R. H. Hudgin, "Wave-front reconstruction for compensated imaging," Opt. Soc. Am. **67**, 375–378 (1977).

[21] B. R. Hunt, "Matrix formulation of the reconstruction of phase values from phase differences," Opt. Soc. Am. **69**, 393–399 (1979).

[22] H. Takajo and T. Takahashi, "Least-squares phase estimation from the phase difference," Opt. Soc. Am. A **5**, 416–425 (1988).

[23] H. Takajo and T. Takahashi, "Noniterative method for obtaining the exact solution for the normal equation in least-squares phase estimation from the phase difference," Opt. Soc. Am. A **5**, 1818–1827 (1988).

[24] D. C. Ghiglia and L. A. Romero, "Direct phase estimation from phase differences using fast elliptic partial differential equation solvers," Opt. Lett. **14**, 1107–1109 (1989).

[25] D. C. Ghiglia and L. A. Romero, "Robust two-dimensional weighted and unweighted phase unwrapping that uses fast transforms and iterative methods," Opt. Soc. Am. A **11**, 107–117 (1994).

[26] Q. Kemao, S. H. Soon, and A. Asundi, "A simple phase unwrapping approach based on filtering by windowed fourier transform." Opt. Laser Technol. **37**, 458–462 (2005).

[27] Q. Kemao, "Two-dimensional windowed fourier transform for fringe pattern analysis: Principles, applications and implementations," Opt. Laser Eng. **45**, 304–317 (2007).

[28] Q. Kemao, W. Gao, and H. Wang, "Windowed fourier-filtered and quality-guided phase-unwrapping algorithm," Appl. Opt. **47**, 5408–5428 (2008).

[29] J. C. Estrada, M. Servin, and J. A. Quiroga, "Noise robust linear dynamic system for phase unwrapping and smoothing," Opt. Express. **19**, 5126 – 5133 (2011).

[30] M. A. Navarro, J. C. Estrada, M. Servin, J. A. Quiroga, and J. Vargas, "Fast two-dimensional simultaneous phase unwrapping and low-pass filtering," Opt. Express. **20**, 2556 – 2561 (2012).

[31] J. C. Estrada, J. Vargas, J. M. Flores-Moreno, and J. A. Quiroga, "Windowed phase unwrapping using a first-order dynamic system following iso-phase contours," Appl. Opt. **51**, 7549 – 7553 (2012).

[32] F. Chen, M. Brown, and M. Song, M., "Overview of three-dimensional shape measurement using optical methods," Opt. Eng. **39**, 10 – 22 (2000).

[33] P. Rae, H. Goldrein, N. Bourne, W. Proud, L. Forde, and M. Liljekvist, "Measurement of dynamic large-strain deformation maps using an automated fine grid technique," Laser Eng. **31**, 113 – 122 (1999).

[34] T. Tsuruta, N. Shiotake, and Y. Itoh, "Hologram interferometry using two reference beams," JSAP **7**, 1092 – 1100 (1968).

[35] M. Hipp, J. Woisetschlager, P. Reiterer, and T. Neger, "Digital evaluation of interferograms," Measurement **36**, 53 – 66 (2004).

[36] G. K. Bhat, " Hybrid fringe analysis technique for the elimination of random noise in interferometric wrapped phase maps," Opt. Comm. : Appl. Mechanics **59**, 604–614 (1992).

[37] T. Yoshizawa, "The recent trend of moiré metrology," Robot. Mechatron. **3**, 80 – 85 (1991).

[38] Z. Wen-Sen, and S. Xian, "A direct mapping algorithm for phase measuring profilometry," Mod. Opt. **41** 89 – 94 (1994).

[39] M. Takeda, and K. Mutoh, "Fourier transform profilometry for automatic measurement," Appl. Opt. **24** 3977 – 3982 (1983).

[40] D. J. Bone, "Fourier fringe analysis: the two-dimensional phase unwrapping problem," Appl. Opt. **30**, 3627–3632 (1991).

[41] J. M. Huntley, "Three-dimensional noise-immune phase unwrapping algorithm," Appl. Opt. **40**, 3901–3908 (2001).

[42] D. J. Bone, H.-A. Bachor, and R. J. Sandeman, "Fringe-pattern analysis using a 2-D Fourier transform," Appl. Opt. **25**, 1653–1660 (1986).

[43] R. Yamaki and A. Hirose, "Singularity-spreading phase unwrapping," IEEE Trans. Geoscience and Remote Sensing **45**, 3240–3251 (2007).

[44] P. M. Morse and H. Feshbach, *Methods of Theoretical Physics* (McGraw-Hill, New York, 1953), pp. 52–54.

[45] S. Tomioka, S. Nisiyama, and T. Enoto, "Nonlinear least square regression by adaptive domain method with multiple genetic algorithms," IEEE Trans. Evolutionary Computation **11**, 1–16 (2007).

[46] S. Tomioka, S. Heshmat, N. Miyamoto, and S. Nishiyama, "Phase unwrapping for noisy phase maps using rotational compensator with virtual singular points," Appl. Opt. **49**, 4735–4745 (2010).

[47] W. H. Press, S. A. Teukolsky, W. T. Vetterling, and B. P. Flannery, *Numerical Recipes 3rd Edition: The Art of Scientific Computing* (Cambridge University Press, New York, 2007).

[48] S. Tomioka, and S. Nishiyama, "Phase unwrapping for noisy phase maps using localized compensator," Appl. Opt. **51**, 4984 – 4994 (2012).

[49] S. Heshmat, S. Tomioka, and S. Nishiyama, "Reliable phase unwrapping algorithm based on rotational and direct compensators," Appl. Opt. **50**, 6225 – 6233 (2011).

[50] C. A. Brebia and S. Walker, *Boundary element techniques in engineering* (Newnes-Butterworths, Boston, 1980).

[51] S. Tomioka and S. Nisiyama, "Analytical regularization of hypersingular integral for helmholtz equation in boundary element method," Enginnering Analysis with Boundary Elements **34**, 393–404 (2010).

[52] M. Arai, T. Adachi, and H. Matsumoto, "Highly accurate analysis by boundary element method based on uniform gradient condition," Trans. of the Japan Society of Mechanical Engineers. A **61**, 161–168 (1995). (in Japanese).

[53] M. Guiggiani, G. Krishinasamy, T. J. Rudolphi, and F. J. Rizz, "A general algorithm for the numerical solution of hypersingular boundary integral equations," Trans. of ASME : Journal of Applied Mechanics **59**, 604–614 (1992).

[54] E. Anderson, Z. Bai, C. Bischof, J. Demmel, J. Dongarra, J. Du Croz, A. Greenbaum, S. Hammarling, A. McKenney, S. Ostrouchov, and D. Sorensen, *LAPACK users' guide* (Society for Industrial and Applied Mathematics, Philadelphia, 1992).